R-01-49

# Development of hydrogeological modelling tools based on NAMMU

Niko Marsic
Kemakta Konsult AB

Lee Hartley, Peter Jackson, Mike Poole
AEA Technology, UK

Arnfinn Morvik
BSSI, Norway

September 2001

**Svensk Kärnbränslehantering AB**
Swedish Nuclear Fuel
and Waste Management Co
Box 5864
SE-102 40 Stockholm Sweden
Tel 08-459 84 00
+46 8 459 84 00
Fax 08-661 57 19
+46 8 661 57 19

ISSN 1402-3091
SKB Rapport R-01-49

# Development of hydrogeological modelling tools based on NAMMU

Niko Marsic
Kemakta Konsult AB

Lee Hartley, Peter Jackson, Mike Poole
AEA Technology, UK

Arnfinn Morvik
BSSI, Norway

September 2001

# Abstract

A number of relatively sophisticated hydrogeological models were developed within the SR 97 project to handle issues such as nesting of scales and the effects of salinity. However, these issues and others are considered of significant importance and generality to warrant further development of the hydrogeological methodology. Several such developments based on the NAMMU package are reported here:

- **Embedded grid:** nesting of the regional- and site-scale models within the same numerical model has given greater consistency in the structural model representation and in the flow between scales. Since there is a continuous representation of the regional- and site-scales the modelling of pathways from the repository no longer has to be contained wholly by the site-scale region. This allows greater choice in the size of the site-scale.
- **Implicit Fracture Zones (IFZ):** this method of incorporating the structural model is very efficient and allows changes to either the mesh or fracture zones to be implemented quickly. It also supports great flexibility in the properties of the structures and rock mass.
- **Stochastic fractures:** new functionality has been added to IFZ to allow arbitrary combinations of stochastic or deterministic fracture zones with the rock-mass. Whether a fracture zone is modelled deterministically or stochastically its statistical properties can be defined independently.
- **Stochastic modelling:** efficient methods for Monte-Carlo simulation of stochastic permeability fields have been implemented and tested on SKB's computers.
- **Visualisation:** the visualisation tool Avizier for NAMMU has been enhanced such that it is efficient for checking models and presentation.
- **PROPER interface:** NAMMU outputs pathlines in PROPER format so that it can be included in PA workflow.

The developed methods are illustrated by application to stochastic nested modelling of the Beberg site using data from SR 97. The model properties were in accordance with the regional- and site-scale models used in SR 97. Some very specific features of the SR 97 structural model, such as the increased permeability in the repository rock blocks, were omitted from the current study. A comparison between the NAMMU nested model and the HYDRASTAR site-scale model was made to assess the applicability of the new methodology to a performance assessment, and a check on consistency with SR 97. A Monte Carlo simulation of 100 stochastic realisations was performed with a set of 120 particles being released from the repository blocks for each realisation.

The new methodology is shown to be efficient and demonstrates a greater accuracy in nesting the regional- and site-scale models. Given the differences in representation of Beberg, the results of the new model are broadly consistent with SR 97. A more rigorous repeat of SR 97, such as including the repository rock blocks might be expected to give very similar results. Variable density flow is not considered here.

# Sammanfattning

Under arbetet med SR 97 utvecklades ett antal relativt sofistikerade hydrogeologiska modeller för att hantera problem som nästling av modeller i olika skalor och inverkan av saltvatten. Dessa och andra frågor anses dock vara av sådan generell betydelse att de motiverar vidare utveckling av den hydrogeologiska metodiken. Ett antal sådana utvecklingar baserade på NAMMU-paketet redovisas här:

- **Sammanlänkade nät:** länkning av regional- och lokalmodellerna (numeriskt länkade inneslutna nät med interna randvillkor) inom samma numeriska modell har lett till bättre överensstämmelse i representationen av strukturmodellen och i flödet mellan modellskalorna. Eftersom det finns en kontinuerlig representation av regional- och lokalmodellerna behöver inte modelleringen av partikelbanorna längre i sin helhet omfattas av lokalskalan. Det här ger större valfrihet vid valet av storlek på lokalmodellen.
- **Implicita sprickzoner (IFZ):** den här metoden för skapande av strukturmodellen är mycket effektiv och möjliggör snabb implementering av ändringar i endera FEM-nätet eller sprickzonerna. Det ger även stor flexibilitet vad gäller modifiering av egenskaper hos strukturerna och bergmassan.
- **Stokastiska sprickor:** ny funktionalitet har lagts till i IFZ så att valfria kombinationer av stokastiska eller deterministiska sprickor kan användas tillsammans med bergmassan. Egenskaper för sprickorna specificeras individuellt för varje spricka.
- **Stokastisk modellering:** effektiva metoder för Monte-Carlo-simulering av stokastiska permeabilitetsfält har implementerats och testats på SKBs datorer.
- **Visualisering:** visualiseringsverktyget Avizier för NAMMU har förbättrats med avseende på kontroll av modeller och presentationsmöjligheter.
- **PROPER-gränssnitt:** NAMMU exporterar data för partikelbanor i PROPER-formatet så att resultaten senare kan användas av andra programpaket.

De utvecklade metoderna demonstreras genom tillämpning på en stokastisk nästlad modell av Beberg med data från SR 97. Modellens egenskaper överensstämmer i stort med regional- och lokalmodellerna som användes inom SR 97. En del specifika detaljer i strukturmodellen i SR 97, så som högre permeabilitet inom förvarsblocken, utelämnades i den här studien. En jämförelse mellan NAMMU-modellen och HYDRASTAR-modellen gjordes för att bedöma användbarheten av den nyutvecklade metodiken inom arbetet med säkerhetsanalyser. Dessutom gjordes en jämförelse med resultaten från SR 97. En Monte-Carlo-simulering med 100 stokastiska realiseringar utfördes med 120 partiklar släppta från förvarsområdet för varje realisering.

Den nya metodiken visar sig vara effektiv och ger en bättre noggrannhet vid nästlig av regional- och lokalmodeller. Givet skillnaderna i representationen av Beberg är resultaten från den nya modellen i grova drag överensstämmande med SR 97. Ett mer rigoröst återskapande av modellen i SR 97, så som representation av förvarsblocken, kan förväntas ge ännu bättre överstämmelse mellan modellerna.

# Contents

# List of Figures

# List of Tables

# 1 Introduction

This report documents several developments to NAMMU, and associated tools, that were performed between end 1999 and January 2001. The testing of the enhanced software is described, and finally an application to assessment style modelling of the Beberg site is described. The application had several purposes. Firstly, to illustrate how the new facilities available in NAMMU could be used to construct a nested regional- and site-scale model, and what the advantages were over the methodology used in SR 97. Secondly, by performing Monte Carlo simulations of a stochastic model the robustness of the methods and their practical application could be assessed. Finally, the results were compared with the SR 97 Beberg model to verify the consistency of the methodology and software. An exact comparison was not expected since the model was not intended as an exact replica of SR 97, but as a demonstration of the new facilities using the SR 97 data. Hence, the results are expected to be broadly consistent and we make efforts to explain any differences.

Section 3 describes the developments performed and how they were tested, and where appropriate gives the user some practical advice on using the new facilities.

Section 4 describes the nested model of Beberg.

Section 5 presents the results for Beberg and compares them with SR 97.

Section 6 summarises what has been achieved and outlines potential areas for future work.

# 2 Background and Objectives

A number of generic issues relating to geosphere modelling have been recommended for further investigation during tasks carried out on the SR 97 safety assessment. Here we summarise these issues and suggest how they may be addressed. In particular, we consider how software tools, such as NAMMU, may best be applied and developed for SKB projects.

The main objectives of this study are to:

1. Develop methods for modelling continuum site-scale hydrogeological models nested within continuum regional-field models.

2. Include a facility for Implicit Fracture Zone (IFZ) representation within NAMMU to calculate the effective permeability of a grid block crossed by tabular features in a groundwater flow model.

3. Perform stochastic modelling with NAMMU using the Turning Bands algorithm and Monte Carlo simulations.

4. Generate fracture plane transmissivity as a stochastic 2D process in the plane of the fracture with the flexibility to condition on available transmissivity data.

5. Implement a new robust pathline algorithm based on calculation of a continuous velocity field with a dynamic time step set to avoid pathlines that terminate inside the model or oscillate between adjacent elements arising from a discontinuous field.

6. Verify the methods, and practicalities of their use, by comparison with the approaches used in SR 97.

7. Enhance visualisation capabilities (specifically Avizier for NAMMU) to improve graphical tools for presentation, interpretation and checking of models and their results.

The motivation for these developments is to extend the flexibility available to the modeller in representing physical processes and hydrogeological features, and hence improve the realism and accuracy of model predictions. In addition, approaches that may improve the efficiency of performing calculations shall be evaluated.

The benefits obtained from the new facilities are demonstrated by comparing with SR 97. For example, the ability to nest the regional- site-scale automatically, and to shape irregular grids on the regional and site scales to follow the natural hydrogeological boundaries.

# 3 Developments in methodology

## 3.1 Nesting

In SR 97, transport was considered on a site-scale of a few kilometres, while the conditions governing groundwater patterns were modelled on a regional-scale of tens of kilometres. Having two scales created the problem of how to nest the two models to ensure consistency (Follin, 1999; Walker and Gylling, 1998; Walker and Gylling, 1999). Nesting proved difficult due to the different modelling approaches adopted. For example, at Beberg the site-scale model used implicit fractures, stochastic continuum, steady-state freshwater flow on the site scale as opposed to explicit fracture zones, deterministic, transient salt transport on the regional-scale (Hartley *et al*., 1998).

Some of the uncertainties associated with these differences have been quantified (Marsic and Hartley, 2000) by considering variable density on the site-scale.

The natural solution to this problem is to embed the site-scale model within a regional-scale model, such that consistency of pressure and flux (and salt) is implemented numerically. Consistency in the geological representation on the two scales requires that structures which cross the interface are continuous and that a self-consistent upscaling method is used to obtain effective hydrogeological properties on a range of scales. This aspect is considered in the application in Section 4.

Options for formal nesting of the two scales are:

1. NAMMU continuum model using "constraints" to nest a refined site-scale model within a coarser far-field model. The method is called constraints as constraint equations are used to link the system variables at an interface such that the physical equations are honoured. A typical finite-element size for the site-scale model is about 30 m, for the far-field it is over 100 m, see Figure 3-1(a). The constraints facility allows the freedoms (or variables) located either side of an interface between two regions with differing refinement to be coupled by constraint equations. For groundwater flow, the constraint equations ensure continuity of pressure and mass balance. For salt transport, salinity is also continuous and the mass flux of salt is conserved. Due to the different element scales, the permeability field must be upscaled in a self-consistent method. That is, the effective permeability for a volume in the site-scale model needs to be consistent with an equivalent volume in the far-field.

2. CONNECTFLOW (Hartley *et al*., 2001) model with a Discrete Fracture Network (DFN) site-scale model nested within a continuum far-field model, see Figure 3-1(b).

The first of these two approaches has been enhanced and demonstrated in the current study (Section 3.2). The issue of ensuring continuity in the fracture zone structures is addressed by the improved IFZ method described in Section 3.3. Depending on the geological concept for the fracture network and size of a REV, for example, the second

approach may be viewed as either an alternative approach or combined with the first to give telescopic nesting with a canister-scale DFN model nested with the continuum site- and regional-scale models.

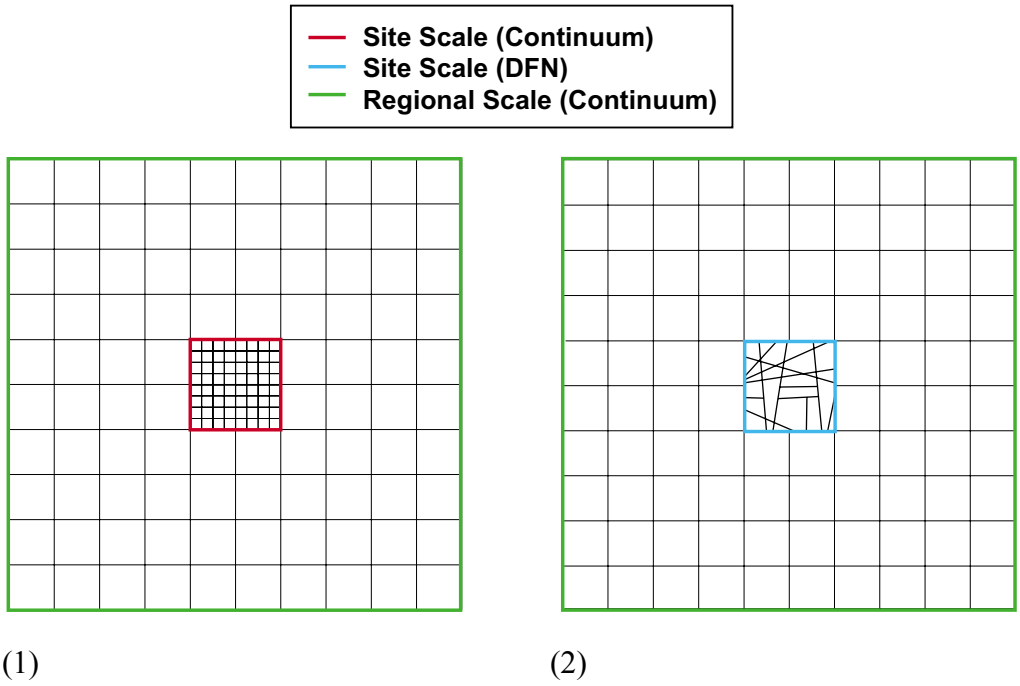


*Figure 3-1* *(1) Schematic view of a refined continuum site-scale model nested within a coarser continuum far-field model (NAMMU). (2) Schematic view of a Discrete Fracture Network (DFN) site-scale model nested within a continuum far-field model (CONNECTFLOW).*

## 3.2 Embedded grid ("Constraints")

Figure 3-2 illustrates an example of nesting of different scale finite-element meshes using constraints. Here a refined site-scale model (35m element-size) is joined to a coarser regional-scale model (105m). Hence, at the interface between the two scales one element in the regional-scale is adjacent to nine elements in the site-scale, and only every third node in the site-scale mesh is coincident with a node in the regional-scale. The other two nodes being 'pinch' nodes. To ensure that the physics of groundwater flow is maintained at this interface the finite-element equations for elements on the interface are modified using constraint equations. For pinch nodes in the site-scale, the pressure is set to the interpolation of the pressure in the adjacent regional-scale element to ensure continuity in the discrete system

$$Ps_i = \sum_j Ir_{ij}\, Pr_j$$

where $Ps_i$ is the residual pressure at the node $i$ on the site-scale side of the interface, $Pr_j$ is the residual pressure at node $j$ in the adjoining element on the regional side, and $Ir_{ij}$ is the finite element basis function evaluated in the regional-scale mesh for node $j$ and at

the position of node *i*. For the regional-scale element, an extra contribution to the flux entering the element is calculated from the integral of flux using Gaussian quadrature from the nine (in 3D) adjoining site-scale elements

$$\int_{S_s} \left( \underline{qs} - \underline{qr} \right) \cdot \underline{n} dS_s$$

where $\underline{qs}$ is the specific discharge in the element in the site-scale mesh, $\underline{qr}$ is the specific discharge in the element in the regional-scale mesh, $\underline{n}$ is the unit normal vector to the interface and $S_s$ is the surface of the element on the interface in the site-scale model. This ensures conservation of mass. Similar principles can be applied to more complex processes such as salt transport. This will be dealt with in a follow-up study.

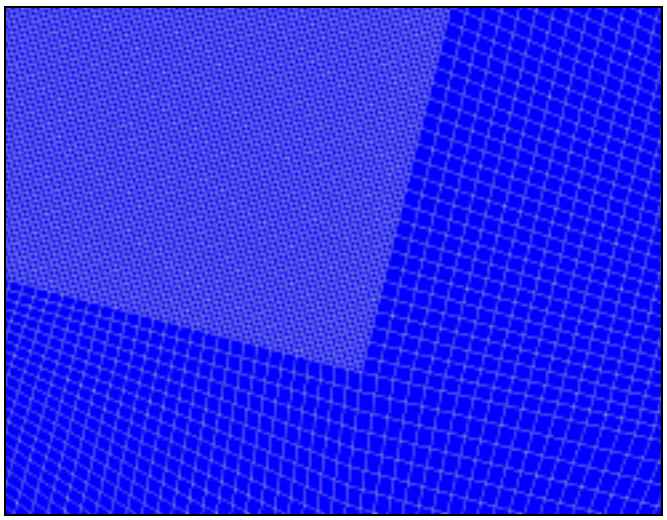

*(a)*

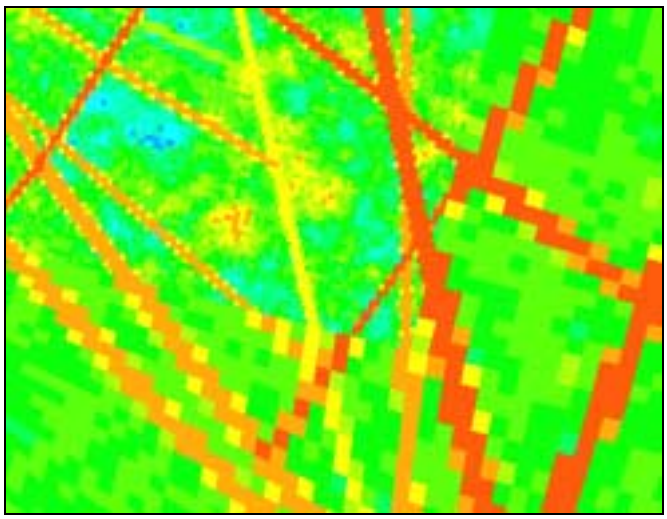

*(b)*

*Figure 3-2* *(a); Part of the finite element mesh showing the constraint boundary between the refined site-scale model and the coarse regional-scale model. (b); The same area shown with the stochastic permeability field ($K_{zz}$) for realisation 1. The fracture zones are implicitly represented in the model.*

## 3.3 Implicit representation of tabular features using IFZ

Here we detail a new method for calculating the effective permeability of a grid block in a model for groundwater flow in a domain containing tabular features. The method was based on the IFZ approach (Boghammar et al., 1997), but represents a very significant enhancement in the range of structures it can represent, how it handles fracture intersections, and is efficiency. The permeability of the background rock and the features may have arbitrary orientation, and the features may be more permeable, or less permeable than the surrounding rock. The approach is simple to implement and has low computational cost. The use of the method is illustrated by examples.

There are various approaches to modelling groundwater flow in domains containing tabular features. If the features are much more permeable, or more transmissive, than the background rock, the modelling can be undertaken using discrete fracture-network models (see for example, Hartley et al., 1998) in which each feature is represented by a planar 'fracture', and the background rock is not represented. Such models are easy to set up, and it is easy to change the numbers, positions and properties of the features. However, the features may not be that much more permeable or more transmissive than the background rock; or some features may act as barriers to flow across them; or some features may have a more complicated behaviour in that they act as barriers to flow across them, but in the directions along the larger extents of the feature are more transmissive than the surrounding rock. It may, therefore, be necessary to model the flow through the background rock as well as through the features. This can be done using fracture-network models, but it may be necessary to approximate the background rock in some way in terms of 'fractures'.

Another approach to the modelling is to use continuum porous medium models in which each tabular feature is represented by a group of finite elements chosen so that the boundaries of the feature lie along element boundaries. There are variants of this approach in which for example, the features are approximated using two-dimensional elements in a grid of three-dimensional elements. All of these approaches represent the flow in both features and the surrounding rock, and can handle the various types of features discussed above.

However, it is very difficult and time-consuming to set up the grids for such a model in three dimensions, and in general it is very difficult to automate the process of setting up the grid. This is particularly important if one wants to address the uncertainties, which will always exist, in the number and position of the features. This would be done by undertaking Monte-Carlo simulations. Realisations of the features would be generated numerically based on the available information about the features and then the flow would be calculated for each realisation. In this way, the uncertainty about the flow resulting from the uncertainties about the features could be quantified. However, if it were necessary to manually set up the grid for the numerical flow calculation for each realisation, it would only be practicable to undertake calculations for a very small number of realisations, which would limit the usefulness of the Monte-Carlo technique.

An alternative approach to modelling flow in a domain containing tabular features using continuum porous medium models is as follows. The finite-element (or finite-difference) grid is set up independently of the features. Typically, a simple cubic grid

might be used. Then for each element, or grid block, a suitable effective permeability would be determined, appropriate to represent the background rock and all the features crossing the element, or grid block. This approach is often used in finite-difference calculations, for example, because many finite-difference programs can only handle simple cubic grids. Variants of this approach have been proposed by, for example, Svensson (1999) and Lee et al. (2000). In fact, the approach is better suited to implementation in finite-element models as they allow an arbitrary direction of hydraulic anisotropy in the effective permeability to be specified. This is important since in the general case, the principal directions of the permeability tensor will differ from element to element according to the alignment of features that cross them. Another motivation for using simple cubic grids is in undertaking stochastic calculations to address the effects of heterogeneity in the background rock, because the statistical parameterisation may require that all elements or grid blocks have similar sizes.

The approach is particularly flexible. It can be readily automated, which makes it straightforward to undertake Monte-Carlo simulations to address the uncertainties in the number and position of the features. However, for a particular level of grid refinement, the flow calculated for an individual realisation would not be quite as accurate as that calculated using a grid chosen so that each feature is represented accurately by a number of finite elements, although this can be addressed by grid refinement.

The question then arises of how best to calculate the effective permeability for an element crossed by one, or more, tabular features. In this report, a new approach to this is presented. The approach has several very desirable features:

1. It allows the permeability tensors of the features and background rock to have arbitrary orientation, not necessarily aligned with the coordinate system or the grid blocks, and the resulting effective permeability tensor to have arbitrary orientation. This is likely to give better results than approaches in which the principal axes of the permeability tensors are constrained to be aligned with the coordinate axes, noting that neither the features nor their permeability tensors are likely to be aligned with the coordinate axes in general.

2. It can handle features that are less permeable than the background rock and act as barriers to flow in one direction.

3. It can handle cases in which more than one features crosses a block. This is done in such a way that the resulting effective permeability is not dominated by the contribution from the most transmissive feature. Rather, the approach uses a priority order for the features so that cases in which the behaviour of a grid block is controlled by a feature that is less permeable than the background rock can be set up and handled. The priority order is set on a feature by feature basis rather block by block, and is specified manually by the user. For example, the order could correspond to the geohistory of the features, or by ascending transmissivity to give a conservative model.

4. The approach is very flexible and simple to implement, and the computational cost of calculating the effective permeabilities is not high.

### 3.3.1 Method

The starting point for the method is a specification of the tabular features. For definiteness here, they are taken to have a rectangular shape. Each feature could be described by, for example:

a) the position of its centre;

b) the orientation of a coordinate system aligned with the feature, which would be defined by three angles;

c) the extent of the feature in the three coordinate directions for the coordinate system aligned with the feature.

An order of priority for the features also needs to be provided. It is taken that where two, or more, features cross, the rock in the intersection region has the property of the highest priority feature, rather than the most permeable. This corresponds to the view that the rock has the property of the most recent feature crossing it, with the priority order corresponding to the order in which the features developed.

The basic idea of the approach is to successively consider the features crossing a block in order of priority. At each step, the effect of the feature in question is combined with the effective permeability that represents the combined effect of the background rock and lower priority features to give a new effective permeability. The end result is an effective permeability that represents the combined effect of all the features and the background rock.

In each step:

1. The volume of intersection between the feature and the block is determined;

2. The effective permeability tensor that represents the combined effect of the background rock and features with lower priority than the one under consideration is determined in the coordinate system aligned with the feature.

3. The effective permeability tensor that includes the effect of the feature under consideration is determined in the coordinate system aligned with the feature;

4. The effective permeability tensor that includes the effect of the feature is determined in the original coordinate system.

In principle, determining whether a tabular feature crosses a grid block, and evaluating the volume of intersection are straightforward geometric analyses. However, many different cases have to be considered. Therefore, an approximate approach is adopted that is much easier to implement, but is considered to give an acceptable accuracy, bearing in mind that there will be discretisation errors in the numerical calculation of the groundwater flow. From the corners of each block, it is determined whether or not the feature intersects the block. For a feature that does intersect the block, a regular lattice of points lying within the block is considered. Typically, this lattice might include of the order of 1000 points (resulting from subdivision of the block into ten in each coordinate

direction). Then for each point in the lattice, it is determined whether it lies in the feature. The intersection volume is then taken to be given by the volume of the block times the fraction of the total number of points in the block that lie within the feature.

The calculation of the effective permeability tensor that represents the background rock and lower priority features in the (rotated) coordinate system aligned with the feature is straightforward. It just involves pre- and post-multiplication of the permeability tensor in the original coordinate system by the appropriate rotation matrix and its transpose respectively. Similarly, once the combined effective permeability of the block and the feature under consideration has been determined in the coordinate system aligned with the feature, it is straightforward to determine the effective permeability tensor in the original coordinate system by pre- and post-multiplication of the permeability tensor with, respectively, the transpose of the rotation matrix and the rotation matrix itself.

The key step in the algorithm is the determination, in a coordinate system aligned with the feature, of an effective permeability that represents the combined effect of the feature under consideration and the effective permeability of the background rock and lower priority features. The desired effective permeability is approximated by the effective permeability of a modified block, which is obtained by rotating the original grid block to be aligned with the feature, keeping the volume of intersection of the block and feature the same as for the original block (see Figure 3-3). Without loss of generality, the intersection region is taken to occupy the bottom part of the modified block. For the modified block, it is possible to calculate the effective permeability using simple algebraic expressions. This method of effectively reshaping the volume of the tabular feature within the block implies that for features that truncated within the block will be extended across the block, albeit their volume will be maintained. This is clearly an approximation, but one that will not be significant providing the block size is small relative to the length of the features. In order to consider the situation where features are sub-block size or for greater accuracy, then a DFN approach should be used instead.

It should be noted that in general, the effective permeability of the background rock and lower priority features will not be aligned with the modified block. Even if the background rock has an isotropic permeability, the effect of taking into account features of lower priority than the one under consideration would be to produce an effective permeability that is unlikely to be aligned with the feature under consideration. (It should be noted that use of the appropriate full permeability tensor is likely to be much better than the use of an approximate tensor with principal axes aligned with the original coordinate system.) Therefore, in the analysis, the possibility is allowed for that the effective permeability of the modified block and lower priority features has an arbitrary orientation. For maximum flexibility, the possibility that the permeability of the feature has an arbitrary orientation is also allowed for.

The effective permeability of the modified block is determined as follows. For an overall head gradient in each coordinate direction, the flows through the faces of the block are calculated. The effective permeability is the permeability tensor of a homogeneous, anisotropic block that would give the same flows for these overall head gradients.

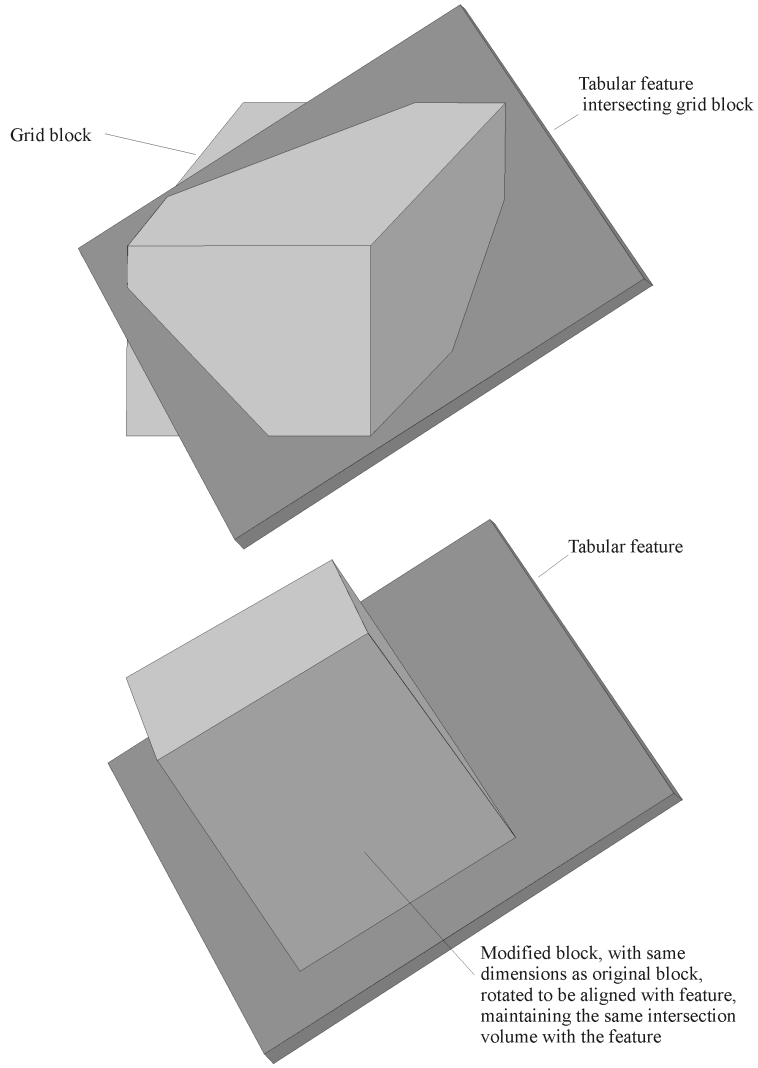


*Figure 3-3 Derivation of the modified block.*

It is necessary to consider what is meant by the overall head gradient being in a given direction, bearing in mind that the head gradient within the block will not be uniform, but will vary because of the differing permeabilities of the feature and the rest of the block. It is considered that an appropriate way in which to interpret this is to take the boundary conditions on the faces of the block to be a combination of an overall head gradient in the given direction and a variation that is periodic, with the period in each direction being given by the length of the side of the block in that direction. That is the head variation over one face is taken to have the same shape as the head variation over the opposite face, but shifted by a certain amount. (This effectively corresponds to considering groundwater flow in a medium consisting of the block repeated indefinitely in each direction.)

Using an overall head increment of $\Delta_x$ in the $x$-direction, $\Delta_y$ in the $y$-direction and $\Delta_z$ in the $z$-direction the boundary conditions on the block vertices and on the tabular feature surface are set as shown in Figure 3-4(a), (b) and (c) respectively. As indicated, the head is taken to vary linearly between the points at which its value is specified. This exploits

the knowledge that a linearly varying head gives a solution to the groundwater flow equation for a homogeneous permeability field. Thus, the head distributions shown in Figure 3-4 satisfy the flow equations within the feature and the rest of the block. The effective permeabilities are calculated by firstly determining the value of each of the head values $\Delta^*_x$, $\Delta^*_y$ and $\Delta^*_z$ such that appropriate boundary conditions are satisfied on the interface between the feature and the rest of the block. For groundwater flow, the desired conditions are that the head is continuous across the interface (which is satisfied for the head distributions shown in Figure 3-4), and that the normal component of the specific discharge (Darcy velocity) to the interface is continuous.

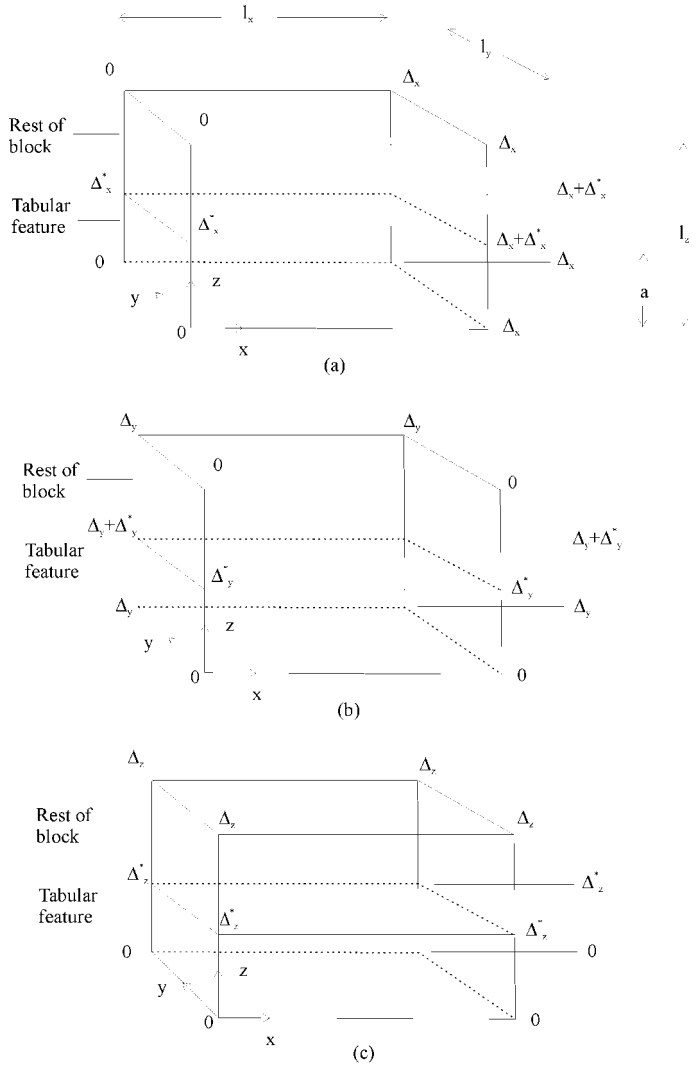


*Figure 3-4* *The boundary conditions for the calculation of the components of the effective permeability tensor (in the coordinate system aligned with the feature, and the modified block) for an overall head gradient in (a) the* x*-direction, (b) the* y*-direction (c) the* z*-direction. The head gradients are indicated by showing the value of head at the vertices of the block and on the surface of the tabular feature in terms of head increments* $\Delta_x$, $\Delta_y$, $\Delta_z$.

It is straightforward to determine the required values of $\Delta^*_x$, $\Delta^*_y$ and $\Delta^*_z$. Then the flows through the faces of the block can be determined, and by matching these to the flows through a homogeneous anisotropic block with the same dimensions and the same overall head gradient, the components of the effective permeability tensor, $k^e$, can be determined. The end result is

$$k^{\mathrm{e}}_{zz} = \frac{l_z}{\left( \dfrac{a}{k^{\mathrm{f}}_{zz}} + \dfrac{(l_z - a)}{k^{\mathrm{b}}_{zz}} \right)} \ . \tag{1}$$

$$k^{\mathrm{e}}_{xz} = \frac{a}{l_z}\frac{k^{\mathrm{f}}_{xz}}{k^{\mathrm{f}}_{zz}} k^{\mathrm{e}}_{zz} + \frac{(l_z - a)}{l_z}\frac{k^{\mathrm{b}}_{xz}}{k^{\mathrm{b}}_{zz}} k^{\mathrm{e}}_{zz} \ . \tag{2}$$

$$k^{\mathrm{e}}_{yz} = \frac{a}{l_z}\frac{k^{\mathrm{f}}_{yz}}{k^{\mathrm{f}}_{zz}} k^{\mathrm{e}}_{zz} + \frac{(l_z - a)}{l_z}\frac{k^{\mathrm{b}}_{yz}}{k^{\mathrm{b}}_{zz}} k^{\mathrm{e}}_{zz} \ . \tag{3}$$

$$k^{\mathrm{e}}_{xx} = \left( \frac{a}{l_z} k^{\mathrm{f}}_{xx} + \frac{(l_z - a)}{l_z} k^{\mathrm{b}}_{xx} \right) - \frac{a}{l_z}\frac{(l_z - a)}{l_z}\frac{k^{\mathrm{e}}_{zz}}{k^{\mathrm{b}}_{zz} k^{\mathrm{f}}_{zz}} \left( k^{\mathrm{f}}_{xz} - k^{\mathrm{b}}_{xz} \right)^2 \ . \tag{4}$$

$$k^{\mathrm{e}}_{yx} = \left( \frac{a}{l_z} k^{\mathrm{f}}_{yx} + \frac{(l_z - a)}{l_z} k^{\mathrm{b}}_{yx} \right) - \frac{a}{l_z}\frac{(l_z - a)}{l_z}\frac{k^{\mathrm{e}}_{zz}}{k^{\mathrm{b}}_{zz} k^{\mathrm{f}}_{zz}} \left( k^{\mathrm{f}}_{yz} - k^{\mathrm{b}}_{yz} \right)\left( k^{\mathrm{f}}_{xz} - k^{\mathrm{b}}_{xz} \right) \ . \tag{5}$$

$$k^{\mathrm{e}}_{yy} = \left( \frac{a}{l_z} k^{\mathrm{f}}_{yy} + \frac{(l_z - a)}{l_z} k^{\mathrm{b}}_{yy} \right) - \frac{a}{l_z}\frac{(l_z - a)}{l_z}\frac{k^{\mathrm{e}}_{zz}}{k^{\mathrm{b}}_{zz} k^{\mathrm{f}}_{zz}} \left( k^{\mathrm{f}}_{yz} - k^{\mathrm{b}}_{yz} \right)^2 \ . \tag{6}$$

where

$k^{\mathrm{f}}$ is the permeability tensor for the feature, with components $k^{\mathrm{f}}_{xx}$, $k^{\mathrm{f}}_{yy}$, $k^{\mathrm{f}}_{zz}$, $k^{\mathrm{f}}_{xy}\ (=k^{\mathrm{f}}_{yx}), k^{\mathrm{f}}_{yz}\ (=k^{\mathrm{f}}_{zy}), k^{\mathrm{f}}_{zx}\ (=k^{\mathrm{f}}_{xz})$.

$k^{\mathrm{b}}$ is the permeability tensor for the rest of the (modified) block, with components $k^{\mathrm{b}}_{xx}$, $k^{\mathrm{b}}_{yy}$, $k^{\mathrm{b}}_{zz}$, $k^{\mathrm{b}}_{xy}\ (=k^{\mathrm{b}}_{yx}), k^{\mathrm{b}}_{yz}\ (=k^{\mathrm{b}}_{zy}), k^{\mathrm{b}}_{zx}\ (=k^{\mathrm{b}}_{xz})$

$l_x$, $l_{\mathrm{y}}$, $l_z$ are the lengths of the sides of the (modified) block;

$a$ is the thickness of the representation of that part of the feature crossing the (modified) block.

The expressions in equation (1) to (6) are the components of the effective permeability tensor in the rotated coordinate system aligned with the block. The components in the original coordinate system are determined by an appropriate rotation. Only the derivation of an effective permeability has been considered here. For transport or transient situations, an effective porosity can also be calculated. This requires that volumes of fracture and rock mass be calculated and then combined appropriately with the feature and rock mass porosities. Although this is straightforward to implement, different porosities may be required for different applications, such as a total porosity

for transient calculations, but just the fracture porosity for a conservative calculation of transport. The calculation of effective porosities will be treated.

### 3.3.2 Examples

The use of the approach is illustrated below for three examples. The first example is that of a single feature crossing a block with much lower permeability. The block was taken to have side 1000m, and it was modelled with a 40×40×40 grid of tri-linear finite elements. The feature was taken to pass through the centre of the block, and the length of its intersection with the end faces of the block was taken to be 200m. Several different orientations of the feature and two values of the thickness (50m, and 6.25m) were considered. For this example, the groundwater flux through the domain for a specified head difference across it can (approximately) be calculated analytically. In Table 3-1, the ratio of the numerically calculated flux to the analytically calculated flux is presented for the variants considered. As can be seen, the method generally performs well. The worst case is that of a very thin feature that is parallel to the axes of the block. For this case, the error is approximately 20%. Most of this error is due to errors in the approximation of the volume of intersection of the feature with grid blocks. For the coarse lattice used in the calculation, 10 points in each block axial direction with a spacing of 2.5m, these errors are relatively large for a feature that is thin or at shallow angles to the coordinate axes. The errors could be reduced by the use of a finer lattice, although this would increase the computational cost. A feature thinner than the spacing of points in the lattice would not be treated.

| ***Feature Orientation*** | | ***Feature Thickness*** | |
|---|---|---|---|
| ***Strike*** | ***Dip*** | ***50m*** | ***6.25m*** |
| 0° | 90.0° | 1.001 | 1.200 |
| 0° | 70.7° | 0.871 | 0.846 |
| 0° | 51.3° | 0.993 | 1.077 |
| N45°E | 41.5° | 1.071 | 1.083 |

*Table 3-1 Ratio of numerically calculated flux to analytically calculated flux.*

The second and third examples are simple cases with a very small number of features. These models are effectively two-dimensional, in that the geometry and properties of the model are independent of the *y*-coordinate. The second example, which is illustrated in Figure 3-5, shows the effect of three connected features that are much more permeable than the surrounding rock. The features all have the same permeability. The third example, which is illustrated in Figure 3-6, shows the effects of two features that are much less permeable than the surrounding rock arranged so that the flow follows a contorted path around the features. As can be seen from Figure 3-5 and Figure 3-6 the calculated flow in both cases is realistic. In the second example, the calculated flow follows the network of features. The head falls off linearly along the network of features, as it should. In the third example, the calculated flow detours around the features.

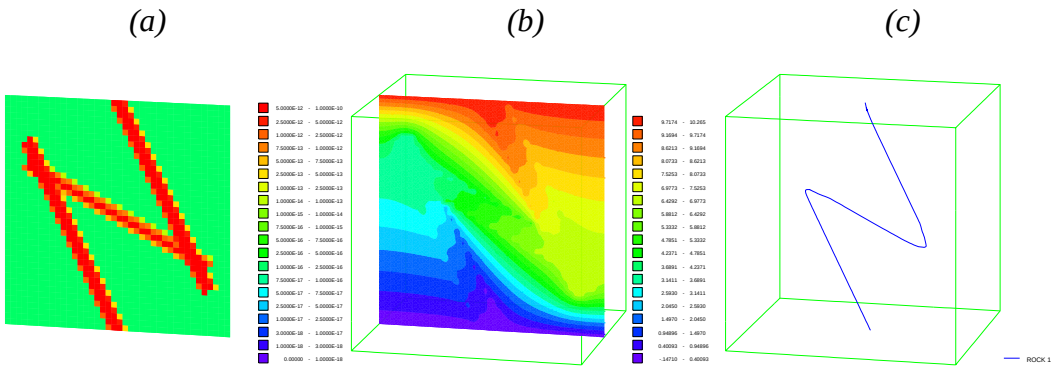


*Figure 3-5* *Effective permeability, calculated head and flow for the second example: (a) effective $K_{zz}$ permeability ($m^2$) on a slice in the x-z plane; (b) calculated head (m) on a slice in the x-z plane; (c) pathlines.*

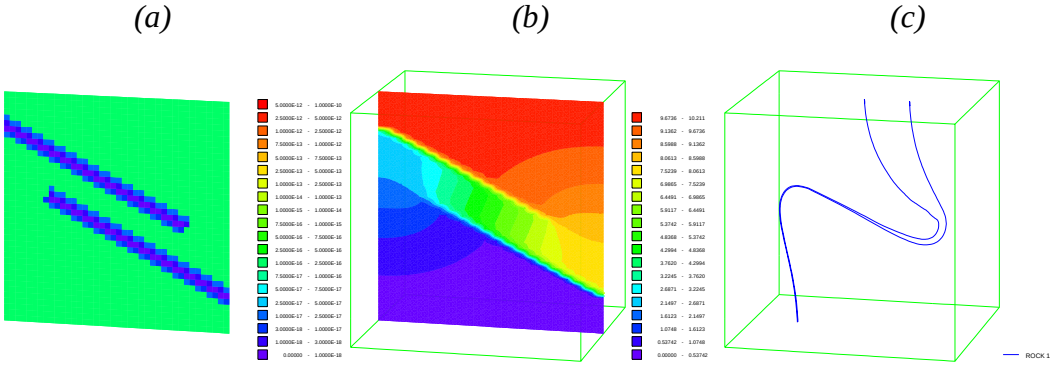


*Figure 3-6* *Effective permeability, calculated head and flow for the third example: (a) effective $K_{zz}$ permeability ($m^2$) on a slice in the x-z plane; (b) calculated head (m) on a slice in the x-z plane; (c) pathlines.*

### 3.3.3 Discussion

An approach for calculating the effective permeability of a grid block in a domain crossed by tabular features has been described above. The approach has many desirable features, such as:

1. It clearly gives the appropriate result in cases in which the features are aligned with the grid blocks and features do not intersect within a grid block. The method represents a sensible generalization from such cases to deal with features that have arbitrary orientation and the permeability tensors of the features and the surrounding rock have arbitrary orientation.

2. The method can handle cases in which the features are less permeable than the background rock and so act as barriers to flow.

3. It can handle cases in which more than one feature crosses a block. This is done in such a way that the resulting effective permeability is not dominated by the contribution from the most transmissive feature. Rather, the approach uses a priority order for the features (corresponding to their order of development) so that cases in which the behaviour of a grid block is controlled by a feature that is less permeable than the background rock can be set up and handled.

4. The method is ideally suited for stochastic models intended to address the uncertainty about the number and position of the features, because it uses a grid that is not determined by the position of the features, but which can be specified at the start of the calculations. The method can also be used in stochastic calculations to address heterogeneity within the features or the background rock.

5. It is easy to refine the grid, so that specific features can be represented accurately.

6. The method is straightforward to implement, and its computational cost is low. As can be readily seen from the discussion in Section 3.3.1, the computational cost has two main components. The cost of determining which elements are crossed by one or more features is essentially proportional to the number of elements times the number of features. The cost of evaluating the effective permeabilities for the blocks crossed by features is essentially proportional to the total number of intersections of features with blocks. In general, the cost will be much smaller than the cost of calculating the flow.

7. The approach is very flexible, and allows for example, the treatment of a model that is sometimes suggested for faults, in which the fault has an inner core that may be transmissive in the plane of the fault, but may, due to the presence of fault gouge, act as a barrier to flow across the fault, and an outer core that is more transmissive than the background rock due to a greater density of fractures. The effective permeability tensor for the outer zone need not be aligned with the plane of the fault. This allows cases to be addressed in which the fracturing is controlled by the rock fabric, or the stress field, rather than the fault itself. Such a model would simply be treated by taking each fault to be represented by three features with appropriate properties.

In summary, the approach presented is considered to be a very effective and powerful approach, that is straightforward to implement, has low computational costs, and has many desirable features.

## 3.4 Stochastic modelling

Applications of NAMMU within SR 97, and more recent SKB work (Marsic and Hartley, 2000), have all used deterministic continuum models. The ability to efficiently perform stochastic simulations is a further requirement, and this needs to be possible for both linear systems (e.g. constant-density groundwater flow) and non-linear systems (e.g. coupled variable-density flow and salt transport). For this purpose the generation of stochastic permeability fields in NAMMU has been implemented based on pre-existing methods used in the TBCODE software. This is based on the Turning Bands method. TBCODE has been used and tested extensively as part of the GEONAM

module that was used in comparisons with HYDRASTAR (Morris and Cliffe, 1994) and on the WIPP2 test case (Cliffe and Jackson, 1993). The stochastic continuum approach requires that tens or hundreds of Monte-Carlo realisations be performed of essentially the same hydrogeological system. Therefore, care was taken to ensure that the stochastic continuum method was implemented efficiently.

The methodology allows a good deal of flexibility in the stochastic modelling. The rock mass and individual fracture zone domains can have independent statistical parameters, and the domains can be defined as stochastic or deterministic independently. By treating the rock mass and fracture zones as independent domains this method contrasts to HYDRASTAR where the spatial process is continuous and 'trends' (scaling of the local conductivity) are used to represent the fracture zones. The stochastic methods for the rock mass are described in this section. The stochastic methods for the fracture zones are described in Section 3.6. Currently, simulations are unconditioned. Conditioning of the rock mass or fracture domains would be straightforward to implement numerically, but careful consideration needs to be given to how the data is defined, for example on what rock volume the data is defined and whether it is associated with a particular zone or just a borehole interval.

For this study, unconditioned realisations of the rock mass were based on an exponential variogram, and combined with deterministic fracture zone properties using IFZ. It may be desired to have different statistical parameters in different parts of the model. For example, a median permeability that decreases with depth. Another important possibility is to have different statistics for the regional- and site-scale domains since different values will be obtained for upscaling to the different mesh sizes. Generally, the larger the grid size, the higher the median and the smaller the variance until a REV is reached. This creates a choice as to whether to use a continuous spatial process or have a number of discrete spatial processes for the different parts of the model. This decision depends on which is most consistent with the geological model. For the crystalline rocks of interest to SKB it was considered that the continuous process was the more appropriate since variations in statistical properties are generally associated with trends rather than absolute discontinuities at lithological boundaries, for example.

Hence, the approach was to use a single Gaussian spatial process with a uniform correlation length, and normalised to have zero mean and variance 1.0. This generated normalised field was then rescaled by the mean and variance parameters for the discrete parts of the model. Thus, the different upscaled mean and variance parameters could be applied to the regional- and site-scale regions, but in a way that a high permeability in the regional-scale would generally be adjacent to a high permeability in the site-scale near the interface. This avoids having artificial barriers to flow around the boundary of the site-scale model due to discontinuities in the spatial process. NAMMU also allows anisotropic permeabilities to be defined. For the stochastic case, this was implemented by scaling the normalised spatial process by different factors for the different components of the permeability tensor. Different degrees of anisotropy can be defined for different domains.

## 3.5 Solvers

The standard solver in NAMMU uses a direct frontal method that is robust in terms of being able to solve a wide range of numerical systems even when poorly conditioned (for example, very heterogeneous models). The disadvantage of this method is that the required CPU time and memory scale poorly with the number of freedoms. Generally, the method is practicable for discrete systems up to a few hundred thousand freedoms. Site-scale models used in SR 97 used grids in the order of 1 million nodes, and hence the direct solver would not be able to perform similar calculations. For this reason, iterative solvers were incorporated in NAMMU. These generally use much less CPU and memory for large models. Factors of a thousand are possible for systems with 1 million freedoms. Two alternative preconditioned conjugate gradient methods were implemented: generalised minimum residual (GMRES) and stabilised biconjugate gradient (BICSTAB). Both methods can solve non-symmetric discrete systems. BICSTAB is generally faster and uses less memory but can diverge. GMRES seems to be slightly slower but should be more stable, even if it needs more iterations to converge. For the Beberg example both solvers performed well. It is important to note that the number of iterations increases as the heterogeneity of the permeability field increases or as the correlation length decreases. Generally, the discrete system becomes difficult to solve when the range of permeability values exceeds eight or nine orders of magnitude. Hence, if the geological model has a large variability, a variance greater than about 2.25 in the $\log_{10}$ of permeability, then numerical problems may be encountered. In such cases, consideration should be given as to whether a lognormal distribution of permeability is an appropriate model of reality, and in particular whether the values predicted by the tails of the distribution are observed in reality. A practical remedy is to truncate the distributions at the maximum and minimum observed permeability values upscaled to the appropriate volume.

## 3.6 Generation of 2D Stochastic Permeability in Fracture Zones

The SR 97 stochastic modelling represented fracture zones by 'trends' in a continuous field. The permeability within the fracture zones being modified according to the upscaled median permeability for each fracture zone. However, the properties of individual fracture zones had been interpreted statistically in Walker et al. (1997), and so an alternative model is to treat each of identified conductor domains as an independent volume with its own statistical properties. This stochastic model was implemented in NAMMU. Each fracture zone is modelled by a 2D spatial process using the Turning bands method and based on an exponential variogram with specified mean, variance and correlation length. The mean variance can be specified to vary with depth based on a piecewise constant depth zonation. This can be done for arbitrary polygonal planar fractures. The 2D field is generated on a rectangular grid with specified mesh spacing covering the fracture zone area. Hydraulic anisotropy on the fracture plane can be achieved by specifying a different median value for the longitudinal (along the fracture) and transverse (through the fracture) directions. The same standard deviation is used for both components, and the two components are correlated with a fixed ratio. Once the 2D fracture field has been generated it is then combined with the 3D rock mass field (stochastic or deterministic) for each finite-element. An appropriate choice

for the mesh spacing used for the fractures is the average element size in the region it is located. Hence, fracture properties need to be upscaled to the same grid size as the rock mass. Figure 3-7 shows an example of stochastic fractures. Two vertical irregular shaped fractures are generated in a homogeneous rock mass with the same mean and variance but different correlation lengths. Based on flow for a uniform vertical head gradient, pathlines were calculated through the two fractures. The results show the expected behaviour. The permeability on the fracture with a small correlation length (the triangular fracture) is less smooth and the pathlines meander through the region of high permeability. The method is applied to Beberg as described in Section 5.10.

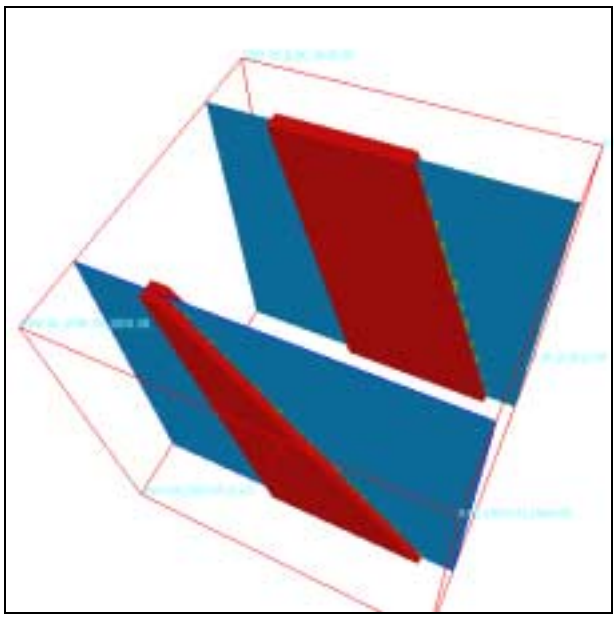

*(a)*

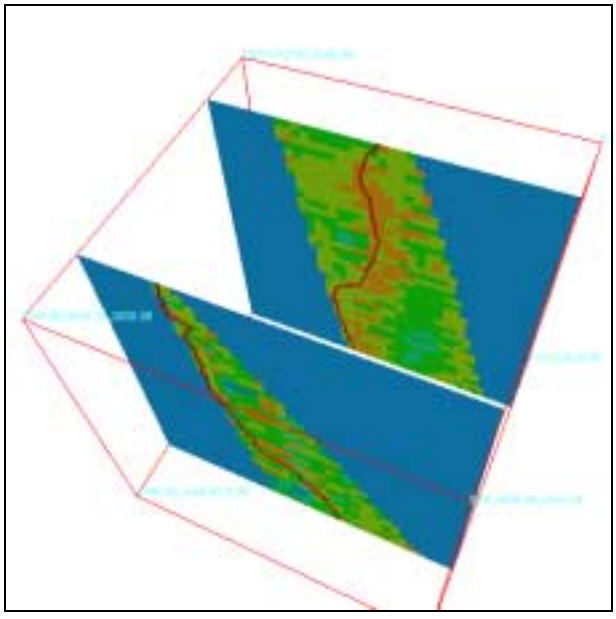

*(b)*

*Figure 3-7* *A two plane example of IFZ with stochastic fractures, and a uniform low permeability rock mass: (a) the fracture volumes (red) and two vertical slices through the rock permeability distribution. The fractures have an irregular shape, triangular and trapezoidal, to demonstrate the capability to represent non-rectangular zones; (b) the effective permeability on two vertical slices through each of the fractures. The correlation length is larger in the trapezoidal fracture than the triangular. Two pathlines are shown for a vertical pressure gradient.*

## 3.7 Visualisation (Avizier for NAMMU)

NAMMU exports a results file to the Avizier for NAMMU 3D visualisation environment. It is a very useful tool for understanding and presenting the results of large 3D models, as well as checking models during their construction. Several enhancements were made to Avizier for NAMMU during the current project. These include:

- improved efficiency for large models (1 million nodes);
- a module to import (in IFZ format) and display the fracture zones, and allow them to be drawn semi-transparent;
- import pathline start points from a file, and export the results to a file;
- import a large number of 'objects' to be displayed. These are used to indicate pathline start points and exit points, for example.

## 3.8 PROPER interface

A facility has been added to NAMMU to export the results of pathline calculations for up to 5,000 canister locations to a file in the PROPER format. This file contains a record for each realisation and canister that records the canister multiplicity, travel time, canister flux and exit location.

## 3.9 Improved pathlines

Some problems have been detected in the current pathline algorithm for stochastic continuum models with large variability or large contrasts between fractures and the rock mass. The problem arises from an inherent feature of the standard finite-element equations that calculate a velocity field that is not pointwise continuous across element boundaries. This is because the standard method of evaluating velocity is to interpolate pressure gradients using basis functions whose gradient is non-continuous. The resulting velocity discontinuities lead to the potential for pathlines to oscillate between elements or to cycle around adjacent elements. These effects can be exaggerated by a lack of numerical accuracy in the solution for partially converged solutions, such as those obtained from coarse meshes or poorly converged iterative solution schemes.

In order to remedy this problem two issues need to be addressed. The first is to choose time-steps dynamically as particles move along a trajectory that accounts for variability in both the magnitude of flow and element size in the general case of distorted finite-element meshes. Currently NAMMU uses a predictor-corrector algorithm for choosing the time-step that can lead to the selection of small time-steps to resolve very localised variations in velocity within single elements. The second issue is to develop an alternative method of interpolating the velocity field from the calculated pressure solution that ensures continuity. The first issue was solved by choosing the time-step such that particles move a specified distance relative to the current element, say half an element size. This is achieved by calculating the velocity in the transformed localised element geometry. In doing this, the algorithm ensures that particles are effectively

moving from one element to its neighbour without stepping or jumping over an element, due to a localised high velocity for example, or making unnecessarily small steps. The solution tried for the second issue of velocity continuity was to calculate a velocity field within each element by averaging the total flux across adjacent element faces to calculate a mean normal and tangential velocity for each element face, and then use linear interpolation of the velocity between opposite element faces. The new algorithm was tested on the second and third examples described in Section 3.3.2 and on the Beberg model. For the simple examples, the new algorithm gave more accurate pathlines that were more robust to grid resolution and numerical parameters, but particles still became stuck around the low permeability fractures in the third example. This suggests that the suggested interpolation method of velocity is not robust for all cases. For Beberg the new pathline algorithm gave very similar results to those for the original algorithm because a fine-scale grid was used for the local-scale region, which resolves spatial variations in the velocity field. Since the new algorithm was not robust for all cases, this area remains a topic for future research.

# 4 Application to Beberg nested model

The following two sections summarise the application of the new methodology to Beberg and compare the results with the SR 97 site-scale modelling.

## 4.1 Model Domain

The model used in the present study covers the same area as the regional Beberg model in SR 97. It extends from Örbyhus in the west 16 km to Dannemora in the east and from Silbo in the north about 10 km to the southern shore of Lake Finnsjön, see Figure 4-1. The model extends down to a depth of z = -1505 m which corresponds to the site-scale model of SR 97 but is slightly shallower than the regional model which reached a level of z = -2000 m. The top nodes of the uppermost element in the mesh were adjusted in the vertical direction according to the topography.

The NAMMU CB08 8 node cuboid element type was used in the finite-element mesh. A total number of 787 416 elements were used in the mesh. 632 016 of these were placed in the refined site-scale model nested inside the coarse regional-scale model. The dimension of each element in the site-scale model is 35×35×35 m which corresponds to the element size used in the site-scale model for Beberg in SR 97. Along the constraint boundary between the regional and the site-scales the size of the elements in the regional model is 105×105×105 m i.e. a factor 3 larger in each direction compared to the site-scale elements. Moving away from the constraint boundary the size and shape of the regional-scale elements may vary as the boundary is shaped to fit potential flow divides, but stay approximately cubed. The refined site-scale model extends from the top of the model to the bottom. The extension of the refined site-scale model in this study is 105 m shorter in the east-west direction compared to the site-scale model in SR 97. The change was needed because of the placement of some fracture intersections right at the constraint boundary, which cause convergence problems trying to solve the equations.

## 4.2 Permeability Field

In the present study, the permeability field was generated stochastically using the Turning Bands method for a set of 100 realisations. A Monte Carlo technique was used to perform the simulations. The site-scale modelling in SR 97 was carried out using the same techniques as implemented in HYDRASTAR.

The rock matrix was divided into two horizontal layers with different permeability. The permeability is changed in a stepwise manner at z = -35 m where it is reduced by a factor of 12.3 for the rock below. In the site-scale model in SR 97, the change occurred at z = -100 m but the factor of 12.3 was the same. The permeability values used for the refined site-scale model in the present study are the same as the ones used in SR 97. However, there is a significant difference between the two models local to the repository. In SR 97, the repository area was divided into two separate rock blocks (the Northern and the Southern Rock Blocks separated by Zone 1) both with higher

permeability than the surrounding rock. Due to simplifications of the model in the present study, these rock blocks have not been represented in the permeability field. Thus, the rock in the repository area in this model has the same statistical properties as the rest of the surrounding rock inside the site-scale model.

In the coarse regional-scale model surrounding the site-scale model the permeability was upscaled to the larger element size (approximately 100 m compared to 35 m in the site-scale model). The upscaling was done using an empirical scaling relationship developed by Rhén et al. (1997), which was also used in SR 97. The same stepwise change in permeability as in the refined part of the model was also used in coarse regional-scale, see Table 4-1.

| **Layer** | | **Mean -$\log_{10}$ *K* *[m/s]*** | **$\log_{10}$ *K Variance*** |
|---|---|---|---|
| Site model 35 m scale | 0 -> -35 m | 8.25 | 0.69 |
| | -35 -> -1505 m | 7.16 | 0.69 |
| Regional model 100 m scale | 0 -> -35 m | 6.81 | 0.21 |
| | -35 -> -1505 m | 7.90 | 0.10 |

*Table 4-1* *Conductivity values and the corresponding variances used generating the stochastic conductivity field for the different layers and scales in the model.*

The fracture zone representation used in the present study is a slightly simplified combination of the fracture zones used in the regional and the site-scale models in SR 97, see Figure 4-1 (the scale shown is about 20km by 20km), Figure 4-2 (the scale-shown is about 7km by 8km) and Table 4-2. One of the most significant changes is the representation of Zone 2, where only a single layer is used in the present study whereas it was split into three layers with different permeabilities in SR 97. In this way, a sandwich construction was achieved with high horizontal transmissivity and low vertical transmissivity. The absence of the more detailed Zone 2 might affect the results in this study.

A correlation length of 150m (practical range 450m) was used generating the stochastic permeability field for both the site-scale and regional-scale models in the present model, which compares to a correlation length of approx. 80m (practical range of 247m) for the SR 97 site-scale model. The reason for choosing a larger correlation length in the present study is that the element size in the regional scale is approximately 100m compared to 35m for the SR 97 site-scale model. If the correlation length is shorter than the typical element length (grid spacing), the correlation in permeability between elements will not be captured. Thus, keeping the correlation length at 80m would give us an uncorrelated permeability field in the regional scale. Even with 1.5 elements per correlation length, as in the present study, the full correlation may not be captured.

The general approach for calculating the stochastic permeability field is as follows:

- First, the rock mass is assigned a homogenous deterministic isotropic permeability corresponding to the values given in Table 4-1.

- Second, the stochastic field is generated with the Turning Bands method using the variance of the permeabilities in Table 4-1.

- Finally, the fracture zones are implicitly defined as deterministic features with the IFZ method and combined with the stochastic rock mass to give an anisotropic equivalent permeability, see section 3. The properties listed in Table 4-2 were used.

Figure 4-3 presents a regional view of the nested model showing the stochastic permeability field ($K_{zz}$) for realisation 1. The red colour indicates higher permeability and the green/blue colour indicates lower permeability. The fracture zones are implicitly represented in the model and it is clear that no undesirable cut-off's occur in the intersection between crossing fractures. This is accomplished by inserting the fractures in an order of increasing permeability. In this way the averaged permeability for each element in the model crossed by more than one fracture never blocks the flow through another fracture since the averaged permeability will have properties resembling the latest fracture (i.e. the most permeable). If desirable, it is possible to order the fractures so that less permeable fractures are inserted upon more permeable and thereby in effect cut off the flow in the previous fracture.

Some of the regional fracture zones pass through the site-scale model. Due to different element sizes in different parts of the model, the width (visually) of the fracture changes when a fracture crosses the constraint boundary and the effective permeability of the elements in the fracture decreases when the element size increases. This can be seen in Figure 4-3 and Figure 4-4. Another feature of Figure 4-3 is the fracture zones placed on the model boundary. In these fractures, the depth dependence of the permeability also is clearly visible.

Figure 4-4 presents a site-scale view of the model showing the stochastic permeability field ($K_{zz}$) for realisation 1. The surrounding coarse regional-scale model has been removed. Compared to the regional model, it is clear that the variance is larger in the site-scale model. The range for the stochastic permeability field is more than eight orders of magnitude, from $1.8 \cdot 10^{-4}$ m/s to $9.1 \cdot 10^{-13}$ m/s.

| Zone | $-\log_{10} K$ *[m/s]* | Width *[m]* | Inclination |
|---|---|---|---|
| 1 | 4.68 | 35 | 75 SE |
| 2 | 3.76 | 86 | 16 SW |
| 3 | 5.99 | 50 | 90 |
| 4 | 4.26 | 35 | 60 SW |
| 5 | 4.26 | 35 | - |
| 6 | 6.56 | 35 | - |
| 7 | 5.30 | 35 | - |
| 8 | 5.30 | 35 | 90 |
| 10 | 7.51 | 35 | - |
| 12 | 5.27 | 35 | 90 |
| 13 | 4.33 | 20 | 90 |
| 14 | 5.27 | 100 | 90 |
| Giboda | 4.26 | 100 | 90 |
| Giboda South | 4.26 | 50 | 90 |
| Imundbo | 4.26 | 100 | 90 |
| Skogsbo | 4.26 | 100 | 90 |
| Gräsbo | 5.27 | 100 | 90 |
| NS1 | 5.27 | 50 | 90 |
| NS2 | 4.91 | 25 | 90 |
| Örbyhus | 4.91 | 100 | 90 |
| Silbo | 4.91 | 100 | 90 |
| Dannemora | 4.91 | 100 | 90 |
| Källviken | 4.33 | 100 | 90 |

*Table 4-2* *Hydraulic conductivity, width and inclination for the fracture zones in the Beberg area as modelled within the present study.*

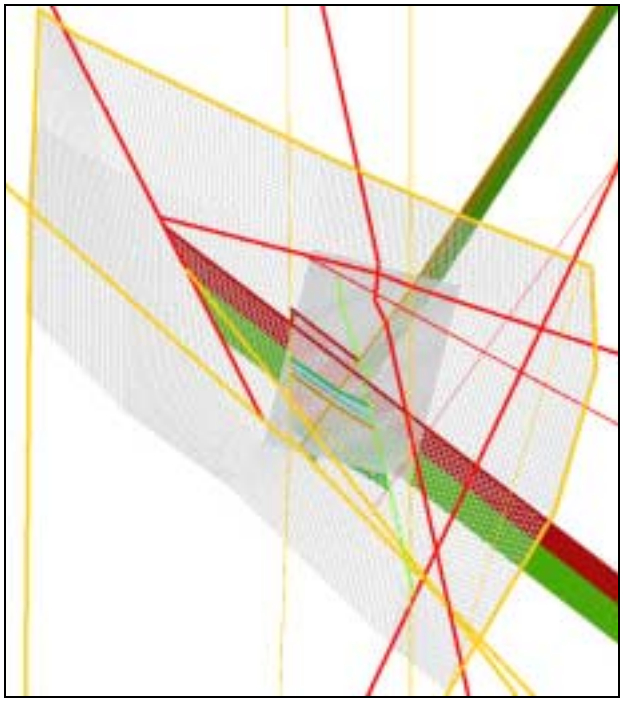

*Figure 4-1* *Horizontal regional view of the nested grid together with the fracture zones used in the model. The fractures are coloured with respect to permeability. The red colour indicates higher permeability and the blue colour indicates lower permeability. North is pointing up.*

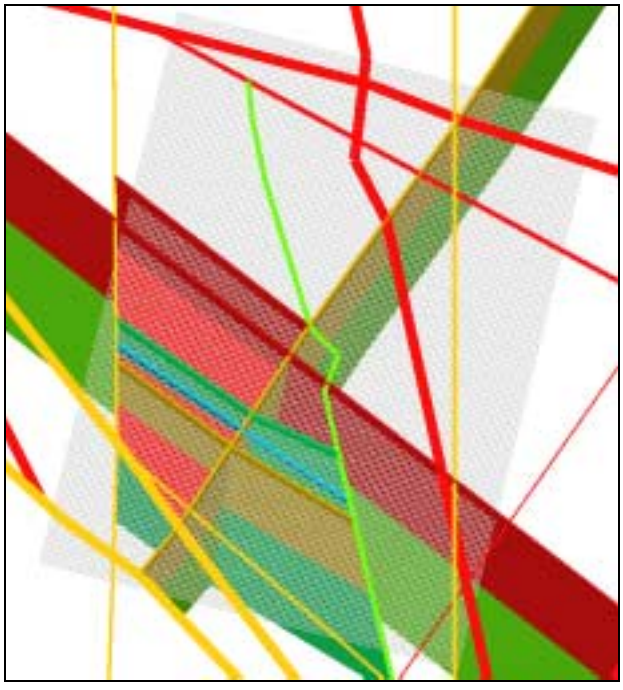

*Figure 4-2* *Horizontal view of the refined site-scale grid together with the fracture zones intersecting the site-scale model. The surrounding coarse regional-scale grid has been removed. The fractures are coloured with respect to permeability. The red colour indicates higher permeability and the blue colour indicates lower permeability. North is pointing up.*

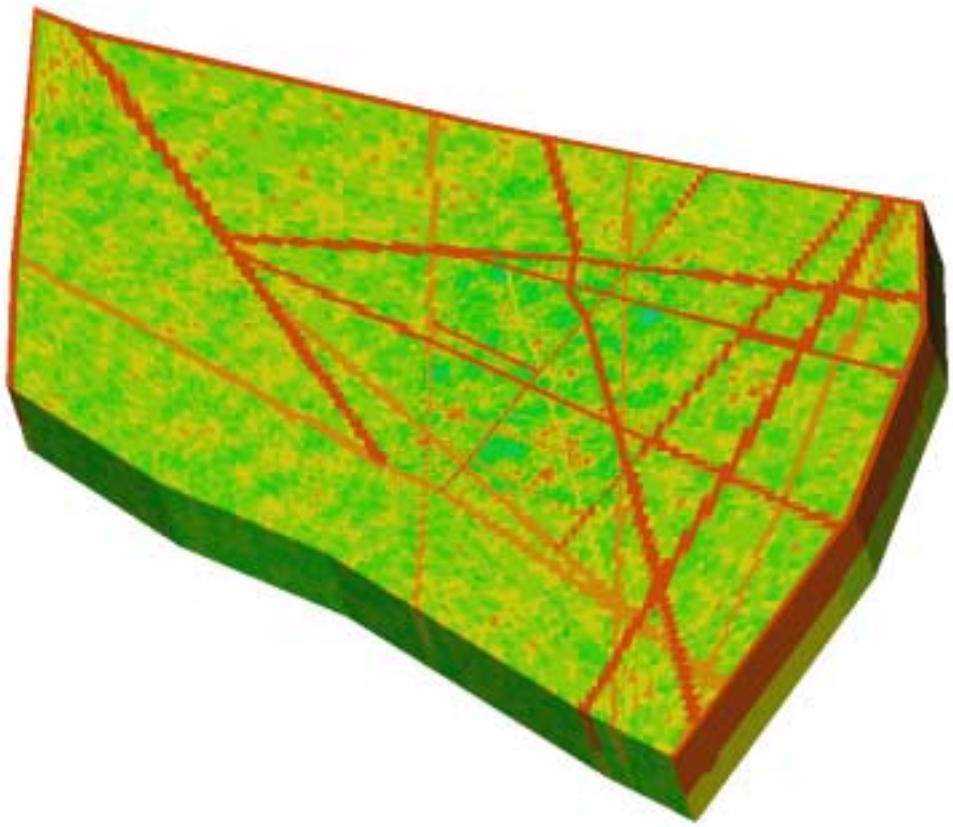

*Figure 4-3* *Regional view of the nested model showing the stochastic permeability field ($K_{zz}$) for realisation 1. The fracture zones are implicitly represented in the model. The red colour indicates higher permeability and the green/blue colour indicates lower permeability.*

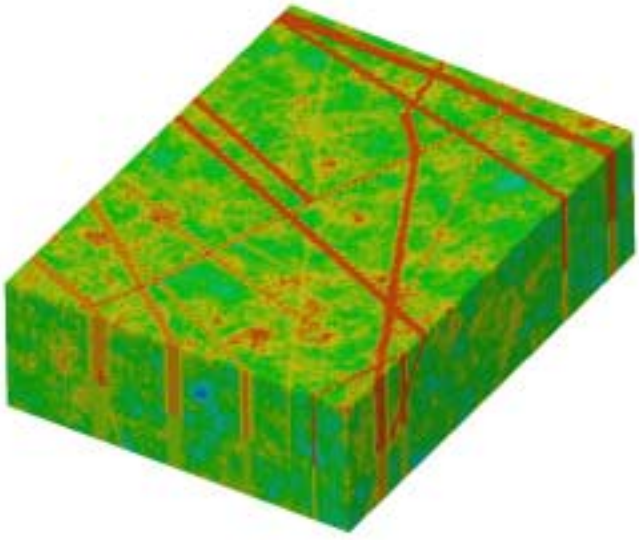

*Figure 4-4* *Site-scale view of the model showing the stochastic permeability field ($K_{zz}$) for realisation 1. The fracture zones are implicitly represented in the model. The surrounding coarse regional-scale model has been removed. The red colour indicates higher permeability and the green/blue colour indicates lower permeability.*

## 4.3 Boundary Conditions

In SR 97, the regional large scale hydrogeological modelling of Beberg was performed with NAMMU. The regional model was later used to provide appropriate boundary conditions for the site-scale modelling carried out with the HYDRASTAR stochastic continuum program. HYDRASTAR solves for steady-state constant density groundwater flow equations for a stochastic permeability distribution and needs to be provided with boundary conditions for pressure, which describe a hydraulic gradient consistent with the regional-scale model.

In the regional-scale modelling of Beberg in SR 97 it was concluded that the presence of saline groundwater has a great impact on the groundwater flow pattern in the region (Hartley et al., 1998). However, because of the limitations in HYDRASTAR, different strategies had to be applied in order to provide appropriate boundary conditions for the site-scale model.

A freshwater simulation (*grlfresh62a.gfs*) of the regional-scale model was used when generating the Dirichlet boundary conditions for the Base Case of the site-scale model. Other variants of the site-scale model were set up in order to assess the impact of saline groundwater by e.g. importing the environmental head boundary condition from the regional variable-density flow simulation.

The results in this study will only be compared to the Base Case of the SR 97 site-scale modelling carried out with HYDRASTAR. Thus, for the present study, a steady-state uniform density (freshwater) model is used.

The hydrogeological model in the present study uses a constant pressure boundary condition on the top surface equal to the topography obtained from the SKB GIS database, see Figure 4-5. This is the same data as was used for the regional-scale model of Beberg in SR 97. The topography data has a resolution of 50 m so the data was interpolated to the finite-element mesh. Since the discretisation of the present model is much more refined than the regional model in SR 97 it will capture topographical features in more detail and thus have a slightly different top boundary condition compared to the SR 97 models (both regional and site-scale).

On the sides and at the bottom of the model, a no-flow boundary condition was used. This differs from the model in SR 97 where hydrostatic boundary conditions were used on the sides of the model. The north, east and west boundaries are formed by the regional fracture zones (Silbo, Örbyhus and Dannemora respectively). Örbyhus and Dannemora are likely to be flow divides whereas Silbo probably is not. The use of a hydrostatic boundary condition in the SR 97 regional model was very important in that study since long-term transient saline flow was being considered. When considering saline flows the most realistic boundary condition is to allow the dense saline waters to be advected in or out through the sides of model rather than having no-flow conditions that force the salt to leave the model only through discharge at the surface. For freshwater calculations, as described here, this is not an issue and for a large steady-state regional model the vertical boundaries should have little effect on flow in the centre.

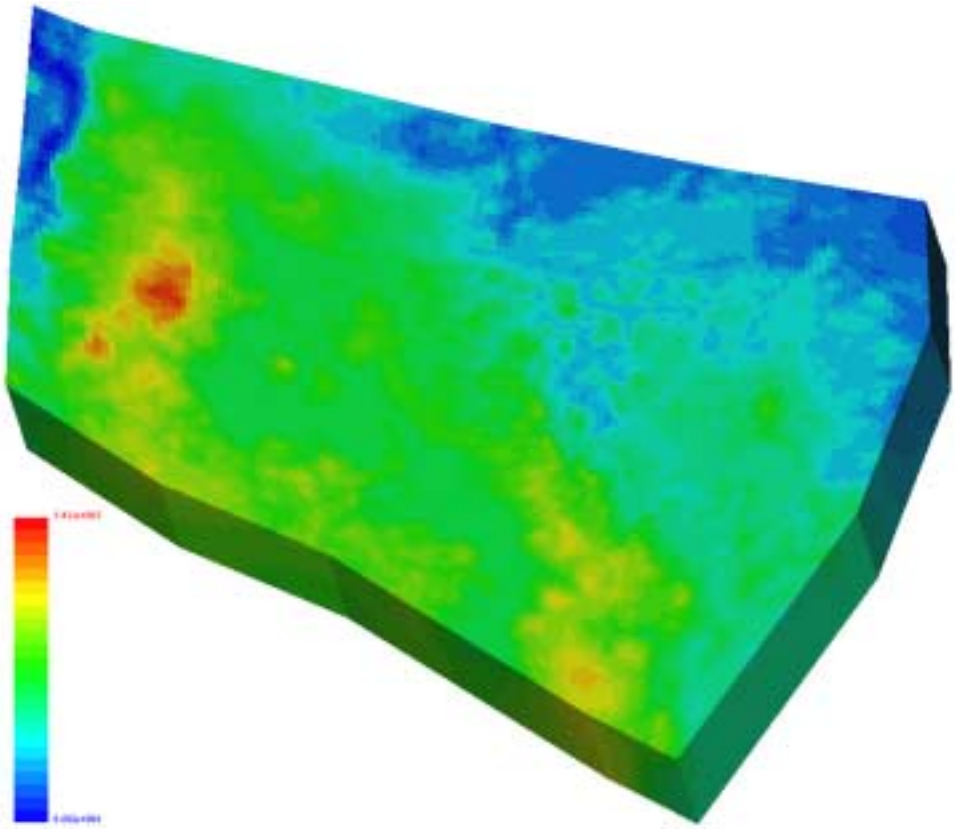

*Figure 4-5* *Regional view of the nested model showing the topographic boundary condition (Dirichlet) at the top of the model. Pressure given in [Pa].*

## 4.4 Pathlines

A set of 120 particles was released from the northern and the southern repository blocks for each of the 100 realisations. This is the same number of particles as was released in the HYDRASTAR model in SR 97 and exactly the same starting positions were used. The particles were released at a depth of 604.5 m (z = -604.5 m) which corresponds to the centre of the copper canisters used for the encapsulation of spent nuclear fuel. The repository is placed at a depth of 600 m (z = -600 m).

The pathlines show the advective transport of a tracer moving at the pore velocity. The path, the total travel time (TT) and the canister flux (CF) were determined for each of the released particles. The travel time is the time used by the particles released in the model to be transported from the starting position to the top boundary of the model domain. The canister flux is the Darcy groundwater velocity calculated by NAMMU as the resultant of the three velocity components ($u_x$, $u_y$ and $u_z$) at each of the 120 particle starting positions.

A constant flowing porosity of $1.0 \cdot 10^{-4}$ was used for the entire model domain.

The representation of the structural model is slightly different since the discretisation method gives an effective fracture zone location that is only accurate to the mesh-size (35 m). No attempt was made here to reconcile any starting positions located within fractures. The result is that some of the released particles (nr 12, 15, 18, 20 and 24) effectively start within Zone 8, see Figure 4-6. Since Zone 8 is connected to Zone 2 at this depth, these particles will have a fast connection to the top surface of the model, and hence a large canister flux and short travel time. There are other particles starting on the fringe of Zones 5 and 7. This will cause the results to be slightly skewed when evaluating the performance measures for the released particles.

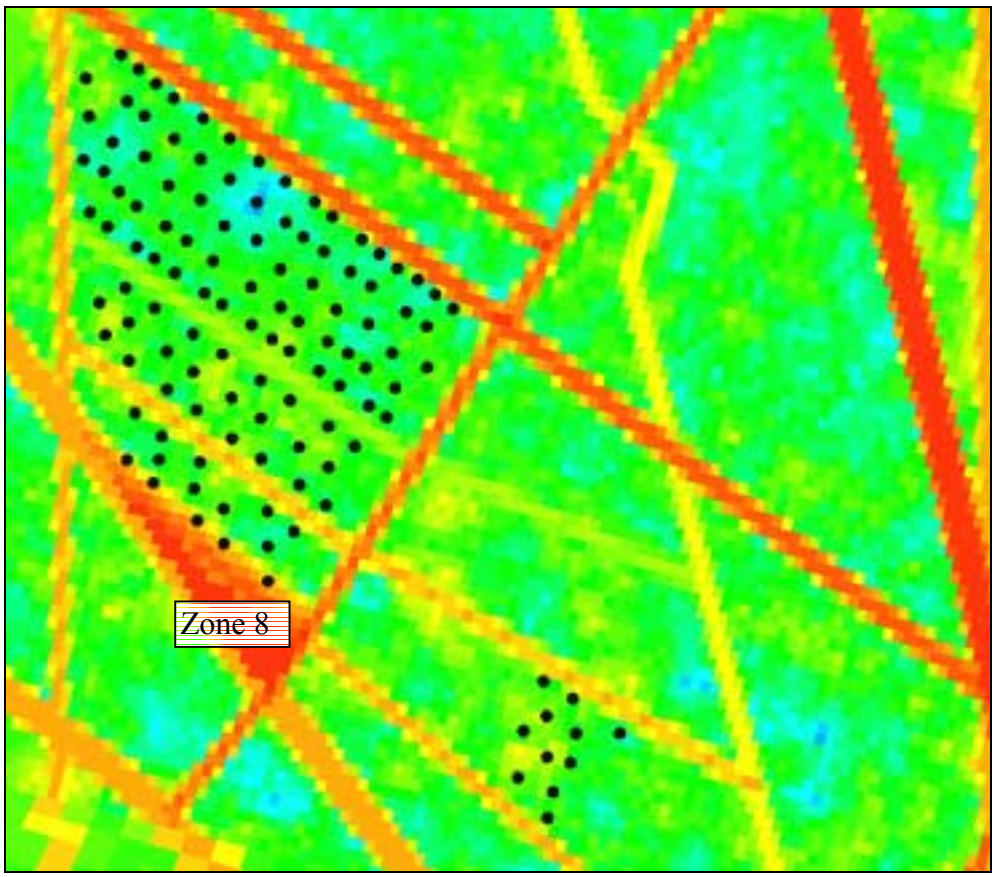


*Figure 4-6* *Starting locations (black dots) for the released particles superimposed on a horizontal slice coloured according to the logarithm of permeability at a depth of -604.5 masl for realisation 1. Five of the particles (nr 12, 15, 18, 20 and 24) are in effect started within Zone 8.*

# 5 Beberg results and comparison to SR 97

This section presents the results for the stochastic Monte Carlo simulation of the nested Beberg model and compares them with SR 97.

## 5.1 Nesting and Boundary Flow

The boundary flow for five realisations has been calculated on either side of the interface between the nested models to check the mass balance between the two scales, the mass balance within the site-scale, and for comparison with SR 97. The flux was calculated by integrating the velocity on a regular array of points on each surface with a spacing of 7m. It should be pointed out that this method of integration is approximate for the finite-element method since the method is not necessarily mass conservative over single elements but only for the entire model domain. The points used to calculate the flow are all aligned with the element boundaries apart from the top where they are placed at 0 m. The results are presented in Table 5-1.

The directions of flow agree with the HYDRASTAR model in SR 97. The flow through the top surface is only slightly larger in the NAMMU model. The flows on the vertical sides are about three times higher than in SR 97. In SR 97, the site-scale boundary flux was controlled by the boundary conditions that were supplied by a coarsely refined NAMMU regional-model. The SR 97 regional-model did not include explicitly all the site-scale fracture zones, and hence may have underpredicted the flow entering the site-scale. Further, the coarse refinement of the SR 97 regional model may have failed to capture some of the smaller scale flow patterns, again resulting in a lower site-scale flow. Hence, the much finer regional-scale mesh used here and the better match of fracture zone geometries between the regional- and the site-scale models (thanks to the nesting technique used) ensures greater connectivity across the interface, and leads to a larger mass flux between the two scales. Due to the no flow boundary condition being used at the bottom surface, flow there is virtually equal to zero. The flow match between the site- and regional-scale is good (due to the nesting method used and higher grid resolution) compared to SR 97 and the balance is relatively small. It should be noted that the values of flux given are only approximations of the flux across the site/regional-scale interface calculated by integrating the values of normal velocity at a regular array of points. The actual match of flux across the boundary if calculated by Gaussian quadrature would be expected to be more accurate, and improve as the tolerance on the iterative solver is reduced.

| Model Surface | External Site-scale | Internal Regional-scale | HYDRASTAR SR 97 |
|---|---|---|---|
| Top | 12.952 (out) | N/A | 10.130 (out) |
| Bottom | 0.040 (out) | N/A | 4.967 (in) |
| South | 8.013 (in) | 8.775 (in) | 3.600 (in) |
| West | 25.904 (in) | 25.838 (in) | 8.602 (in) |
| North | 14.280 (out) | 11.838 (out) | 4.154 (out) |
| East | 7.777 (out) | 7.381(out) | 2.870 (out) |
| ***Balance*** | ***1.133 (out)*** | ***2.402 (in)*** | ***0.016 (in)*** |

*Table 5-1* *Net groundwater flux through the interface between the site-scale and the regional-scale models [$m^3/s \times 10^{-3}$].*

Generally, it has been shown that by ensuring continuity of equations and fracture representation we ensure against flow being restricted by an approximate manual nesting, but the broad pattern of flow and mass exchange with the surface seems consistent. The higher flows in the NAMMU model show that getting the nesting wrong may give non-conservative (in the cautious sense of the word) predictions.

Figure 5-1 presents the residual pressure on each face of the refined site-scale model, i.e. the constraint boundary. The top surface is showing the topographic boundary condition while the sides and the bottom of the model show the calculated residual pressure.

## 5.2 Monte Carlo Stability

In SR 97, the Monte Carlo technique was used to perform the site-scale hydrogeological simulations. It was shown that the median travel time and median canister flux were approximately stable after 35 realisations and that a total number of 100 realisations was adequate for estimating the medians of the performance measures. In this study the same number of realisations as in SR 97 (i.e. 100 realisations) were performed in the Monte-Carlo simulation. The results are shown in Figure 5-2 and Figure 5-3 where the medians of the logarithm of travel time and the logarithm of canister flux with respect to the number of realisations are presented. The figures show that the medians stabilise within approximately 35 realisations, which is in agreement with the results from SR 97.

As explained by (Gylling et al., 1999) the stability of the sample median does not imply that, for instance, the sample variance is also stable since these higher moments usually require more realisations to stabilise.

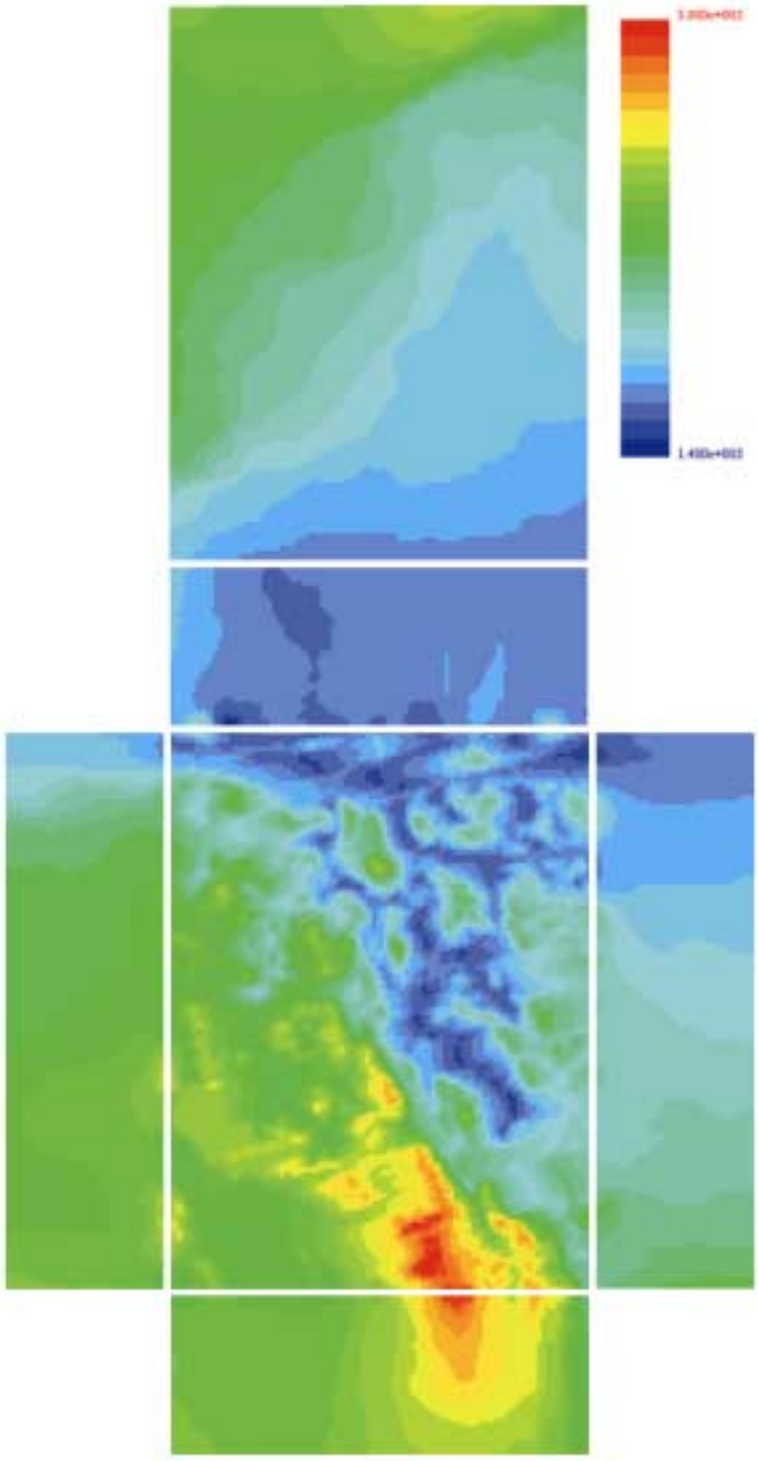

*Figure 5-1* *The residual pressure on each face of the refined site-scale model. The surrounding coarse regional-scale model has been removed. The top surface is showing the topographic boundary condition (Dirichlet) while the sides and the bottom of the model show the calculated residual pressure. The red colour indicates higher pressure and the blue colour indicates lower pressure. The pressure values (Pa) are given in the legend.*

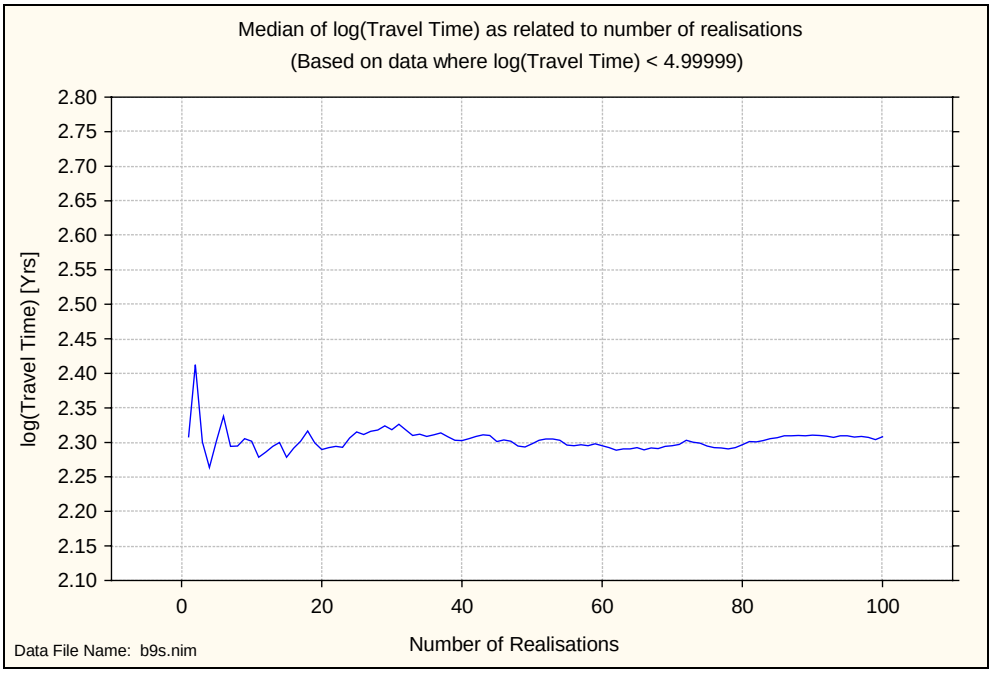


*Figure 5-2* *Monte Carlo stability for 100 realisations. Median travel time versus number of realisations. Results for 120 starting positions.*

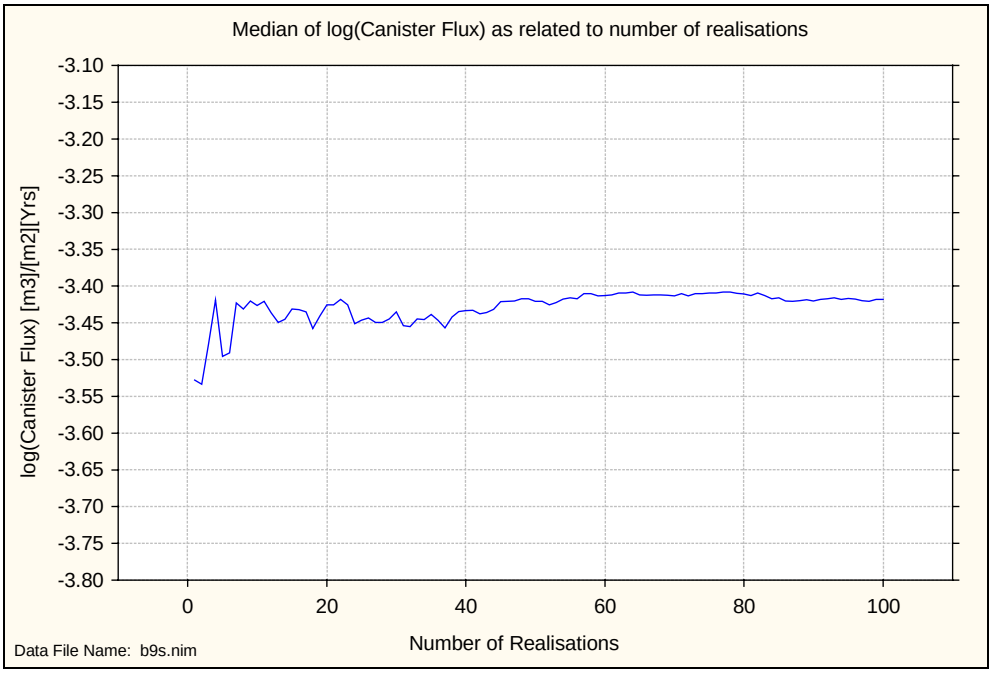


*Figure 5-3* *Monte Carlo stability for 100 realisations. Median canister flux versus number of realisations. Results for 120 starting positions.*

## 5.3 Statistical Summary

Table 5-2 shows the statistical summary for 100 realisations of the 120 starting positions. The calculated performance measures are the travel time (TT), the canister flux (CF), the F-ratio (F), the travel length (TL) and the average velocity (AV) along each pathline. The travel time is the time used by the particles released in the model to be transported by advection from the starting position to the top boundary of the model domain. The canister flux is the Darcy groundwater velocity calculated by NAMMU as the resultant of the three velocity components ($u_x$, $u_y$ and $u_z$) at each of the 120 particle starting positions. The F-ratio is defined as $F = a_r \cdot TT/\varepsilon_f$, where $a_r$ is the flow wetted surface *[$m^2/m^3$]* and $\varepsilon_f$ the flow porosity *[non-dimensional]*. The average velocity is calculated as (TL/TT). All particles are released at a depth of -604.5 m. Some particles (0.3 %) failed to exit the model domain due to numerical problems. The statistics has not been adjusted by removing these particles since they constitute only a small part of the total population and thus should not affect the result significantly.

| **Statistics** | **$Log_{10}$(TT** *[yrs]***)** | **$Log_{10}$(CF** *[m/yr]***)** | **$Log_{10}$(F** *[yrs/m]***)** | **$Log_{10}$(TL** *[m]***)** | **$Log_{10}$(AV** *[m/yr]***)** |
|---|---|---|---|---|---|
| Mean | 2.192 | -3.344 | 6.192 | 3.515 | 1.327 |
| Median | 2.308 | -3.418 | 6.308 | 3.524 | 1.218 |
| Variance | 0.691 | 1.108 | 0.691 | 0.018 | 0.571 |
| 5th Percentile | 0.760 | -4.877 | 4.760 | 3.297 | 0.331 |
| 25th Percentile | 1.790 | -4.014 | 5.790 | 3.433 | 0.847 |
| 75th Percentile | 2.727 | -2.829 | 6.727 | 3.589 | 1.686 |
| 95th Percentile | 3.317 | -0.935 | 7.317 | 3.710 | 2.629 |
| Fraction | 0.997 | - | - | - | - |

*Table 5-2* *Statistical summary for 100 realisations of 120 starting positions with a flow porosity of $\varepsilon_f = 1 \cdot 10^{-4}$ and a flow-wetted surface of, $a_r = 1.0\ m^2/(m^3\ rock)$.*

## 5.4 Travel Time and F-ratio

Table 5-2 summarises the result for the travel time and the F-ratio. The median of the travel time is 203 years, with an interquartile range from 62 years to 533 years. The corresponding results from the Beberg site-scale simulation (Base Case) are as follows: the median of the travel time is 56 years, with an interquartile range from 29 years to 104 years. The median travel time is a factor 3.6 longer here compared to SR 97. This suggests that the mean hydraulic conductivity along paths differs by approximately a factor 3.6 between the models. There are three main causes of the discrepancy. The main one being the structural model around the repository. These areas are called the Northern and the Southern Rock Blocks, and in the SR 97 HYDRASTAR model they were given a higher conductivity. In the NAMMU model these rock blocks are not represented, and thus have the same conductivity as the surrounding rock. Compared to

the HYDRASTAR model the area corresponding to the Northern Rock Block has a conductivity value that is a factor 5.5 lower. The area corresponding to the Southern Rock Block has a conductivity value that is a factor 2.4 lower. Hence, the travel time is increased in the NAMMU model. The second cause has the opposite effect, and that is that five of the stream tube starting positions are located in NAMMU's representation of Zone 8. The travel times associated with these positions will be exceptionally short and account for the spurious tail seen in the histogram shown in Figure 5-4. There is a similar effect on the canister flux at these positions. The final cause is the representation of the fracture zones as deterministic in the NAMMU model as opposed to trends in a stochastic field in HYDRASTAR. Given these reasons the differences, as presented in Table 5-3, are understandable.

Since the five particles that are started within Zone 8 skew the results, the statistics (median and variance for the travel time and the canister flux) were also calculated with the data for these starting positions removed from the total population. There may still be a few particles starting within elements of higher permeability associated with the representation of zones 5 and 7. The adjusted values are presented together with the values for the total population and the results from SR 97 in Table 5-3. The values given within brackets are the travel times in years. The median travel time and the median canister flux are not affected much by this adjustment. The travel time is, as expected, slightly increased while the canister flux is slightly deceased. The variance however changes significantly. The adjusted $\log_{10}$ standard deviation in canister flux is 0.891, a factor 1.37 larger compared to SR 97. However, the value is very close to the standard deviation in hydraulic conductivity ($\log_{10}(K)$) which is 0.831, and hence reasonable. It is difficult to predict an 'expected' standard deviation in canister flux as the practical range of $\log_{10}(K)$ is bigger than the distance from each start point to the nearest site-scale fracture zone. For extra guidance, the statistics of the permeability in the rock-mass were calculated at the canister start locations for one realisation and compared with specified input permeability in the local-scale model at this depth. For this realisation the fractures were excluded to avoid them distorting the statistics. The comparison is presented in Table 5-4. The generated mean permeability is correct and the variance is slightly less than that input value. This is reasonable since the canister location separation is much smaller than the practical range and so each data point is not an independent realisation. Interestingly, it suggests that the fracture zones significantly increase canister flux variability in the NAMMU model, but have little effect on variability in the HYDRASTAR model. The most likely explanation is that some canister locations coincide with local-scale zones in the NAMMU model whereas it was carefully avoided in the HYDRASTAR model.

Given the differences in the representation of the two rock blocks, calculated boundary flux, and to a lesser degree the structural model (for example, Zone 2) the pathline statistics are broadly consistent.

| | NAMMU total | | NAMMU adjusted | | SR 97 | |
|---|---|---|---|---|---|---|
| **Statistics** | **$Log_{10}$(TT*[yrs]*)** | **$Log_{10}$(CF*[m/yr]*)** | **$Log_{10}$(TT*[yrs]*)** | **$Log_{10}$(CF*[m/yr]*)** | **$Log_{10}$(TT*[yrs]*)** | **$Log_{10}$(CF*[m/yr]*)** |
| Median | 2.308 (203) | -3.418 | 2.345 (221) | -3.463 | 1.755 (56) | -2.923 |
| Variance | 0.691 | 1.108 | 0.450 | 0.794 | 0.237 | 0.423 |
| Standard deviation | 0.831 | 1.0526 | 0.671 | 0.891 | 0.487 | 0.650 |

*Table 5-3* *Comparison of the travel time and canister flux statistics for the current study and SR 97. Travel times in years given within brackets.*

| | Local-scale input at 604.5m bsl | Pathline start locations |
|---|---|---|
| **Statistics** | **$Log_{10}$(K)** | **$Log_{10}$(K)** |
| Median | -15.25 | -15.26 |
| Variance | 0.69 | 0.56 |

*Table 5-4* *Comparison of rock mass permeability statistics for the input data in the local-scale region at repository depth and in the model at the canister start locations.*

Figure 5-4 presents the relative frequency histogram of $\log_{10}$ travel time for 100 realisations of 120 starting positions. The histogram is normalised with respect to the total number of starting positions. Noticeable is a group of particles with very short travel times (0.1-1 years); these correspond to the five starting positions in Zone 8. The histogram is also a bit wider than it was in SR 97.

Figure 5-5 presents a box plot of the $\log_{10}$ travel time. The variability between the different realisations is large. Some realisations result in short travel times, which explains the group of particles in the lower region of Figure 5-4. Another feature of the box plot is the large range, more than one order of magnitude, between the $5^{th}$ and the $25^{th}$ percentile.

Figure 5-6 presents the relative frequency histogram of $\log_{10}$ F-ratio for 100 realisations of 120 starting positions. The histogram is normalised with respect to the total number of starting positions and is essentially a linear transformation of the travel time in Figure 5-4.

Figure 5-7 presents a scatter plot of $\log_{10}$ travel time versus $\log_{10}$ canister flux. The expected inverse correlation between the travel time and the canister flux is clear. The vertical lines at the right of the figure also correspond to the starting locations in Zone 8.

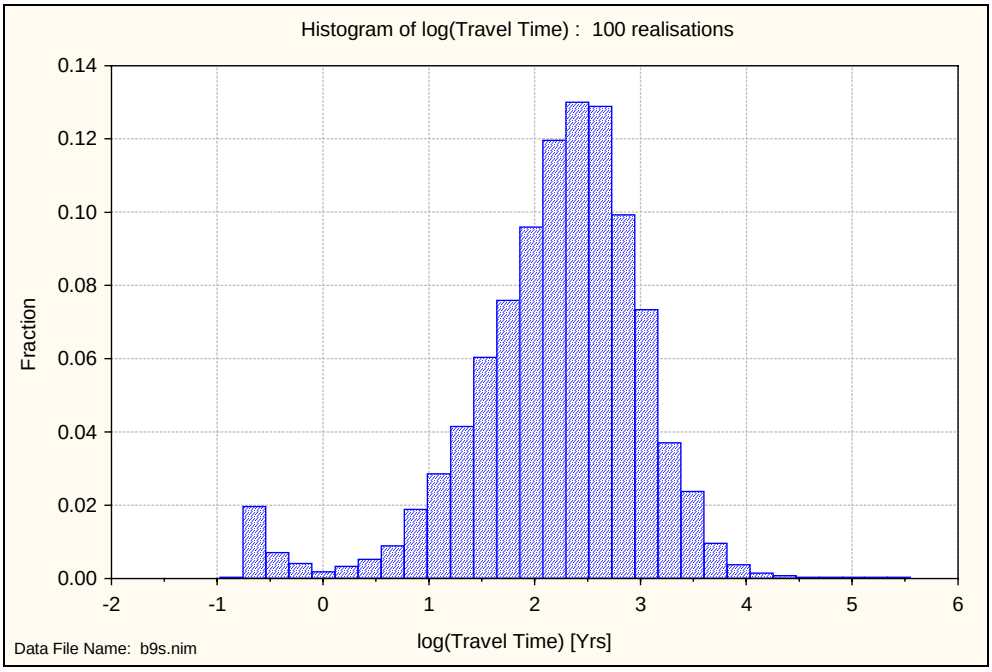


*Figure 5-4* *Relative frequency histogram of $\log_{10}$ travel time. The histogram is normalised with respect to the total number of starting positions. Results for 100 realisations of 120 starting positions and a flow porosity of $\varepsilon_f = 1 \cdot 10^{-4}$.*

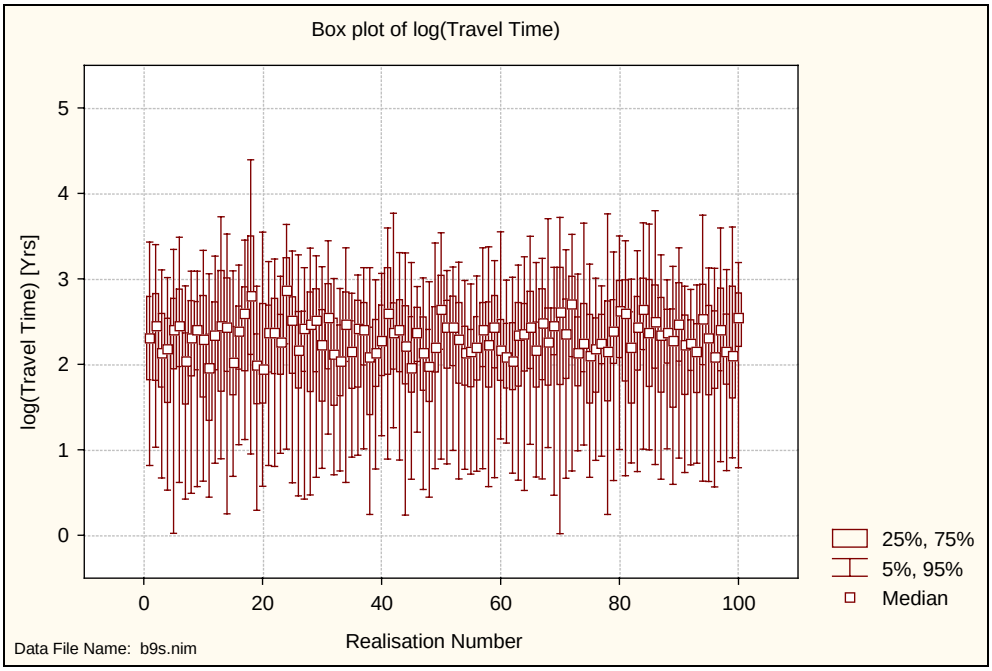


*Figure 5-5* *Box plot of $\log_{10}$ travel time versus realisation number showing the median and the $5^{th}$, $25^{th}$, $75^{th}$, and $95^{th}$ percentiles. Results for 100 realisations of 120 starting positions and a flow porosity of $\varepsilon_f = 1 \cdot 10^{-4}$.*

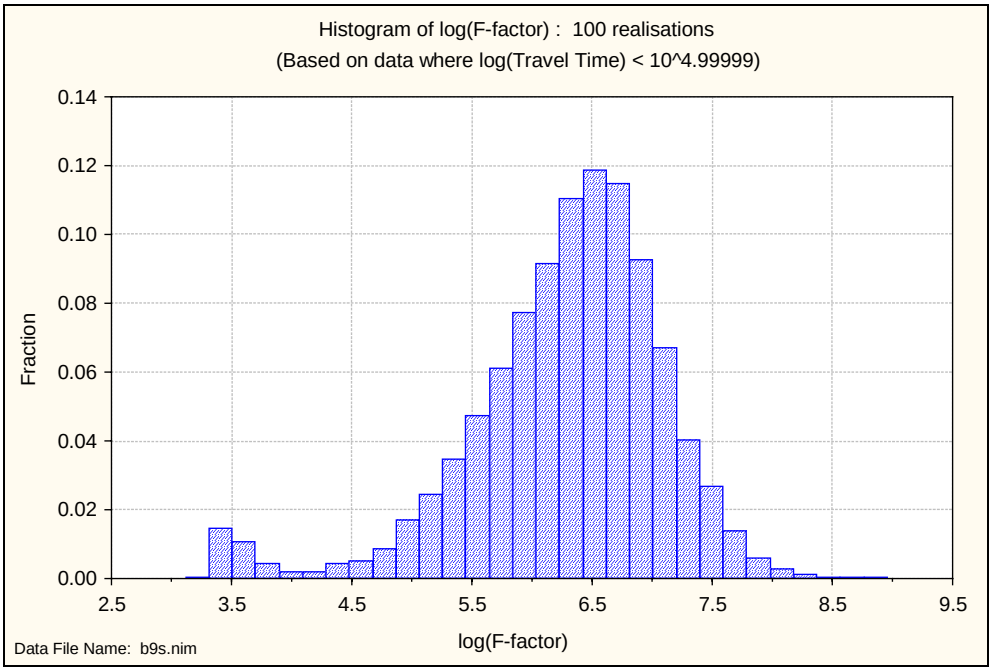


*Figure 5-6* *Relative frequency histogram of $\log_{10}$ F-ratio. The histogram is normalised with respect to the total number of starting positions. Results for 100 realisations of 120 starting positions and a flow porosity of $\varepsilon_f = 1 \cdot 10^{-4}$ and a flow wetted surface of $a_r = 1.0\ m^2/(m^3\ rock)$.*

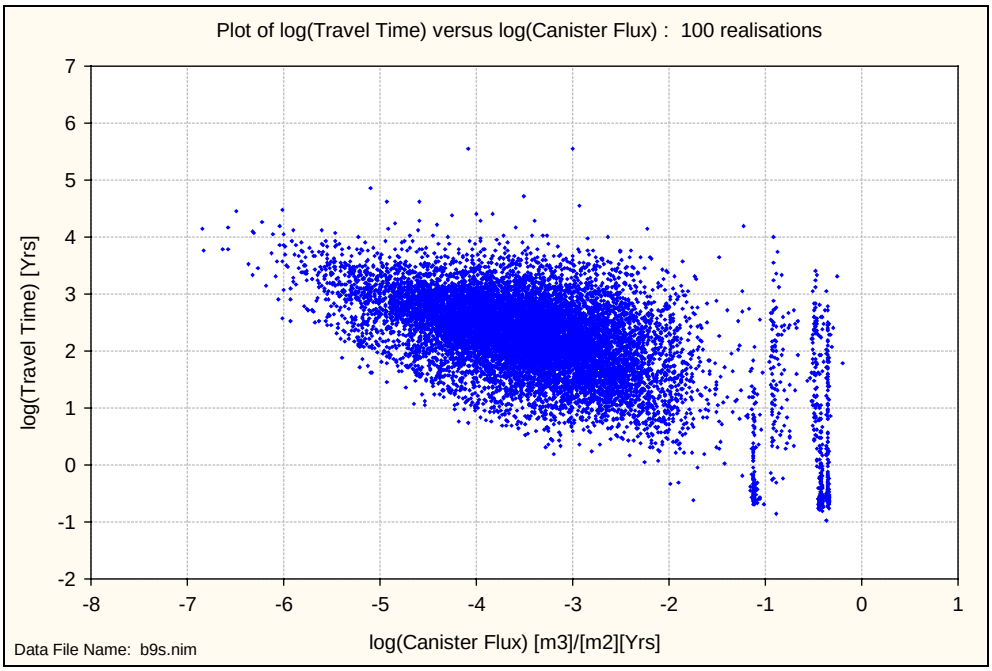


*Figure 5-7* *Scatter plot of $\log_{10}$ travel time versus $\log_{10}$ canister flux. Results for 100 realisations of 120 starting positions and a flow porosity of $\varepsilon_f = 1 \cdot 10^{-4}$.*

## 5.5 Canister Flux

Table 5-2 summarises the result for the canister flux and indicates a median canister flux of $3.8 \cdot 10^{-4}$ m/year, with an interquartile range from $9.7 \cdot 10^{-5}$ m/year to $1.5 \cdot 10^{-3}$ m/year. The variance of the $\log_{10}$(CF) is 1.108, or 0.794 when particles in Zone 8 are removed. The median canister flux for 100 realisations of 120 starting positions is a factor 3.1 lower compared to SR 97, see Table 5-3. This is in agreement with the discrepancies for the travel time and is explained by the reasons given in section 5.4.

Figure 5-8 presents the relative frequency histogram of $\log_{10}$ canister flux for 100 realisations of 120 starting positions. The histogram is normalised with respect to the total number of starting positions. The group of particles with very short travel times (0.1-1 years) that could be seen in Figure 5-4 here appears on the right side of the histogram with canister flux values between 0.05 m/year and 1 m/year. The histogram is also wider than it was in SR 97. This is also confirmed by the box plot of the canister flux in Figure 5-9 where a variability of more than five orders of magnitude is presented. Another feature is the large range, almost two orders of magnitude, between the 75th and the 95th percentile corresponding to the starting positions in Zone 8.

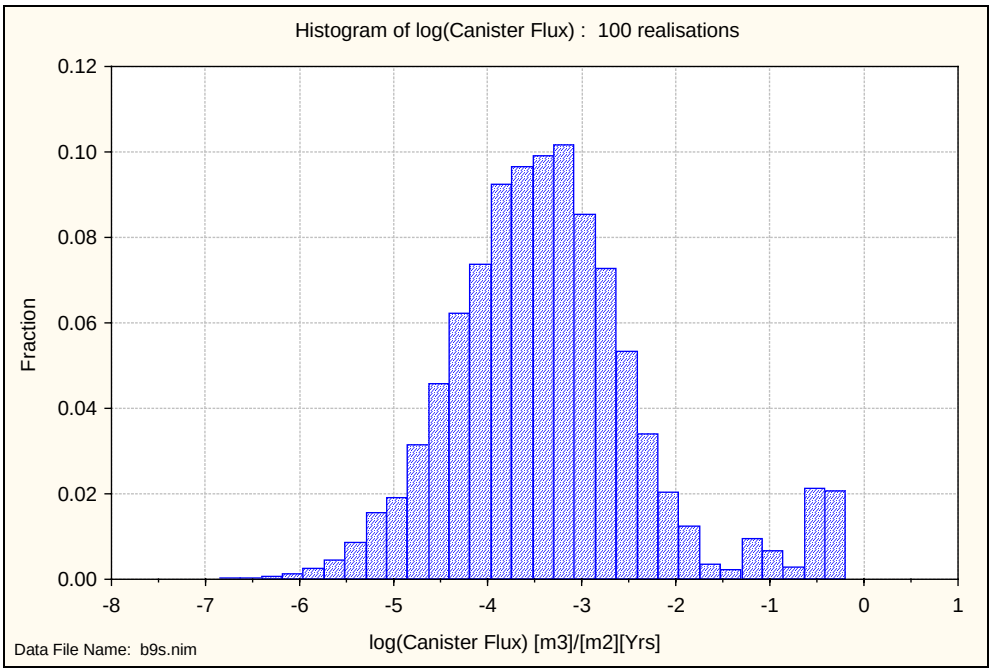


*Figure 5-8* *Relative frequency histogram of $\log_{10}$ canister flux. The histogram is normalised with respect to the total number of starting positions. Results for 100 realisations of 120 starting positions.*

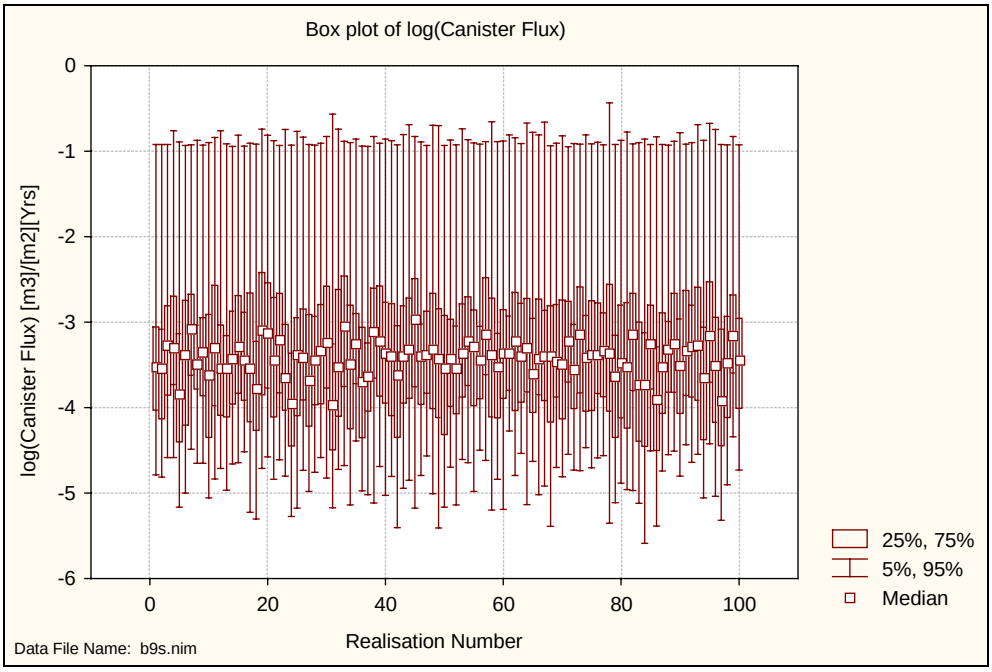


*Figure 5-9* *Box plot of $log_{10}$ canister flux versus realisation number showing the median and the $5^{th}$, $25^{th}$, $75^{th}$, and $95^{th}$ percentiles. Results for 100 realisations of 120 starting positions.*

## 5.6 Exit Locations

The coordinates for the travel paths (stream tubes) are calculated in NAMMU. The last coordinate for each pathline has been extracted for presentation of the exit locations of the released particles. The particles that did not reach the top surface of the model domain have been removed. Figure 5-10 presents a regional view of the model with exit locations (red markers) for 100 realisations of 120 starting positions. The repository tunnels are shown as short black lines at -604.5 masl projected up to the top surface within the nested site-scale model that has been coloured grey. All released particles exit within the site-scale model.

Figure 5-11 presents a close-up view of the model in Figure 5-10. The boundary is showing the more refined site-scale model that is nested inside the coarse regional-scale model.

The pathlines are predominantly directed to the northeast through the rock mass away from the repository. This corresponds to the regional flow pattern. The major part of the particles exit locations are grouped close together near Zone 5 and Zone 1. The particles released from the Northern Repository follow Zone 2 up to Zone 5 where they go either to the northwest or to the southeast following Zone 5 up to the top surface of the model. The particles released from the Southern Repository initially follow Zone 7 either to the northwest through Zone 2 to Zone 5 or to the southeast passing through Zone 3 up to Zone 5. Some particles either exit in Zone 1 or follow the zone up to the Imundbo Zone where they exit. In SR 97, the Imundbo Zone was a very important feature since it corresponded to a majority of the exit locations. Here, it is of less importance as more particles reach the surface just to the west of Imundbo. This is due to the much better

representation of the topography in the new regional-scale model that captures some local discharge regions of low topography in greater detail than in SR 97 (see Figure 5-13). These discharge points correspond to a number of small streams/springs in the area.

Figure 5-12 presents a plan view of 120 calculated 3D pathlines started at -604.5 masl for realisation 1. The pathlines are superimposed on a horizontal slice coloured according to the logarithm of permeability at three different elevations: 0 masl (top), -300 masl (middle) and -750 masl (bottom) respectively. Due to the inclination of some fracture zones, the appearance of the permeability field varies with the elevation of the drawing plane. The exit locations correspond to low elevation areas in the topography.

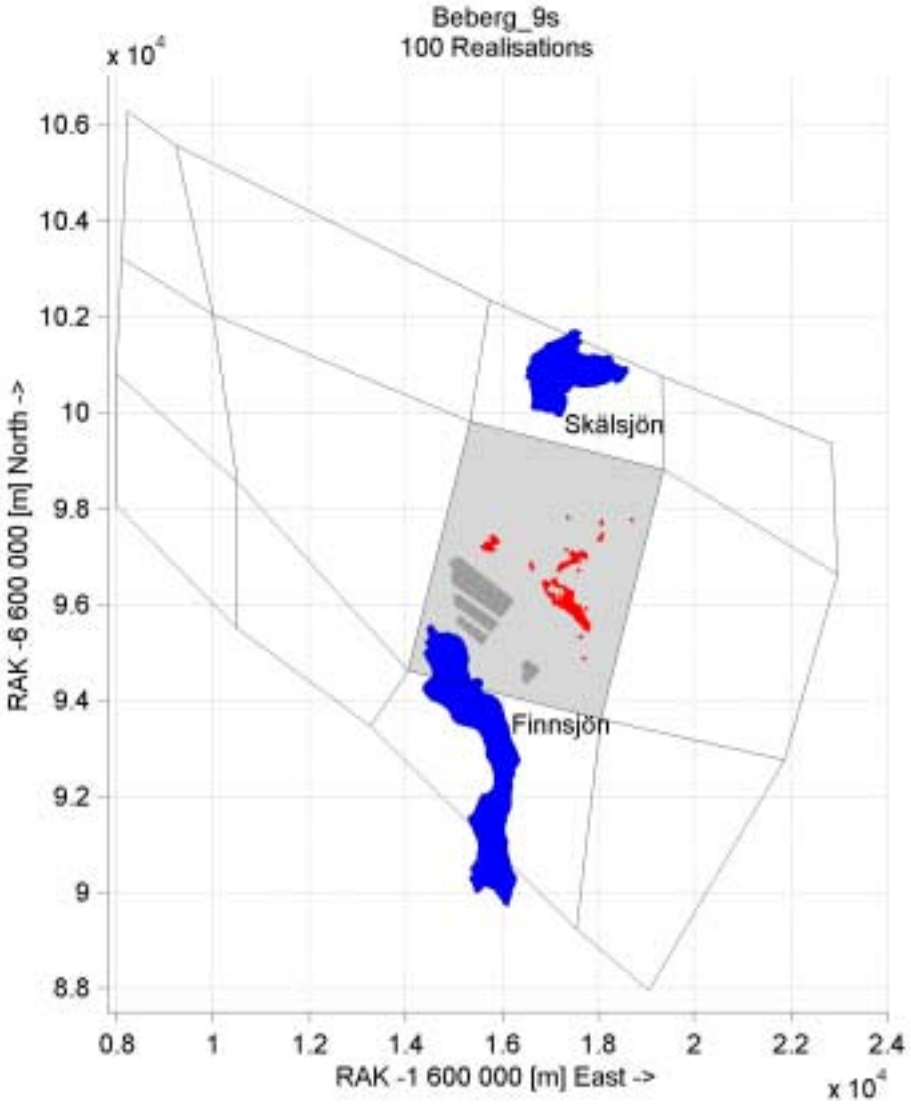


*Figure 5-10* *Regional view of the model with exit locations (red markers) for 100 realisations of 120 starting positions. Repository tunnels (black lines) at -604.5 masl in the nested site-scale model (grey) shown projected up to the model surface. The blue domains correspond to lakes with the names given.*

Figure 5-12 also shows one effect of the deterministic fractures where many particles follow Zone 5 in a direction perpendicular to the hydraulic gradient. When the fractures are implicitly represented in the model, the permeability of the fracture elements is made anisotropic in the length direction of the fracture. This will enhance the flow in the fracture plane and possibly lead the particles in a direction not exactly corresponding to the hydraulic gradient.

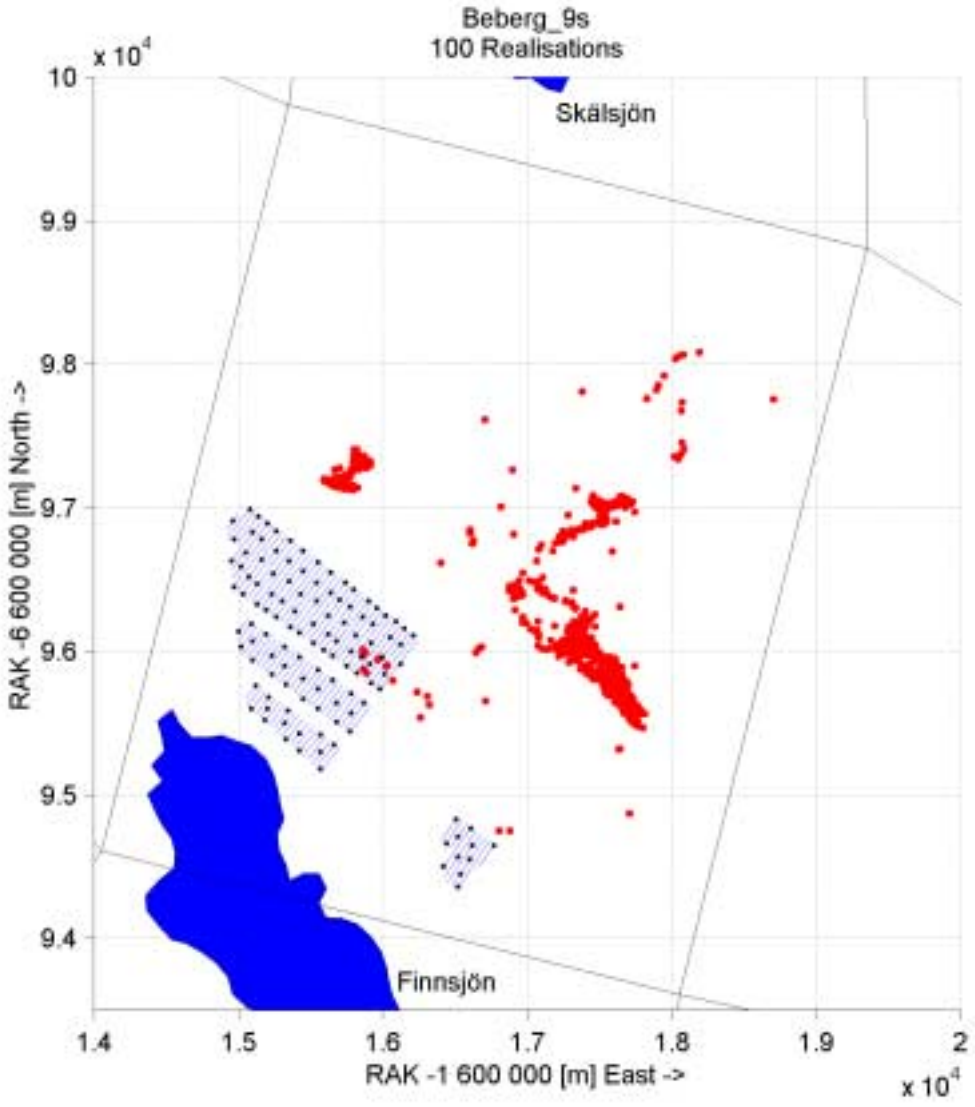


*Figure 5-11* *Close-up view of the model with exit locations (red markers) for 100 realisations of 120 starting positions (black markers). Repository tunnels (blue lines) at -604.5 masl shown projected up to the model surface. Boundary showing the more refined nested site-scale model.*

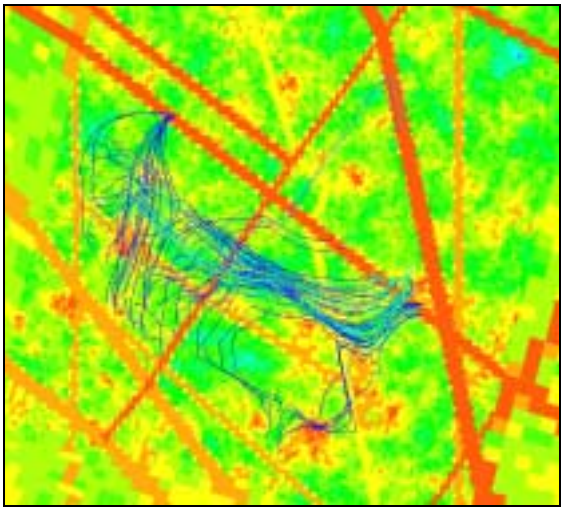

(a)

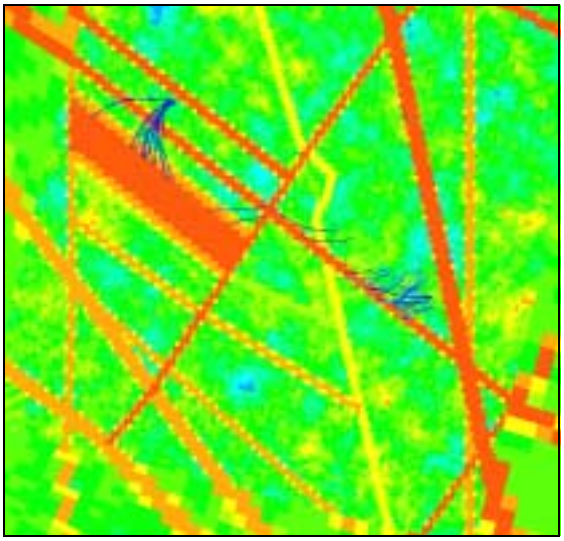

(b)

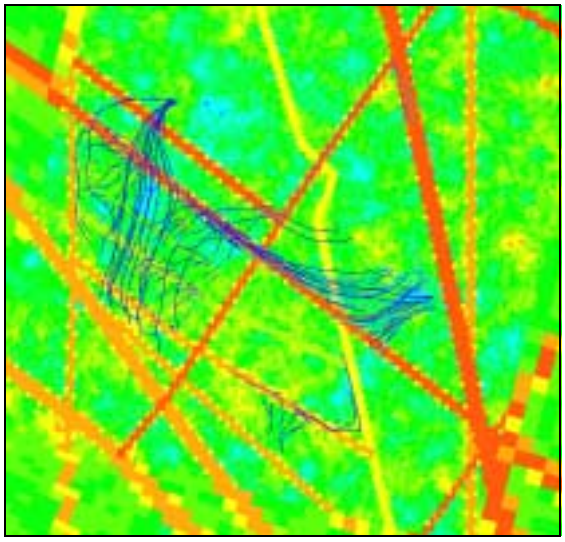

(c)

*Figure 5-12* *Plan view of calculated 3D pathlines for realisation 1. The pathlines are intercepted by horizontal slices coloured according to the logarithm of permeability at 0 masl (a), -300 masl (b) and -750 masl (c) respectively. Results for 120 pathlines started at -604.5 masl.*

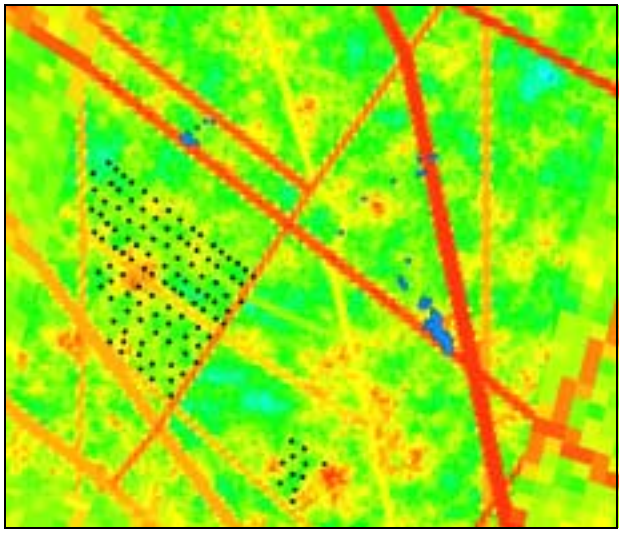

(a)

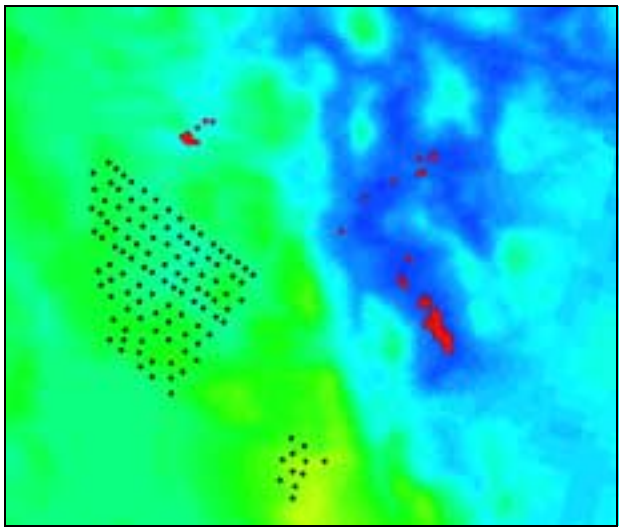

(b)

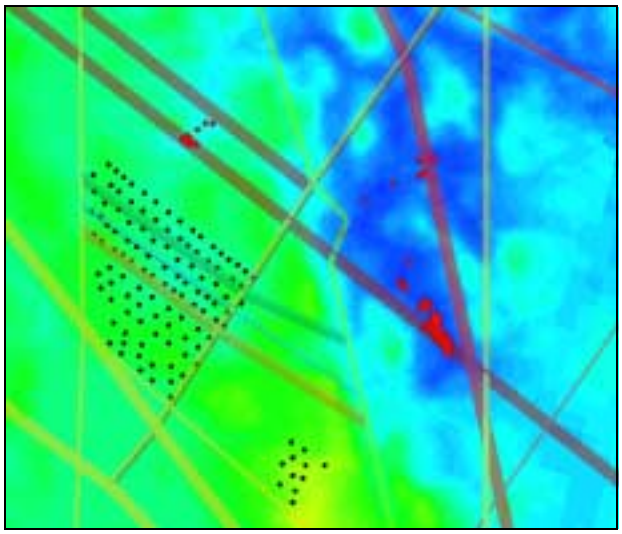

(c)

*Figure 5-13* *Plan view of exit locations ((a) blue markers, (b)(c) red markers) for realisation 1-3 superimposed on a horizontal slice at 0 masl coloured according to: (a) the logarithm of permeability; (b) the hydraulic head; (c) the hydraulic head with the explicit fracture zones. The starting locations are shown as black markers. Results for 120 pathlines started at -604.5 masl.*

## 5.7 Individual Realisations

The first three of the 100 realisations have been selected to show the variability between the realisations with more detail. Since the probability for each realisation in a Monte Carlo set is equal, there is no point in trying to select representative realisations of the ensemble with respect to travel time and canister flux. No attempt has been made to adjust the values for the particles started within Zone 8. Thus, the results here are based on the results for all released particles, and hence contain some bias toward fast paths.

Table 5-4, Figure 5-17 and Figure 5-18 present the statistical summary and the floating histograms of $\log_{10}$ travel time and $\log_{10}$ canister flux for three realisations of 120 starting positions. The histograms are normalised with respect to the number of starting positions in each realisation. The range of median travel times is 136 to 287 years and the range of median canister fluxes is from $2.91 \cdot 10^{-4}$ m/year to $5.42 \cdot 10^{-4}$ m/year. The range in median travel time and median canister flux is approximately two, which is the same result as was obtained in the HYDRASTAR model in SR 97.

The exit locations for the three realisations of 120 starting positions are presented in close-up views in Figure 5-14 - Figure 5-16. It is clear that the variability of the flowpaths between the realisations is small. This was also stated in the previous section studying the results of all 100 realisations. The exit locations are concentrated around Zone 5 with a few particles exiting in the Imundbo Zone.

Figure 5-19 and Figure 5-20 present scatter plots of the performance measures for the three selected realisations by starting position number, illustrating the variability within and between realisations. The variability of the performance measures varies considerably between different starting positions. This variability could be ascribed to the closeness of some of the starting positions to the fracture zones crossing the repository area. For example, the $\log_{10}$ travel time for starting position 24 shows a variability of more than 2.5 orders of magnitude which is roughly a factor two higher than for many of the other starting positions. This can be ascribed to five particle start positions being located in Zone 8. The same effects were seen in SR 97.

Figure 5-21 presents the number of released particles for each realisation that failed to exit the model. In 75 of the 100 realisations none of the released particles failed to exit the model. In only a few realisations more than two particles failed to exit the model.

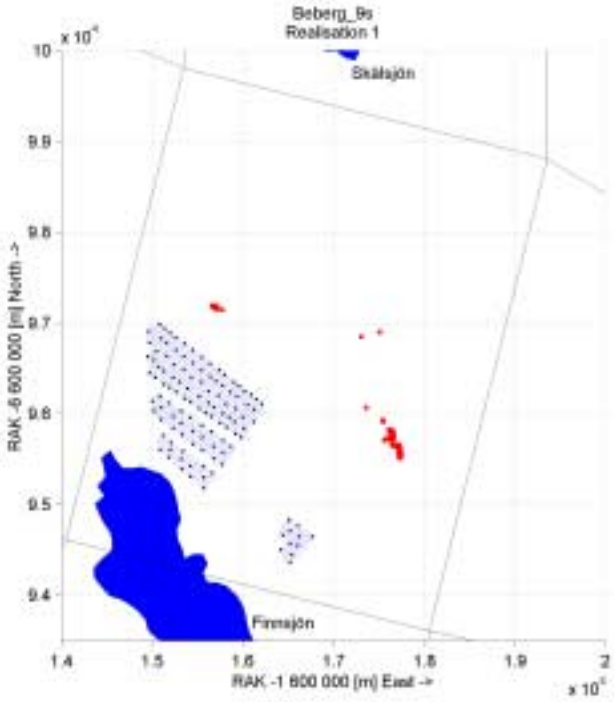


*Figure 5-14 Exit locations for realisation 1. Results for 120 starting positions.*

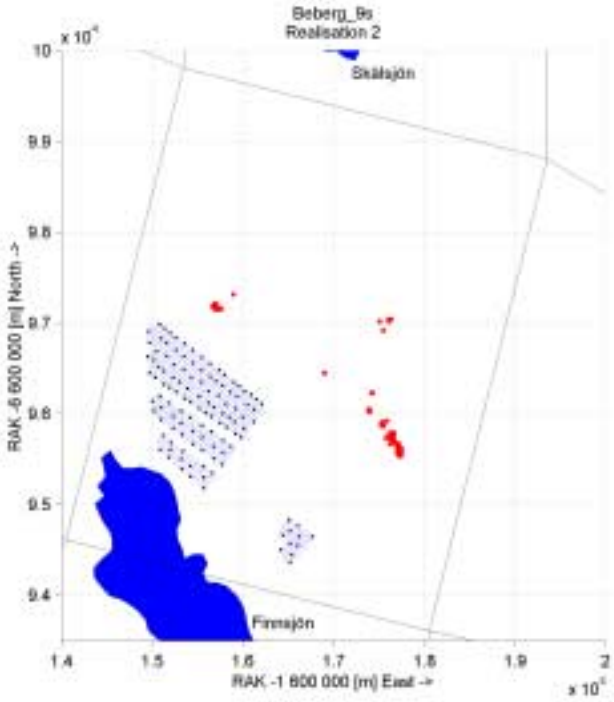


*Figure 5-15 Exit locations for realisation 2. Results for 120 starting positions.*

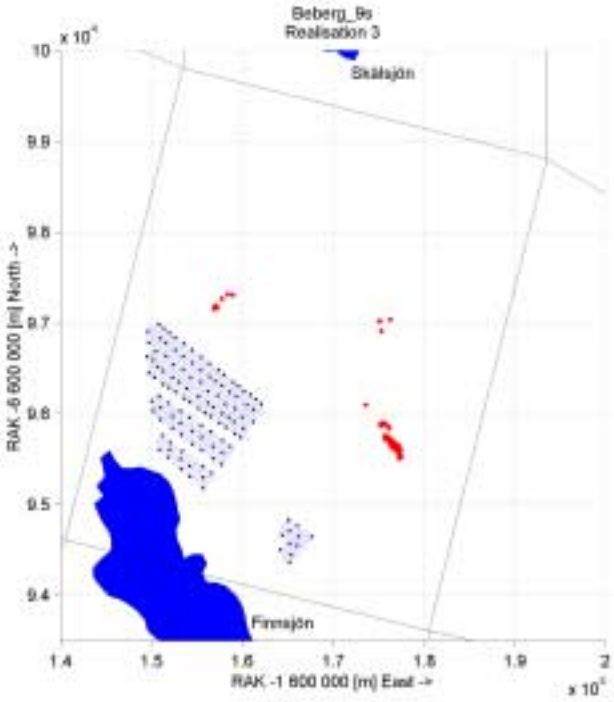


*Figure 5-16 Exit locations for realisation 3. Results for 120 starting positions.*

| | Realisation 1 | Realisation 2 | Realisation 3 |
|---|---|---|---|
| **$Log_{10}$(TT** *[yrs]***)** | | | |
| Mean | 2.226 | 2.284 | 2.067 |
| Median | 2.308 | 2.458 | 2.132 |
| Variance | 0.753 | 0.674 | 0.575 |
| 5th Percentile | 0.767 | 1.000 | 0.611 |
| 25th Percentile | 1.769 | 1.788 | 1.721 |
| 75th Percentile | 2.781 | 2.821 | 2.555 |
| 95th Percentile | 3.377 | 3.379 | 3.106 |
| **$Log_{10}$(CF** *[m/yr]***)** | | | |
| Mean | -3.425 | -3.438 | -3.230 |
| Median | -3.528 | -3.536 | -3.266 |
| Variance | 1.044 | 1.063 | 0.863 |
| 5th Percentile | -4.816 | -4.891 | -4.594 |
| 25th Percentile | -4.057 | -4.150 | -3.857 |
| 75th Percentile | -3.070 | -3.135 | -2.815 |
| 95th Percentile | -1.126 | -1.131 | -1.100 |
| **$Log_{10}$(F** *[yrs/m]***)** | | | |
| Mean | 6.226 | 6.284 | 6.067 |
| Median | 6.308 | 6.458 | 6.132 |
| Variance | 0.753 | 0.674 | 0.575 |
| 5th Percentile | 4.767 | 5.000 | 4.611 |
| 25th Percentile | 5.769 | 5.788 | 5.721 |
| 75th Percentile | 6.781 | 6.821 | 6.555 |
| 95th Percentile | 7.377 | 7.379 | 7.106 |
| **Fraction of Stream Tubes failing to exit the model** | 0.000 | 0.008 | 0.000 |

*Table 5-4* *Statistical summary for three realisations of 120 starting positions with a flow porosity of $\varepsilon_f = 1 \cdot 10^{-4}$ and a flow-wetted surface of, $a_r = 1.0\ m^2/(m^3\ rock)$.*

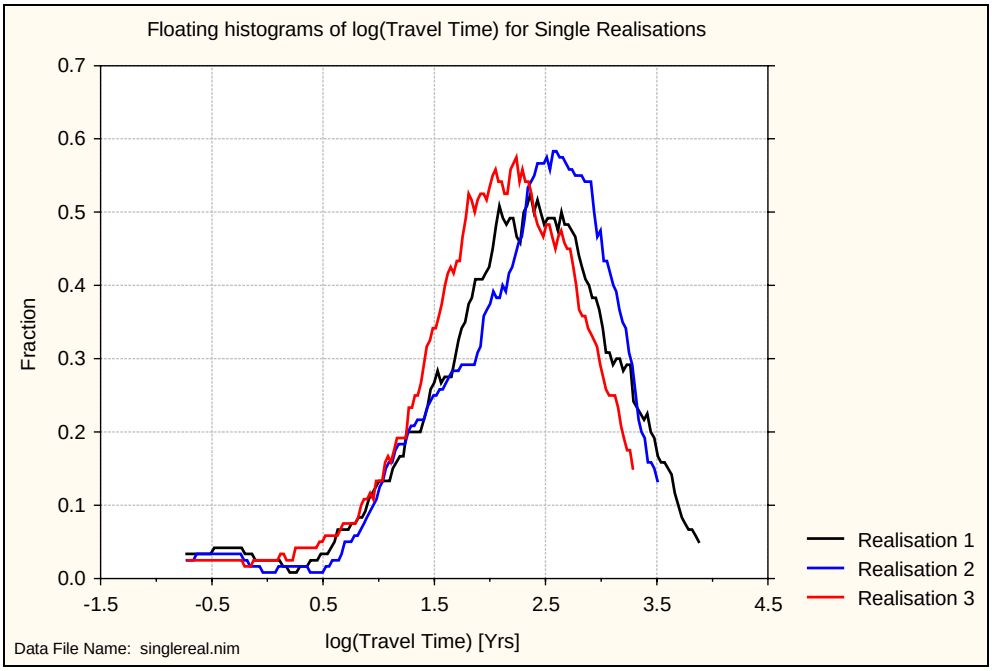


*Figure 5-17* *Floating histograms of $log_{10}$ travel time for three realisations. Results for 120 starting positions and a flow porosity of $\varepsilon_f = 1 \cdot 10^{-4}$.*

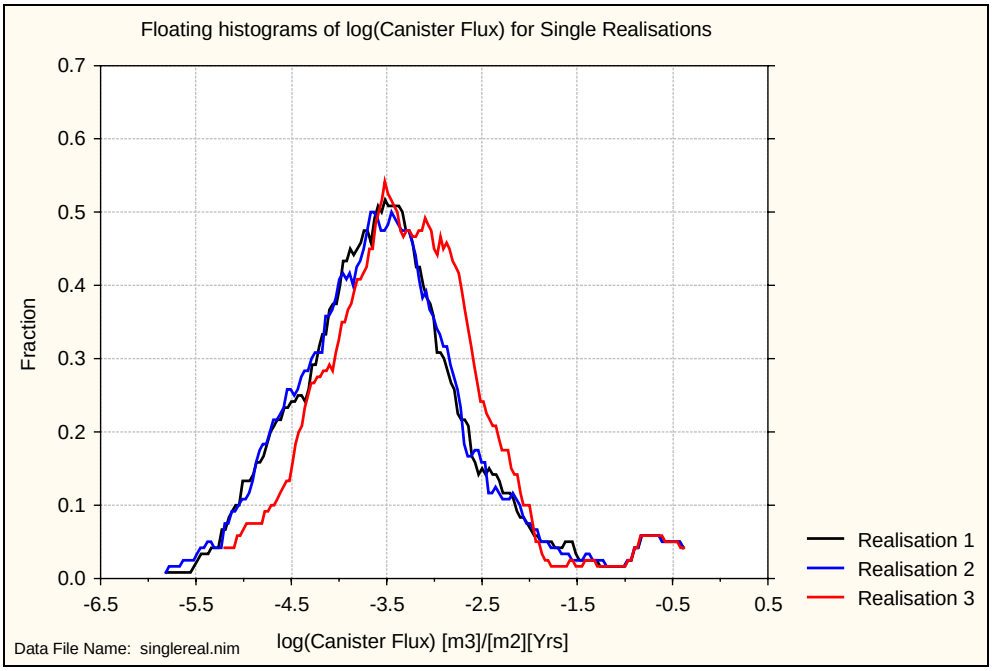


*Figure 5-18* *Floating histograms of $log_{10}$ canister flux for three realisations. Results for 120 starting positions.*

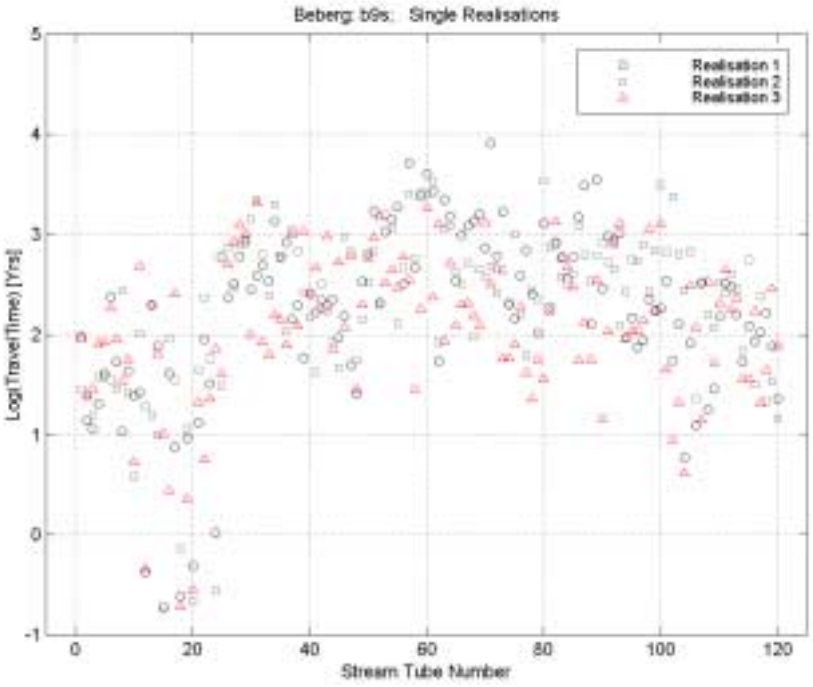


*Figure 5-19* *Scatter plot of $log_{10}$ travel time for three realisations. Results for 120 starting positions and a flow porosity of $\varepsilon_f = 1 \cdot 10^{-4}$.*

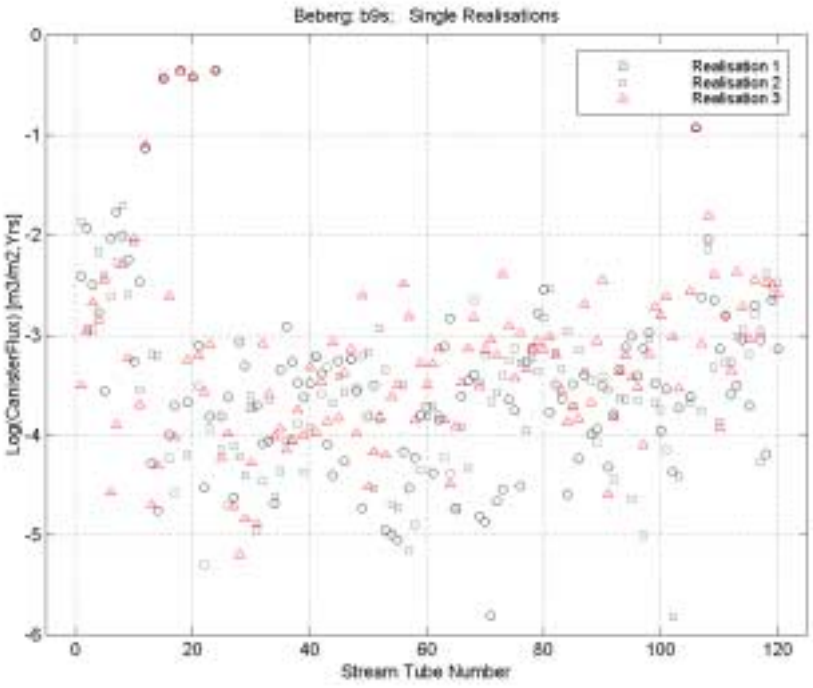


*Figure 5-20* *Scatter plot of $log_{10}$ canister flux for three realisations. Results for 120 starting positions.*

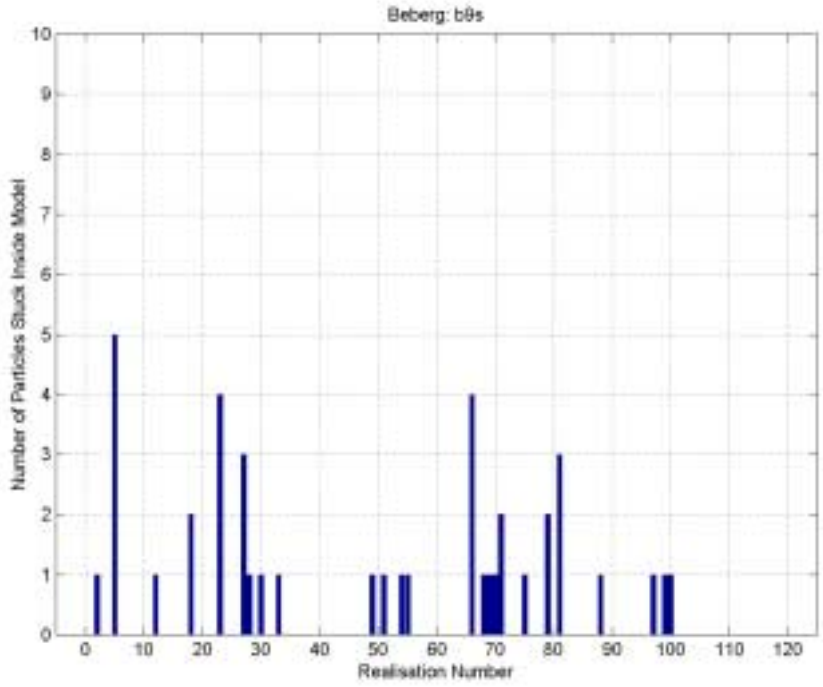


*Figure 5-21* *Number of released particles for each realisation that failed to exit the model. Results for 100 realisations of 120 starting positions.*

## 5.8 Individual Starting Positions

In order to get a measure of the variability within the realisations three different stream tube starting positions were compared. As for SR 97, starting position 8, 22 and 66 were selected presenting the results for 100 realisations. Starting position 8 represents the repository in the Southern Rock Block while positions 22 and 66 represent the southern and the northern extremes, respectively, of the hypothetical repository in the Northern Rock Block. None of these starting positions are placed within Zone 8.

Table 5-5, Figure 5-22 and Figure 5-23 present the statistical summary and the floating histograms of $\log_{10}$ travel time and $\log_{10}$ canister flux for the three starting positions with 100 realisations. The histograms are normalised with respect to the number of starting positions in each realisation. Starting position 22 has the shortest median travel time of 40 years and starting position 66 has the longest median travel time of 356 years. The canister flux at starting position 22 has the lowest value of the three starting positions. Normally we would expect an inverse correlation between the $\log_{10}$ travel time and the $\log_{10}$ canister flux and thus have the largest canister flow at starting position 22. However, this relation does not take into account the local variations in the permeability field where conductive features near the starting position might affect the results. The travel time is influenced by the variations in the permeability field along the particle pathline while the canister flux is a value calculated in a single point for each starting position.

The variances of the $\log_{10}$ travel time and the $\log_{10}$ canister flux are smaller for all of the three starting positions compared to the results based on the total ensemble of released particles. In Table 5-3 the results adjusted for the particles started within Zone 8 are presented. These results correspond much better to the results for the three individual starting positions.

Figure 5-24 and Figure 5-25 present scatter plots of the performance measures versus the realisation number for the three selected starting positions. The figures indicate that the travel time can vary over three orders of magnitude and the canister flux can vary over more than four orders of magnitude at any of these starting positions.

Figure 5-26 - Figure 5-28 present the Monte Carlo stability by plotting the cumulative median $\log_{10}$ travel time versus number of realisations for the three starting positions 8, 22 and 66. Starting positions 8 and 66 require about 50 realisations to stabilise while starting position 22 seems to stabilise slightly slower. In either case, 100 realisations appear to be adequate for reliable estimates of the median of $\log_{10}$ travel time. This also corresponds to the results from SR 97.

The exit locations for the three starting positions for 100 realisations are presented in close-up views in Figure 5-29 - Figure 5-31. The variability of the flowpaths between the different starting positions is small. The majority of the particles released from starting position 8 exit in the southern part of Zone 5. This is also the result for starting position 66. The exit locations for the particles released from starting position 22 are more variable along Zone 5.

Figure 5-32 presents the number of released particles out of the total 100 particles (one for each realisation) for each starting position that failed to exit the model. For 68 of the 120 starting positions, none of the released particles failed to exit the model for any realisation. Not more than two particles at any starting position failed to exit the model.

| | Stream Tube 8 | Stream Tube 22 | Stream Tube 66 |
|---|---|---|---|
| **$Log_{10}$(TT** *[yrs]***)** | | | |
| Mean | 1.974 | 1.684 | 2.628 |
| Median | 1.991 | 1.606 | 2.552 |
| Variance | 0.466 | 0.470 | 0.301 |
| 5th Percentile | 0.881 | 0.637 | 1.752 |
| 25th Percentile | 1.443 | 1.155 | 2.213 |
| 75th Percentile | 2.462 | 2.125 | 2.917 |
| 95th Percentile | 3.018 | 2.798 | 3.582 |
| **$Log_{10}$(CF** *[m/yr]***)** | | | |
| Mean | -2.899 | -4.278 | -3.649 |
| Median | -2.879 | -4.220 | -3.663 |
| Variance | 0.555 | 0.596 | 0.546 |
| 5th Percentile | -4.386 | -5.795 | -5.006 |
| 25th Percentile | -3.278 | -4.799 | -4.097 |
| 75th Percentile | -2.299 | -3.784 | -3.149 |
| 95th Percentile | -1.827 | -3.237 | -2.519 |
| **$Log_{10}$(F** *[yrs/m]***)** | | | |
| Mean | 5.974 | 5.684 | 6.628 |
| Median | 5.991 | 5.606 | 6.552 |
| Variance | 0.466 | 0.470 | 0.301 |
| 5th Percentile | 4.881 | 4.637 | 5.752 |
| 25th Percentile | 5.443 | 5.155 | 6.213 |
| 75th Percentile | 6.462 | 6.125 | 6.917 |
| 95th Percentile | 7.018 | 6.798 | 7.582 |
| **Fraction of Stream Tubes failing to exit the model** | 0.000 | 0.000 | 0.000 |

*Table 5-5* *Statistical summary for three starting positions. Results for 100 realisations with a flow porosity of $\varepsilon_f = 1 \cdot 10^{-4}$ and a flow-wetted surface of, $a_r = 1.0\ m^2/(m^3\ rock)$.*

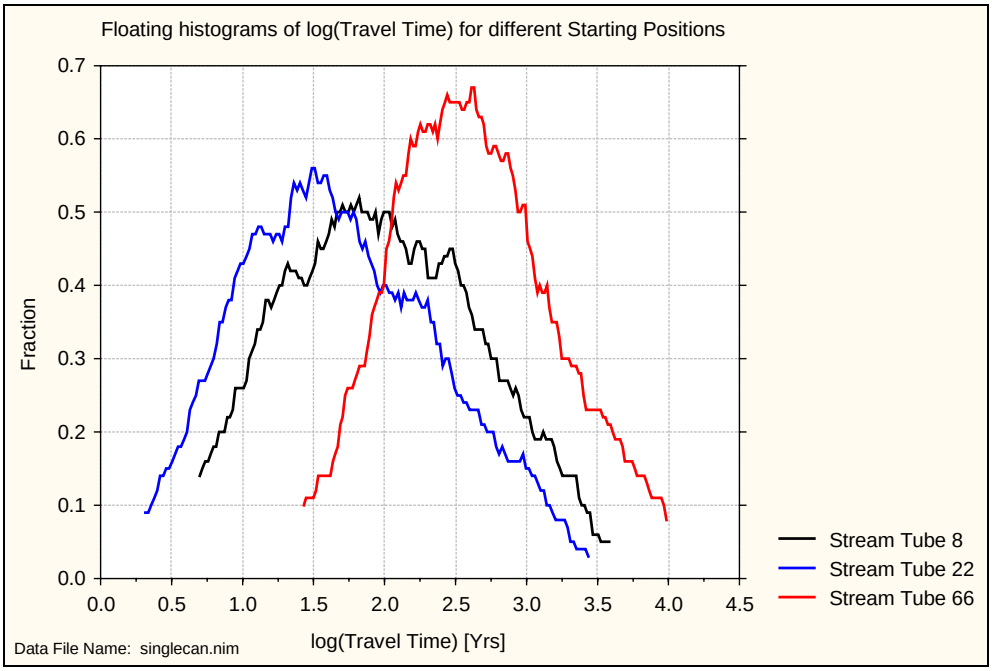


*Figure 5-22* *Floating histograms of $log_{10}$ travel time for three starting positions. Results for 100 realisations and a flow porosity of $\varepsilon_f = 1 \cdot 10^{-4}$.*

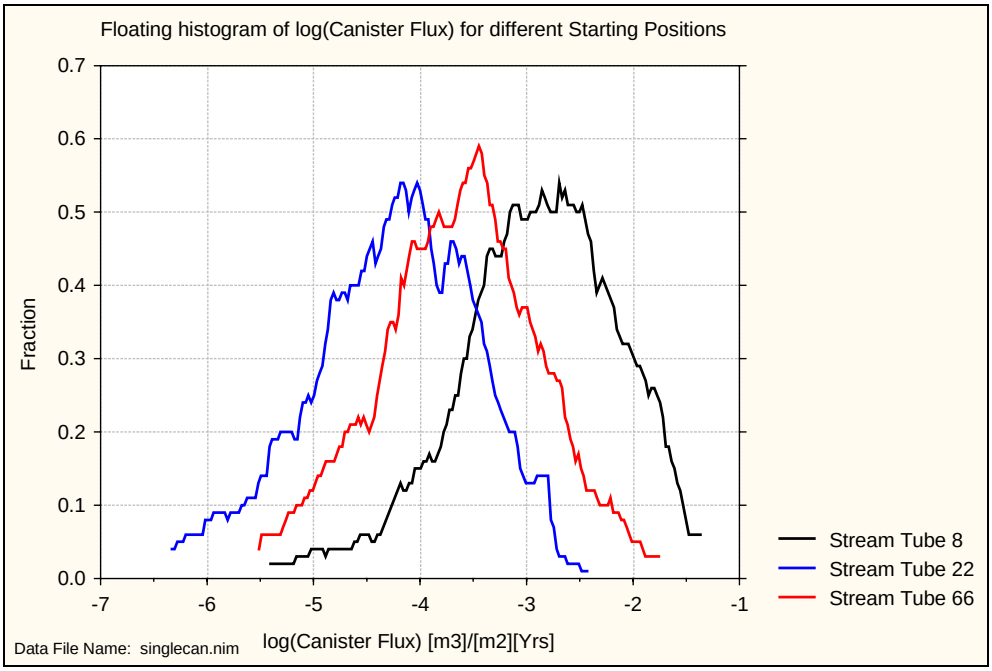


*Figure 5-23* *Floating histograms of $log_{10}$ canister flux for three starting positions. Results for 100 realisations.*

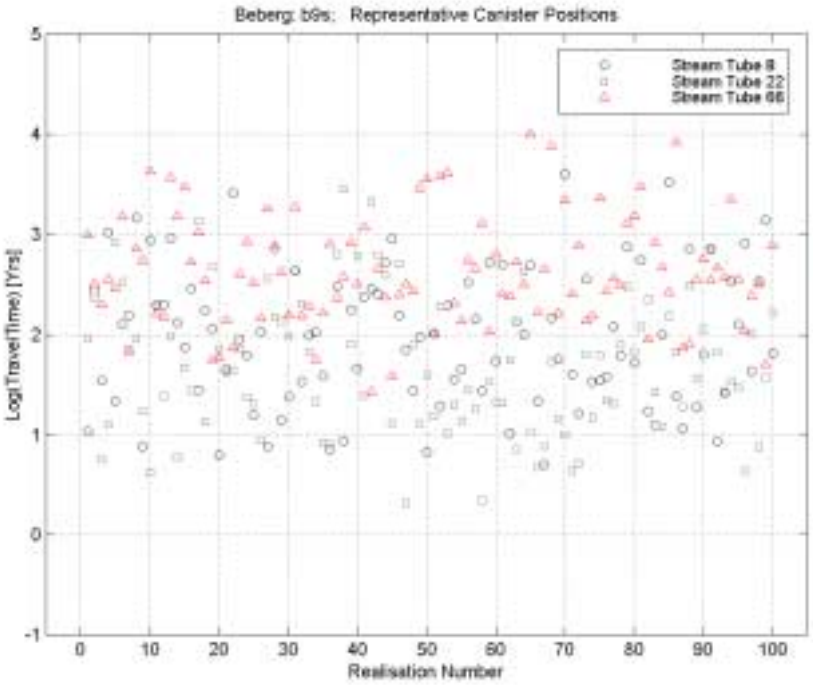


*Figure 5-24* *Scatter plot of $log_{10}$ travel time for three starting positions. Results for 100 realisations and a flow porosity of $\varepsilon_f = 1 \cdot 10^{-4}$.*

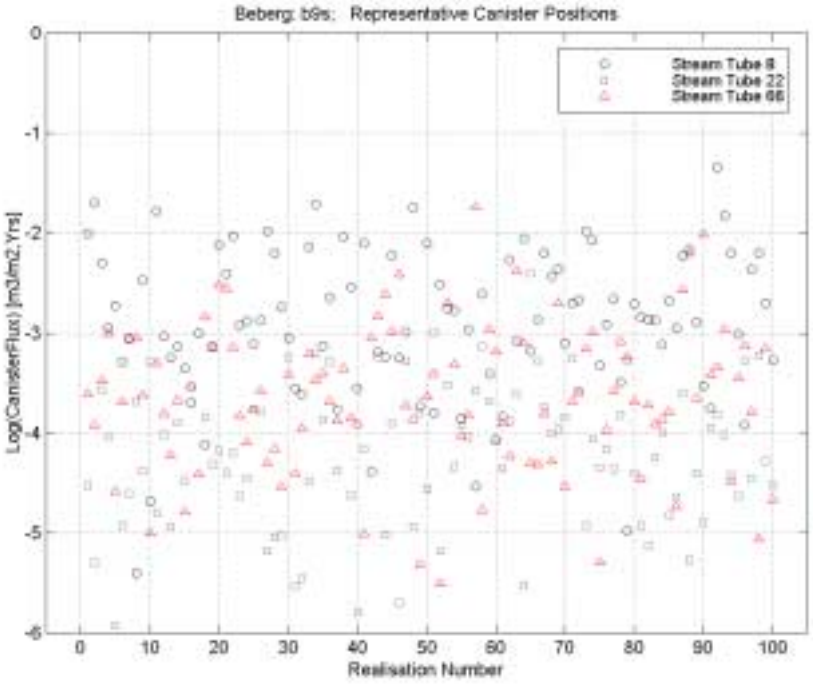


*Figure 5-25* *Scatter plot of $log_{10}$ canister flux for three starting positions. Results for 100 realisations.*

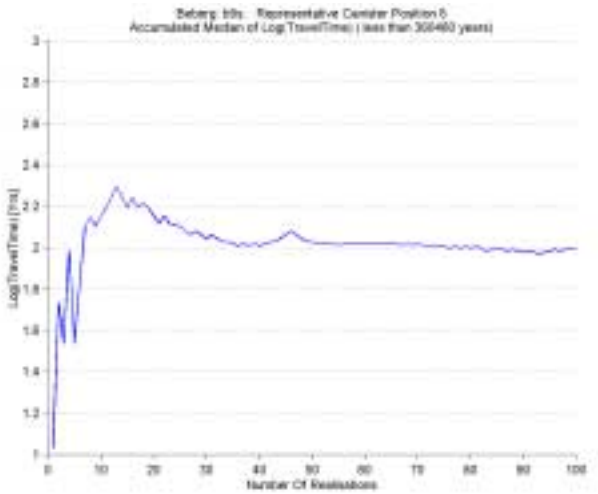

*Figure 5-26 Monte Carlo stability at starting position 8. Cumulative median $log_{10}$ travel time versus number of realisations. Results for 100 realisations and a flow porosity of $\varepsilon_f = 1 \cdot 10^{-4}$.*

*Figure 5-27 Monte Carlo stability at starting position 22. Cumulative median $log_{10}$ travel time versus number of realisations. Results for 100 realisations and a flow porosity of $\varepsilon_f = 1 \cdot 10^{-4}$.*

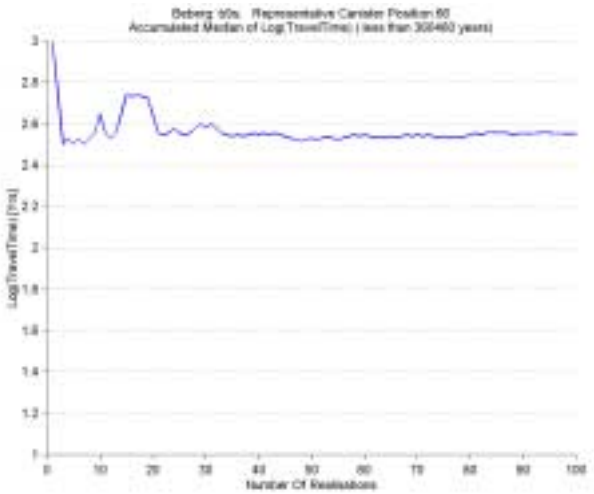

*Figure 5-28 Monte Carlo stability at starting position 66. Cumulative median $log_{10}$ travel time versus number of realisations. Results for 100 realisations and a flow porosity of $\varepsilon_f = 1 \cdot 10^{-4}$.*

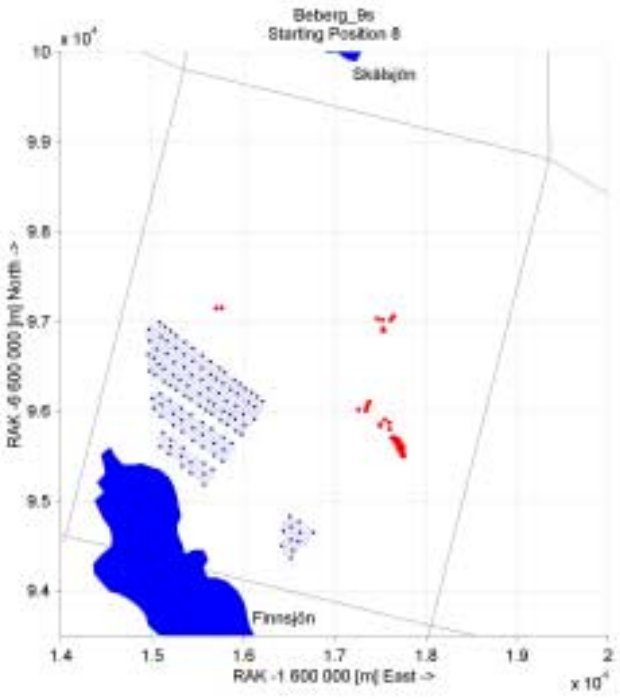


*Figure 5-29 Exit locations for starting position 8. Results for 100 realisations.*

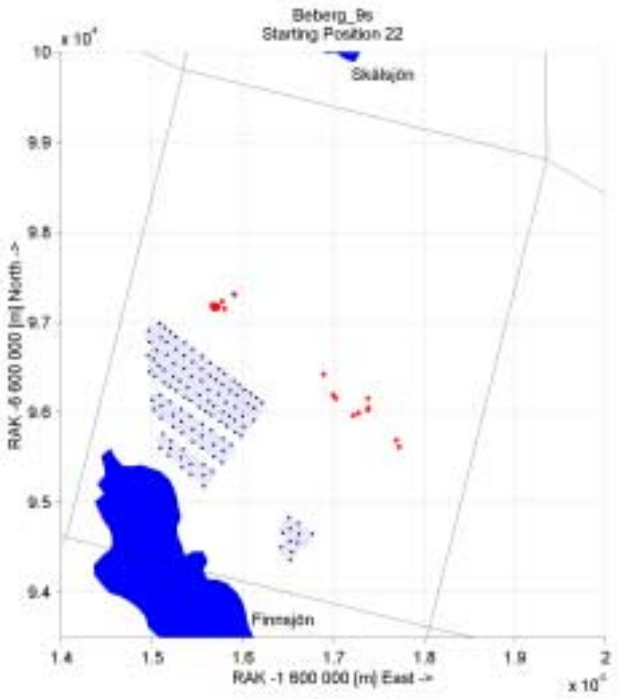


*Figure 5-30 Exit locations for starting position 22. Results for 100 realisations.*

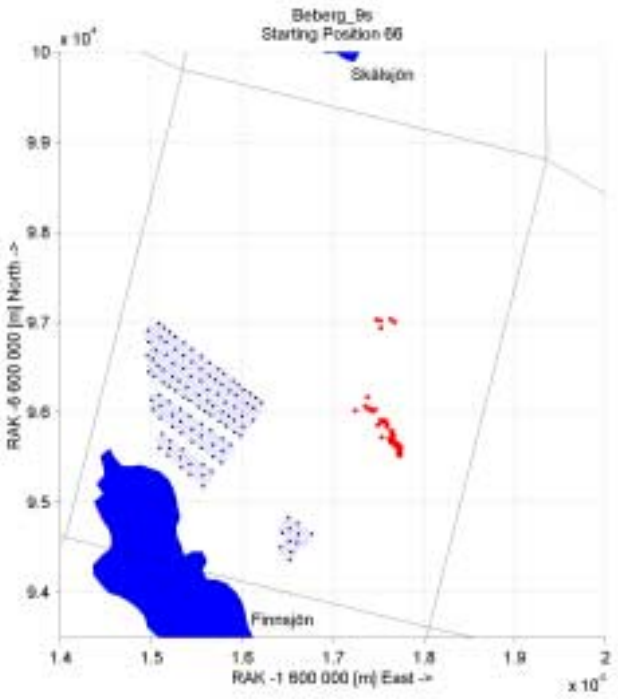


*Figure 5-31 Exit locations for starting position 66. Results for 100 realisations.*

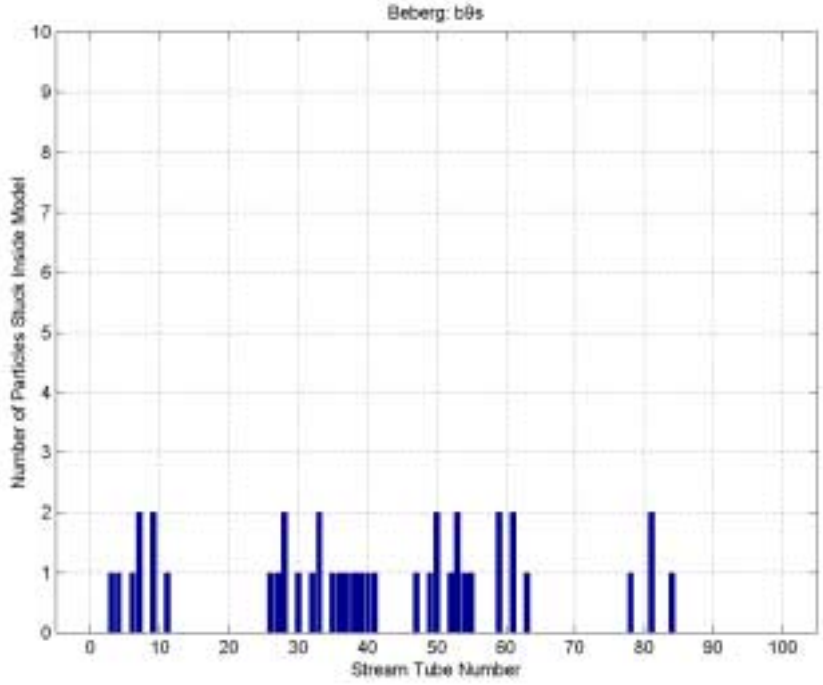


*Figure 5-32* *Number of released particles for each starting position that failed to exit the model. Results for 100 realisations of 120 starting positions.*

## 5.9 Repository Blocks

In SR 97, the hypothetical repository was divided into two blocks, with 11 starting positions in the Southern Rock Block and 109 starting positions in the Northern Rock Block. In addition, the rock blocks had higher conductivities (with the Northern Rock Block being more conductive than the Southern Rock Block) than the areas outside of these. Due to a simplification of the model in this study, these rock blocks are not represented in the model. Instead, the same statistical properties have been used for the hydraulic conductivity throughout the site-scale model with the exception of the depth zonation near the top surface. Another important feature of the SR 97 model of Beberg is Zone 2 situated above the repository in the Northern Rock Block. The statistical analysis in this section is aimed at studying possible effects of the features mentioned above.

Figure 5-33 and Figure 5-34 present the floating histograms of $\log_{10}$ travel time and $\log_{10}$ canister flux respectively, sorted by repository block. Table 5-6 presents the statistical summary for each repository block. The median travel time for the Northern Repository Block is 224 years and 70 years for the Southern Repository Block. The median canister flux for the Northern Repository Block is $3.4 \cdot 10^{-4}$ m/year and $1.2 \cdot 10^{-4}$ m/year for the Southern Repository Block. This relation between the rock blocks corresponds to the results from SR 97 even if the absolute values in this study are different from the ones in SR 97 due to the differences in the structural model

discussed earlier. Actually, the absence of the higher conductivities in the repository rock blocks in this model makes it even clearer that the performance measure differences between the repositories are due to a combination of the effects from the hydraulic gradient and the presence of Zone 2. These effects reduce the canister flux and increase the travel times for starting positions in the Northern Block.

The variance of the $\log_{10}$ travel time and the $\log_{10}$ canister flux are lower in the Southern Block compared to the Northern Block. The same effects were seen in SR 97 and the suggested explanation is the presence of Zone 8 being close to some of the starting positions in the Northern Repository. This results in some very fast particles (note the humps at short travel times and at large canister fluxes for the Northern Repository Block in Figure 5-33 and Figure 5-34), which gives a larger variance.

The values for the median and the variance of the performance measures shown within brackets in Table 5-6 have been adjusted by removing the data for the five starting positions within Zone 8. This gives a much better correspondence between the variances in the two repository blocks.

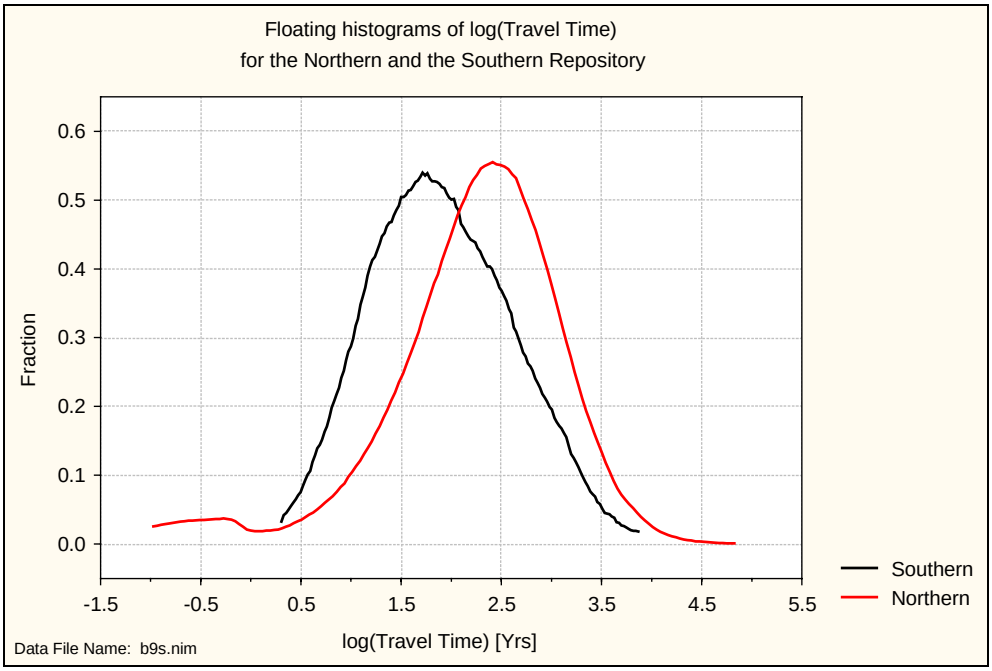


*Figure 5-33* *Floating histograms of $log_{10}$ travel time by repository block. Results for 100 realisations of 120 starting positions and a flow porosity of $\varepsilon_f = 1 \cdot 10^{-4}$.*

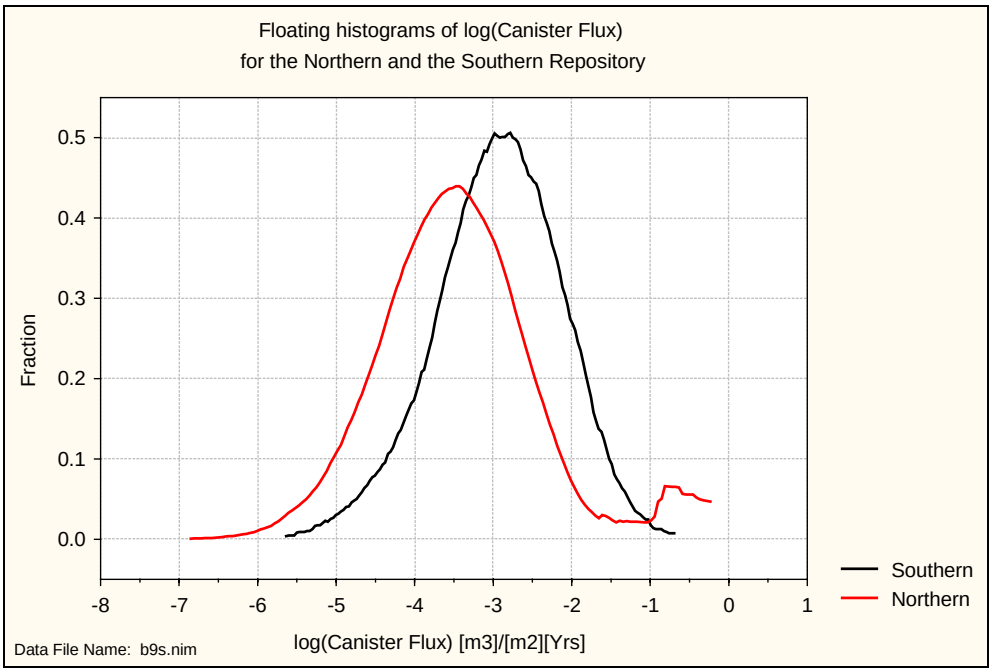


*Figure 5-34* *Floating histograms of $log_{10}$ canister flux by repository block. Results for 100 realisations of 120 starting positions.*

| | Repository Block | |
|---|---|---|
| | **Southern** | **Northern** |
| **$Log_{10}$(TT** *[yrs]***)** | | |
| Mean | 1.900 | 2.222 |
| Median | 1.843 | 2.350 (2.384) |
| Variance | 0.437 | 0.707 (0.434) |
| 5th Percentile | 0.874 | 0.695 |
| 25th Percentile | 1.412 | 1.851 |
| 75th Percentile | 2.365 | 2.751 |
| 95th Percentile | 3.015 | 3.335 |
| **$Log_{10}$(CF** *[m/yr]***)** | | |
| Mean | -2.938 | -3.385 |
| Median | -2.906 | -3.473 (-3.527) |
| Variance | 0.571 | 1.144 (0.785) |
| 5th Percentile | -4.290 | -4.915 |
| 25th Percentile | -3.392 | -4.060 |
| 75th Percentile | -2.404 | -2.891 |
| 95th Percentile | -1.772 | -0.877 |
| **$Log_{10}$(F** *[yrs/m]***)** | | |
| Mean | 5.900 | 6.222 |
| Median | 5.843 | 6.350 |
| Variance | 0.437 | 0.707 |
| 5th Percentile | 4.874 | 4.695 |
| 25th Percentile | 5.412 | 5.851 |
| 75th Percentile | 6.365 | 6.751 |
| 95th Percentile | 7.015 | 7.335 |
| **Fraction of Stream Tubes failing to exit the model** | 0.007 | 0.003 |

*Table 5-6* *Statistical summary by repository block. Results for 100 realisations of 120 starting positions with a flow porosity of $\varepsilon_f = 1 \cdot 10^{-4}$ and a flow-wetted surface of, $a_r = 1.0\ m^2/(m^3\ rock)$. Values within brackets have been adjusted by removing the data for the five starting positions within Zone 8.*

## 5.10 2D Stochastic Permeability in Fracture Zones

A variant of the model was performed to include variability in the fracture zones. Using the stochastic fracture zone facility described in Section 3.6, 10 realisations were performed with all fracture zones having a spatially varying permeability. The following prescription was used for the fracture zones:

- mean fracture permeabilities were unchanged;
- the variance in $Log_{10}$ K for the regional scale zones was taken from the RCD1 data upscaled to 100m (Walker et al., 1997);
- the variance in $Log_{10}$ K of the local-scale fracture zones was 0.29;
- a practical range of 100m.

For the local-scale zones, a variance upscaled to 35m was not available, and so a typical regional-scale value (standard deviation of about half an order of magnitude) was used for purposes of this demonstration. Hence, for the nested approach there is a requirement for the rock-mass and conductor properties to be upscaled on the two scales in a self-consistent way. Figure 5-35 shows an example of a realisation with stochastic fracture zones. The variability in the fracture zones can clearly be seen.

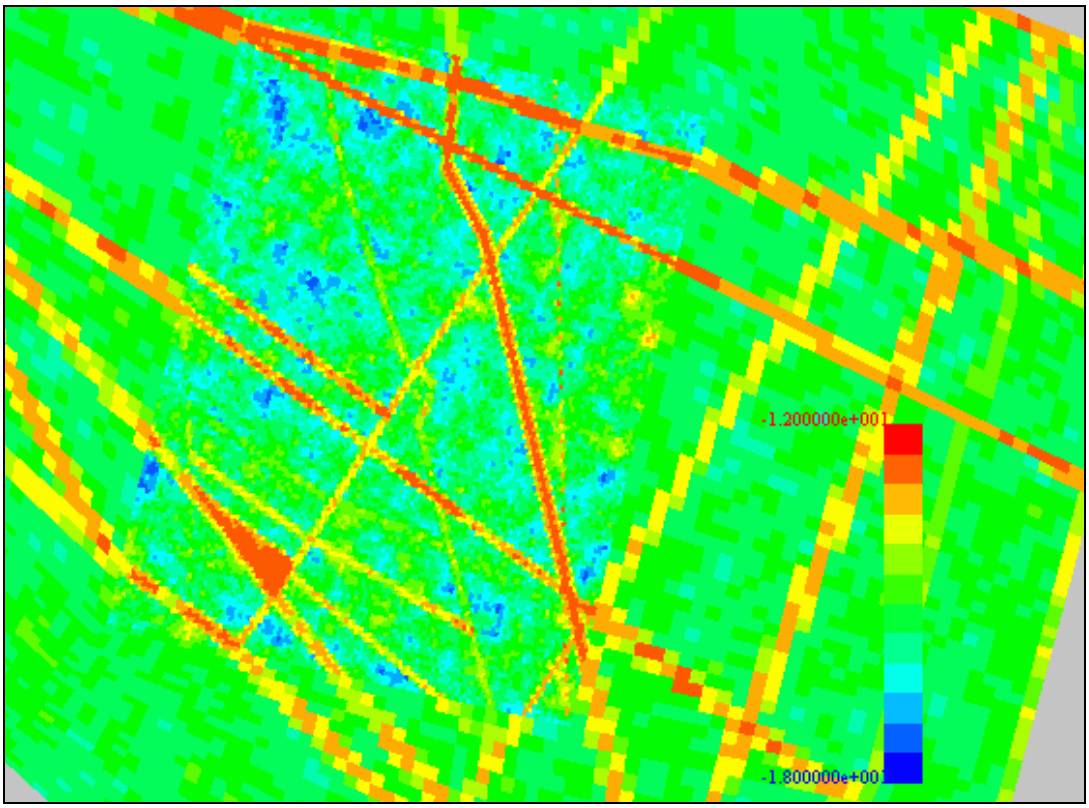


*Figure 5-35* *Permeability distribution for the variant with stochastic fractures on a slice at repository depth -604.5m masl. Values are in $m^2$.*

Some numerical difficulties were encountered with this variant due to the extra variability. To reduce the range of permeabilities a truncation was used of $10^{-18}$ $m^2$ for the minimum permeability. This is not expected to have an effect on the results since it is well below the mean value for the rock-mass and is a conservative approximation.

Table 5-7 shows the travel length statistics for the variant with stochastic fracture zones and the base case. In both variants, 120 particles were released. It is significant that the median travel length is slightly longer in the variant with the stochastic fractures albeit the number of realisations was 100 in the base case. In addition, the variance is increased compared to the base case. This is expected since the importance of particular fracture zones and channels within those zones will vary between realisations because of the introduction of heterogeneity inside the fractures.

| | NAMMU Base case | NAMMU stochastic FZs |
|---|---|---|
| **Statistics** | **$Log_{10}$(TL *[m]*)** | **$Log_{10}$(TL *[m]*)** |
| Mean | 3.515 | 3.580 |
| Median | 3.524 | 3.552 |
| Variance | 0.018 | 0.052 |
| $5^{th}$ Percentile | 3.297 | 3.275 |
| $25^{th}$ Percentile | 3.433 | 3.445 |
| $75^{th}$ Percentile | 3.589 | 3.674 |
| $95^{th}$ Percentile | 3.710 | 4.025 |

*Table 5-7* *Comparison of the travel length statistics for the variant with stochastic fracture zones and the base case.*

In Table 5-8, a comparison of the travel time and canister flux statistics for the variant with stochastic fracture zones, the base case and SR 97 is presented. The variant with stochastic fracture zones shows a small increase in the travel times compared to the base case. This corresponds to the increase in travel lengths shown above and the explanation is the same here.

| | NAMMU Base case adjusted | | NAMMU stochastic FZs | | SR 97 | |
|---|---|---|---|---|---|---|
| **Statistics** | **$Log_{10}$(TT*[yrs]*)** | **$Log_{10}$(CF*[m/yr]*)** | **$Log_{10}$(TT*[yrs]*)** | **$Log_{10}$(CF*[m/yr]*)** | **$Log_{10}$(TT*[yrs]*)** | **$Log_{10}$(CF*[m/yr]*)** |
| Median | 2.345 (221) | -3.463 | 2.425 (266) | -3.463 | 1.755 (56) | -2.923 |
| Variance | 0.450 | 0.794 | 0.497 | 0.742 | 0.237 | 0.423 |
| Standard deviation | 0.671 | 0.891 | 0.705 | 0.861 | 0.487 | 0.650 |

*Table 5-8* *Comparison of the travel time and canister flux statistics for the variant with stochastic fracture zones, the base case, and SR 97. Travel times in years given within brackets.*

Figure 5-36 presents a regional view of the model with exit locations (red markers) for the variant with stochastic fractures. The repository tunnels are shown as short black lines at -604.5 masl projected up to the top surface within the nested site-scale model that has been coloured grey. Compared to the base case, see Figure 5-10, there are some noteworthy differences. In the variant with the stochastic fractures, five of the released particles exit through the local-scale boundary into the regional model and discharge around Skälsjön. One of the particles even reaches the northern model boundary. In the base case, all of the released particles exited within the local-scale. The larger spread can also be seen in the pattern of the exit location within the local-scale model. This corresponds to the statistic results discussed above.

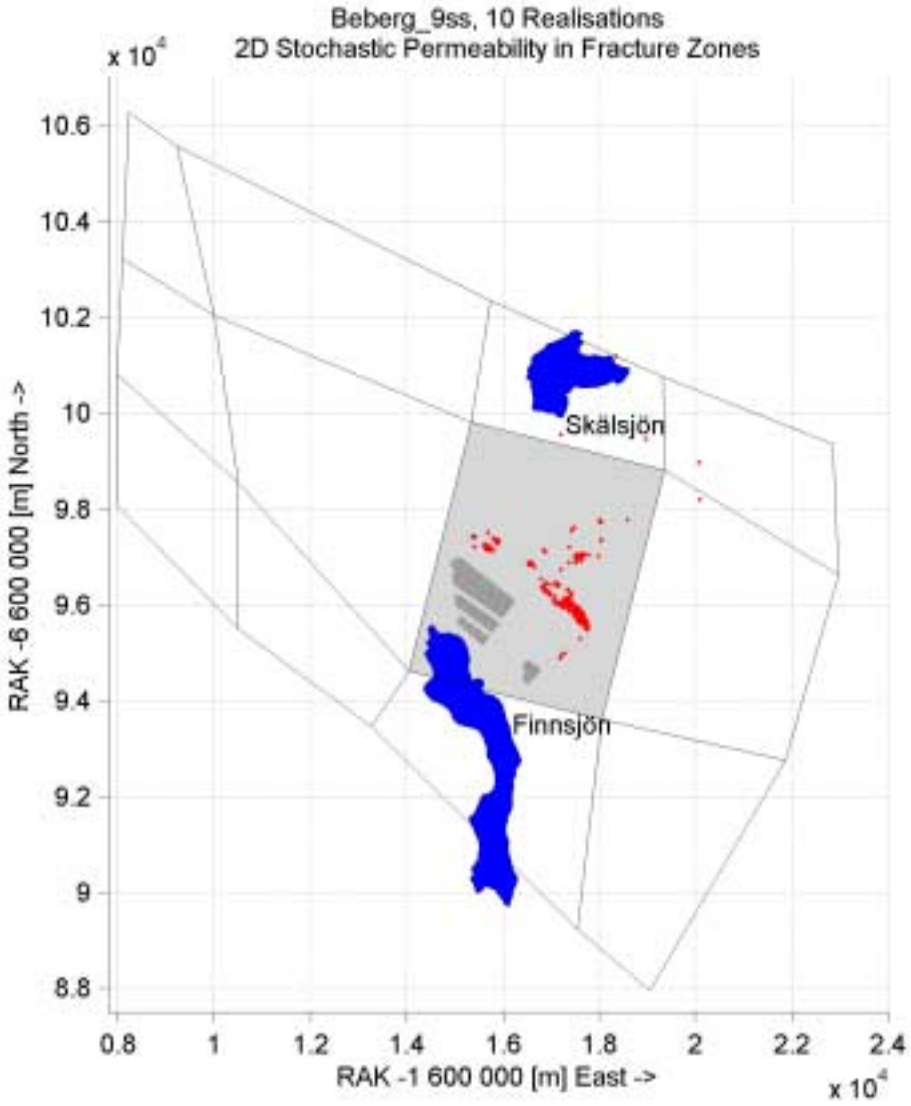


*Figure 5-36* *Regional view of the model with exit locations (red markers). Results for the variant with stochastic fracture zones and 10 realisations of 120 starting positions. Repository tunnels (black lines) at -604.5 masl in the nested site-scale model (grey) shown projected up to the model surface.*

# 6 Discussion

In this section, we discuss the benefits of the new developments, as well as summarising the stochastic modelling of Beberg and its comparison with SR 97. Finally, a brief description is given of future work to illustrate the new methodology for coupled groundwater flow and salt transport, as well as additional development tasks.

## 6.1 Developments in methodology

Here is a summary of the developments and benefits they have brought:

- **Embedded grid:** nesting of the regional- and site-scale models within the same numerical model has given greater consistency in the structural model representation and in the flow between scales. Constraints ensure that the boundary conditions set on the site-scale model are consistent in terms of both pressure distribution and boundary flux with the regional-scale for deterministic models and each stochastic realisation. Since there is a continuous representation of the regional- and site-scales, the modelling of pathways from the repository no longer has to be contained wholly by the site-scale region. Particles starting in the site-scale region can be tracked across the interface with regional-scale model continuously. Hence, the site-scale model does not necessarily have to be extended to capture all exit locations. Instead the site-scale should be chosen to represent the heterogeneities in flow around the canister positions and along any short paths, while the exit of longer pathways may be represented adequately in the regional-scale. This allows greater choice in the size of the site-scale. For example, the number of nodes required may be reduced to model more complex physics such as salt transport, or the site-scale may be reduced in extent but have greater refinement around the repository.

- **Implicit Fracture zones (IFZ):** this method of incorporating the structural model is very efficient and allows changes to either the mesh or structures to be implement quickly. It is also supports great flexibility in the properties of the structures and rock-mass. For example, the fracture zones may be of higher or lower permeability than the rock-mass, and the permeability of both the fracture zones and rock-mass can be anisotropic.

- **Stochastic fractures:** new functionality has been added to IFZ to allow arbitrary combinations of stochastic or deterministic fracture zones with the rock-mass. Whether a fracture zone is modelled deterministically or stochastically its statistical properties can be defined independently.

- **Stochastic modelling:** efficient methods for Monte-Carlo simulation of stochastic permeability fields has been implemented and tested on SKB's computers. This used large nested models of the order of 1 million nodes that ran at approximately one realisation per hour on Sukon. This is comparable with HYDRASTAR. A hundred realisations where calculated for comparison with SR 97.

- **Visualisation:** the visualisation tool Avizier for NAMMU has been enhanced such that it is efficient for checking models and presentation.

- **PROPER interface:** NAMMU outputs pathlines in PROPER format so that it can be included in PA workflow.

- **Pathline algorithm:** enhancements to the pathline algorithm were investigated to improve accuracy and prevent particle loss. Progress was made on automatic selection of step size, but more work is required in interpolating the velocity field. Particle loss did not prove a significant problem for the SR 97 calculations.

## 6.2 Model application and comparison to SR 97

The consistency of the developed methods has been verified by comparison with the model approaches used for the Beberg site in SR 97. The model properties are broadly consistent with the models used in SR 97. The main differences are the finer discretisation in the regional-scale and the lack of representation of the Repository Rock Blocks used in the present model. As expected the latter proved to have a significant impact on the results.

The boundary flow was calculated over the interface between the nested models to check the mass balance of the site-scale model. The directions of flow all agree with the HYDRASTAR model in SR 97. The main difference between the models is the flow on the vertical sides, which is about three times higher than in SR 97. The reasons for this are probably the greater refinement of regional-scale flows and an improved match of fracture zone geometries between the regional and the site-scale models. These are a consequence of the nesting technique used and it gives greater connectivity across the interface, and hence larger mass flux between the two scales. Due to the higher grid resolution, the flow match between the site- and regional-scales is much improved compared to SR 97. The mass balance is relatively small considering the calculation always is approximate for a finite-element method.

The Monte-Carlo technique that was used to perform the 100 stochastic realisations gave stable results for the medians of the performance measures after approximately 35 realisations. Thus, a total number of 100 realisations are adequate for estimating the medians of the performance measures. This is in agreement with the results from SR 97.

The performance measures were calculated for 100 realisations of the 120 starting positions. Only 0.3 % of the released particles failed to exit the model due to numerical problems. An increase of this value would be expected if the variance of the permeability increases or if the discretisation of the model becomes coarser.

The statistical results together with a comparison with SR 97 are summarised in Table 6-1. The median travel time is 203 years with a $\log_{10}$ variance of 0.691. The median of the $\log_{10}$ canister flux is -3.418 with a $\log_{10}$ variance of 1.108. The median travel time is a factor 3.6 higher and the median canister flux is a factor 3.1 lower compared to the results in SR 97. There are three main causes of the discrepancy. The main one being the structural model around the repository. These areas are called the Northern and the Southern Rock Blocks and in the SR 97 HYDRASTAR model they were given a higher

conductivity. In the NAMMU model these rock blocks are not represented and thus have the same conductivity as the surrounding rock. Compared to the HYDRASTAR model the area corresponding to the Northern Rock Block has a conductivity value that is a factor 5.5 lower. The area corresponding to the Southern Rock Block has a conductivity value that is a factor 2.4 lower. Hence, the travel time is increased and the canister flux is decreased in the NAMMU model. The second cause has the opposite effect, and that is that five of the stream tube starting positions are located in NAMMU's representation of Zone 8. The travel times associated with these positions will be exceptionally short. There is a similar effect on the canister flux at these positions. The much large permeability for Zone 8 is the main cause of the higher variances seen in the NAMMU model. The final cause is the representation of the fracture zones as deterministic in the NAMMU model. Given these reasons the differences, as presented in Table 6-1, are understandable.

Because the starting positions located inside Zone 8 have a large effect on the variance, an effort to quantify the effect of this bias was made by removing the data from these five particles when calculating the statistics. The result is presented in Table 6-1 as "adjusted" values. The median travel time and the median canister flux are not affected much by this correction. The travel time is, as expected, slightly increased while the canister flux is slightly deceased. The variance however changes significantly. The adjusted $\log_{10}$ standard deviation in canister flux is 0.891, a factor 1.37 larger compared to SR 97. However, the value is very close to the standard deviation in hydraulic conductivity ($\log_{10}$(K)) which is 0.831, and hence reasonable. It is difficult to predict an 'expected' standard deviation in canister flux as the practical range of $\log_{10}$(K) is bigger than the distance from each start point to the nearest site-scale fracture zone. Given the differences in the representation of the two rock blocks, calculated boundary flux and to a lesser degree the structural model, for example Zone 2, the pathline statistics are broadly consistent.

| | NAMMU total | | NAMMU adjusted | | SR 97 | |
|---|---|---|---|---|---|---|
| **Statistics** | **$\log_{10}$(TT*[yrs]*)** | **$\log_{10}$(CF*[m/yr]*)** | **$\log_{10}$(TT*[yrs]*)** | **$\log_{10}$(CF*[m/yr]*)** | **$\log_{10}$(TT*[yrs]*)** | **$\log_{10}$(CF*[m/yr]*)** |
| Median | 2.308 (203) | -3.418 | 2.345 (221) | -3.463 | 1.755 (56) | -2.923 |
| Variance | 0.691 | 1.108 | 0.450 | 0.794 | 0.237 | 0.423 |
| Standard deviation | 0.831 | 1.0526 | 0.671 | 0.891 | 0.487 | 0.650 |

*Table 6-1* *Comparison of the travel time and canister flux statistics for the current study and SR 97. Travel times in years given within brackets.*

The exit locations for the released particles were calculated for all realisations. The pathlines are predominantly directed to the northeast through the rock mass away from the repository. This corresponds to the regional flow pattern. The major part of the particle exit locations is grouped close together near Zone 5 and Zone 1. For the particles released from the Northern Repository, Zone 2 is a very important transport feature. Eventually Zone 5 is transporting the majority of the particles up to the top

surface of the model. Some particles exit in Zone 1 or the Imundbo Zone, which had greater importance in SR 97 with a majority of the exit locations. All released particles exited within the site-scale model.

The deterministic fractures used in the present model proved to have an effect on the released particles. Many particles follow Zone 5 in a direction perpendicular to the hydraulic gradient. When the fractures are implicitly represented in the model, the permeability of the fracture elements is made anisotropic in the length direction of the fracture. This enhances the flow in the fracture plane and makes it possible for the particles to go in a direction not exactly corresponding to the hydraulic gradient.

In conclusion, given the discrepancies between the models the results are broadly consistent with SR 97.

## 6.3 Future Work

### 6.3.1 Variable-density flow modelling

As a result of the recent developments to NAMMU, iterative solver and nesting, it is now possible to construct a much more detailed model of post-glacial rebound and marine transgressions than was possible for the original Beberg regional-scale modelling. The overall objective would be to simulate transient saline groundwater flow to represent the effects of post-glacial rebound on the regional groundwater pattern and transport at Beberg between 4,000 years BP and 10,000 years AP, say. Issues to be addressed include:

- What numerical size of model is practicable for non-linear transient calculations?
- How should the position and prescription of boundary condition be chosen for such models?
- How feasible is stochastic continuum modelling of transient salt transport?
- How do the transport results compare with SR 97?
- How sensitive are the transport results to when particles are released either using a snapshot of the flow-field or the time-varying flow-field?

### 6.3.2 DFN modelling using NAPSAC

NAPSAC has successfully been used to model groundwater flow and transport in fractured rock e.g. at the sites Stripa and Äspö HRL. Application of NAPSAC include borehole pump- and tracer-tests, regional-scale flow and transport modelling, fracture upscaling to parameterise effective porous medium (EPM) models, unsaturated near-surface hydrogeology. NAPSAC and NAMMU are two components of the advanced software package CONNECTFLOW that allows unified DFN/EPM models.

There is a risk that fluxes into DFN models may be inconsistent with the equivalent SC (stochastic continuum) model when transferring boundary conditions to DFN models (Dershowitz et al., 1999). Hence, an objective may be to consider solutions to this issue based on nested model concepts e.g. using CONNECTFLOW.

### 6.3.3 Development of an interface between the hydrogeological database SICADA/RVS and NAMMU/IFZ

SKB uses the SICADA database to store all the hydrogeological data produced in the site investigations. This data is used in the Rock Visualisation System (RVS) interpreting and developing the structural models for each different site. The structural models form a base for the development of the hydrogeological models used for groundwater simulations. Currently, much of the data in SICADA/RVS have to be exported in an unformatted way and then reorganised or maybe even recalculated in order to fit the input data format of the groundwater code. This procedure involves many time consuming steps and will always be afflicted with the risk of accidentally introducing errors in the data. A way of solving this problem is to define a NAMMU input data format for the structural model features of interest. Useful features in the structural model could be: fractures, rock zones, repository structures, boreholes, topography, lakes, superficial cover types, outcroppings, Microstation and DXF information that can be used for visualisation purposes etc.

For a fracture the data could typically consist of the fracture geometry (a polygon chain of the corner coordinates), fracture width, conductivity, variance, porosity, depth dependence etc. Consequently, additional development of the IFZ routines in NAMMU will be needed to facilitate the interpretation of the data types imported from SICADA/RVS.

The data transferred to NAMMU will be used to represent fractures zones and repository objects in the hydrogeological model. There is a second requirement that this data, along with additional data such as maps and positions of contextual objects (e.g. lakes, roads) can be visualised simultaneously with the NAMMU results. Hence, the need is to specify the formats for several different types of objects that can be imported into both flow simulations (NAMMU) and visualisations (Avizier). Avizier currently reads in a file from NAMMU that contains grid, permeability and freedoms (head, salinity) information and the IFZ file that defines the fracture zones. Further extensions to Avizier are required in order to handle data such as Microstation format and DXF from SICADA/RVS so that integrated visualisations of flow simulations, data and contextual objects (e.g. maps, lakes) can be rendered simultaneously for presentation.

# 7 References


Boghammar B. B. Grundfelt and L. Hartley, 1997, *Investigation of the large scale regional hydrogeological situation at Ceberg***,** SKB TR-97-21.

Cliffe K. A. and C.P. Jackson, 1993, *Stochastic modelling of groundwater flow at the WIPP site.* Proceedings of the Fourth International High Level Radioactive Waste Management Conference, Las Vegas, 1993.

Cliffe K. A., S.T. Morris and J.D. Porter, 1998, *Assessment Model Validity Document; NAMMU: A program for calculating groundwater flow and transport through porous media,* SKB R-99-51.

Dershowitz B., T. Eiben, S. Follin, J. Andersson, 1999, *SR 97 - Alternative models project. Discrete fracture network modelling for performance assessment of Aberg,* SKB R-99-43.

Follin S., 1999, *Hydrogeological boundary settings in SR 97,* SKB R-99-45.

Gylling B., D. Walker and L. Hartley, 1999, *Site-scale groundwater flow modelling of Beberg,* SKB TR-99-18.

Hartley L., A. Boghammar, B. Grundfelt, 1998, *Investigation of the large scale regional hydrogeological situation at Beberg***,** SKB TR-98-24.

Hartley, L. J., 1998, *NAPSAC (Release 4.1) Technical Summary Document*, AEA Technology Report AEA-D&R-0271.

Hartley, L. J., K.A. Cliffe, A.W. Herbert, M.G. Shepley and P.M. Wilcock 2001 *Groundwater Flow Modelling with a Combined Discrete Fracture Network and Continuum Approach Using the Code CONNECTFLOWt*, AEA Technology Report AEA/ENV/R/0520.

Lee, S.H., C.L. Jensen and M.F. Lough, 2000, *Efficient Finite-Difference Model for Flow in a Reservoir with Multiple Length-Scale Fractures*, PE Journal, Vol. 5, No. 3, September 2000.

Marsic N., 1998, *Using Statistica and Matlab when evaluating results from HYDRASTAR 1.5+*, SKB TS-99-04.

Marsic N., and L. Hartley, 2000, *Modelling of the Site Scale Hydrogeological situation at Beberg Using NAMMU,* SKB R-00-14.

Morris S. T. and K.A. Cliffe, 1994, *Verification of HYDRASTAR: Analysis of hydraulic conductivity fields and dispersion*, SKB TR 94-21.

Rhén, I., G. Bäckblom, G. Gustafson, R. Stanfors and P. Wikberg, 1997, Results from Pre-investigations and Detailed Site Characterization, Summary Report, SKB TR-97-03.

Svensson, U., 1999, Representation of Fracture Networks as Grid Cell Conductivities, SKB TR-99-05.

Walker D., I. Rhen. and I. Gurban, 1997, *Summary of hydrogeologic conditions at Aberg, Beberg and Ceberg,* SKB TR 97-23.

Walker D., B. Gylling, 1998, *Site-scale groundwater modelling of Aberg,* SKB TR-98-23.

Walker D., B. Gylling, 1999, *Site-scale groundwater modelling of Ceberg,* SKB TR-99-13.

# A 1 Quality Assurance

This section contains information about program versions, file names and storage locations. Some of the files have been written to a CD-ROM together with the final report.

## A 1.1 Tools Used

In this project, NAMMU 7.0 *[http://www.aeat-env.com/groundwater/nammu.htm]* was used for the groundwater calculations (Cliffe et al., 1998). The latest NAMMU feature used was 7.0.15 which is now included in the latest NAMMU version. The code and license are installed at SKB's machine *"Sukon"* at the following directory:

`sukon:/export/skb/nammu/nammu6.3/`

For visualisation purposes, AVIZIER 1.0 *[http://www.bssi.no/]* was used. The latest developments are included in this version. The code and license owned by SKB are for practical reasons installed locally at Kemakta Konsult AB.

The commercial statistical data analysis software Statistica *[http://www.statsoft.com/]* has been used for the statistical analysis of the travel times and canister fluxes of the released particles. The script developed for the analysis is described in (Marsic, 1998).

## A 1.2 File Location

All input and output model files are stored on SKB's machine *"Sukon"* at the following directory (*`path`*):

`sukon:/export/skb/project/nammu/2224/`

The model files used for the Monte Carlo simulations in the present report are:

*`path`*`/dat/beberg_model9s.dat`

*`path`*`/dat/beberg_solve9s.dat`

*`path`*`/dat/beberg_output9s.dat`

where *`path`* is defined above.

## A 1.3 List of Figures

The file names of the figures used in the report are listed in Table A 1-1.

| File Name | File Size | Date | Figure |
|---|---|---|---|
| b9s_grid1.tif | 2 122 658 | 2001-01-22 | Figure 3-2 a) |
| b9s_c_1.tif | 2 122 658 | 2001-01-22 | Figure 3-2 b) |
| zed_h.eps | 2 348 477 | 2000-08-23 | Figure 3-5 a) |
| zed_k.eps | 182 084 | 2000-08-23 | Figure 3-5 b) |
| zed_p.eps | 32 025 | 2000-08-23 | Figure 3-5 c) |
| wgate_h.eps | 2 207 892 | 2000-08-23 | Figure 3-6 a) |
| wgate_k.eps | 180 235 | 2000-11-10 | Figure 3-6 b) |
| wgate_p.eps | 33 697 | 2000-08-23 | Figure 3-6 c) |
| fracture_volumes.tif | 736 496 | 2001-01-25 | Figure 3-7 a) |
| rough_fracture_paths.tif | 736 496 | 2001-01-25 | Figure 3-7 b) |
| b9s_f_r.tif | 2 218 886 | 2001-01-22 | Figure 4-1 |
| b9s_f_l.tif | 2 218 886 | 2001-01-22 | Figure 4-2 |
| b9s_c_2.tif | 1 892 940 | 2001-01-22 | Figure 4-3 |
| b9s_c_l.tif | 1 984 558 | 2001-01-22 | Figure 4-4 |
| b9s_p_2.tif | 1 892 940 | 2001-01-22 | Figure 4-5 |
| b9s_startpos_c.tif | 1 902 710 | 2001-02-12 | Figure 4-6 |
| b9s_p.tif | 2 163 690 | 2001-01-23 | Figure 5-1 |
| medttlg2.stg | 3 374 | 2001-01-09 | Figure 5-2 |
| medcflg2.stg | 3 374 | 2001-01-09 | Figure 5-3 |
| histtlg1.stg | 2 814 | 2001-01-09 | Figure 5-4 |
| boxttlg1.stg | 6 784 | 2001-01-08 | Figure 5-5 |
| histtlg2.stg | 2 814 | 2001-01-09 | Figure 5-6 |
| sca_lglg.stg | 98 574 | 2001-01-09 | Figure 5-7 |
| hiscflg1.stg | 2 814 | 2001-01-09 | Figure 5-8 |
| boxcflg2.stg | 9 284 | 2001-01-08 | Figure 5-9 |
| b9s_reg_all.tif | 392 408 | 2001-01-19 | Figure 5-10 |
| b9s_loc_all.tif | 650 386 | 2001-01-19 | Figure 5-11 |
| b9s_paths_0.tif | 2 058 234 | 2001-01-22 | Figure 5-12 a) |
| b9s_paths_300.tif | 2 051 714 | 2001-01-22 | Figure 5-12 b) |
| b9s_paths_750.tif | 2 051 714 | 2001-01-22 | Figure 5-12 c) |
| b9s_obj_r1_3_c.tif | 1 898 306 | 2001-01-31 | Figure 5-13 a) |
| b9s_obj_r1_3_p.tif | 1 898 306 | 2001-01-31 | Figure 5-13 b) |
| b9s_obj_r1_3_pf.tif | 1 898 306 | 2001-01-31 | Figure 5-13 c) |
| b9s_loc_r1.tif | 580 122 | 2001-01-19 | Figure 5-14 |
| b9s_loc_r2.tif | 582 700 | 2001-01-19 | Figure 5-15 |
| b9s_loc_r3.tif | 580 846 | 2001-01-19 | Figure 5-16 |
| histtlg7.stg | 8 389 | 2001-01-09 | Figure 5-17 |
| hiscflg6.stg | 8 389 | 2001-01-09 | Figure 5-18 |
| b9s_single_real_sca_tt.tif | 98 886 | 2001-01-19 | Figure 5-19 |
| b9s_single_real_sca_cf.tif | 98 948 | 2001-01-19 | Figure 5-20 |
| b9s_stuck_per_real.tif | 143 560 | 2001-01-19 | Figure 5-21 |
| histtlg7.stg | 8 388 | 2001-01-09 | Figure 5-22 |
| hiscflg6.stg | 8 388 | 2001-01-09 | Figure 5-23 |
| b9s_single_can_sca_tt.tif | 97 268 | 2001-01-19 | Figure 5-24 |
| b9s_single_can_sca_cf.tif | 97 908 | 2001-01-19 | Figure 5-25 |
| b9s_single_can1_ackmed_tt.tif | 91 534 | 2001-01-19 | Figure 5-26 |
| b9s_single_can2_ackmed_tt.tif | 92 014 | 2001-01-19 | Figure 5-27 |
| b9s_single_can3_ackmed_tt.tif | 87 810 | 2001-01-19 | Figure 5-28 |
| b9s_loc_c1.tif | 581 592 | 2001-01-19 | Figure 5-29 |
| b9s_loc_c2.tif | 578 138 | 2001-01-19 | Figure 5-30 |
| b9s_loc_c3.tif | 582 530 | 2001-01-19 | Figure 5-31 |
| 9s_stuck_per_can.tif | 150 708 | 2001-01-19 | Figure 5-32 |
| isttlg6.stg | 6 846 | 2001-01-09 | Figure 5-33 |
| iscflg5.stg | 6 846 | 2001-01-09 | Figure 5-34 |
| | | | Figure 5-35 |
| | | | Figure 5-36 |

*Table A 1-1 Summary of image files generated.*